

QATAR UNIVERSITY

COLLEGE OF ENGINEERING

DEVELOPMENT AND CHARACTERIZATION OF NICKEL PHOSPHORUS BASED

NANOCOMPOSITE COATINGS FOR CORROSION PROTECTION OF STEEL

BY

OSAMA FAYYAZ

A Thesis Submitted to
the College of Engineering
in Partial Fulfillment of the Requirements for the Degree of
Master of Science in Mechanical Engineering

June 2021

© 2021. Osama Fayyaz. All Rights Reserved.

COMMITTEE PAGE

The members of the Committee approve the Thesis of
Osama Fayyaz defended on 05/03/2021.

Dr. Anwarul Hasan
Thesis Supervisor

Dr. Abdul Shakoor
Thesis Co-Supervisor

Dr Bilal Mansoor
Committee Member

Dr Talal Mohammed Ahmad Altahtamouni
Committee Member

Approved:

Khalid Kamal Naji, Dean, College of Engineering

ABSTRACT

FAYYAZ, OSAMA, Masters :

June : 2021:], Masters of Science in Mechanical Engineering

Title: Development and Characterization of Nickel Phosphorus based Nanocomposite Coatings for Corrosion Protection of Steel

Supervisor of Thesis: Dr. MD Anwarul Hassan

Co-Supervisor of Thesis: Dr. Abdul Shakoor

Corrosion is the major challenge faced by many industries like marine, automobile, oil and gas industry, etc. Nickel Phosphorus (Ni-P) based coatings are extensively studied to mitigate corrosion due to their improved corrosion resistance. However, these coatings lack mechanical strength limiting their applications. In the present study, novel Ni-P-X (X=TiC (titanium carbide) and ZrC (zirconium carbide)) were developed through the electrodeposition process. Various amounts of titanium carbide TiC nanoparticles (0, 0.5, 1.0, 1.5, and 2.0 g/L) and ZrC nanoparticles (0, 0.75 and 1.5 g/L) were co-electrodeposited in the Ni-P matrix under optimized conditions and then characterized by employing various techniques. It is noticed that the concentration of reinforcing ceramic particles has a significant on the structural, mechanical, tribological, and electrochemical properties of Ni-P nanocomposite coatings. The structural analysis of both types of prepared nanocomposite coatings indicates uniform, compact, and nodular structured coatings without any noticeable defects. Vickers microhardness and nanoindentation results of Ni-P-TiC nanocomposite coatings demonstrate the increase in the hardness with an increasing amount of TiC nanoparticles attaining its terminal value (5.98 GPa) at the concentration

of 1.5 g/L, which can be ascribed to dispersion hardening effect. Further increase in the concentration of TiC nanoparticles results in a decrease in hardness, which can be ascribed to their accumulation in the Ni-P matrix. The electrochemical results of Ni-P-TiC nanocomposite coatings indicate the improvement in corrosion protection efficiency of coatings with an increasing amount of TiC particles reaching ~92% at 2.0 g/L, which can be ascribed to a reduction in the active area of the Ni-P matrix by the presence of inactive ceramic particles. Similarly, in the case of Ni-P-ZrC nanocomposite coatings, the best mechanical (5.75 GPa) and corrosion protection efficiency (~85 %) are achieved at the composition of 0.75 g/L. The favorable structural, mechanical, and corrosion protection characteristics of Ni-P-TiC and Ni-P-ZrC nanocomposite coatings suggest their potential applications in many industries such as automotive, electronics, aerospace, oil, and gas, and seawater desalination, etc.

DEDICATION

This thesis is dedicated to my beloved father Maulana Fayyaz Ahmad Falahi Madani, and my mother, Mrs. Sara Inam, for their endless efforts, support, prayers and for being on my side all the time. They appreciated, supported and motivated me throughout the studies. I believe, without them, it would not be possible to achieve this goal.

ACKNOWLEDGMENTS

I am fortunate to be under the kind supervision of Dr. Anwarul Hasan. His exemplary guidance and constant encouragement have been a great influence in my research work and course studies. I am indebted to the Department of Mechanical and Industrial Engineering, College of Engineering, Qatar University (QU) for providing me an opportunity to excel in the important area of synthesis and characterization of advanced materials. A debt of gratitude to my co-supervisor Dr. Abdul Shakoor for supervising my entire research at the Center for Advanced Materials (CAM), QU, and providing full financial support through his awarded grant (IRCC-2020-006). His excellent guidance, regular monitoring, and encouragement throughout the research made this journey possible. A special thanks to Mr. Adnan Khan for his support throughout my research work, specifically in the understanding of electrochemical impedance spectroscopy.

Also, I would like to thank Mr. Moinuddin Yousuf and Mr. Muddasir Nawaz for helping me with characterizations whenever I needed assistance. I truly appreciate their support and guidance throughout my research.

I am indebted by gratitude to the world-class facilities and support of CAM at QU, for providing me with a chance to carry out my whole research work and various characterizations. I am also thankful to the Gas Processing Center (GPC) and Central Lab Unit (CLU) for giving me access to their world-class laboratories to conduct my research.

I would like to acknowledge the financial support of the office of the VP for Research and Graduate Studies (VPRGS), QU, through International Research Collaboration Co-Fund - IRCC-2020-006 and student grant- QUST-2-CAM-2019-7. Finally, I would

extend my gratitude to all the members of the Advanced Multifunctional Materials (AMFMs) Research Group at CAM, QU, for their great company and technical support.

TABLE OF CONTENTS

DEDICATION	v
ACKNOWLEDGMENTS	vi
LIST OF TABLES	xi
LIST OF FIGURES	xii
ABBREVIATION	xvi
Chapter 1: Introduction	1
1.1 Background	1
1.2 Overview of the State of the Art	2
1.3 Missing Point in the Literature.....	8
1.4 Goals and Objectives.....	9
Chapter 2: Materials and Methods	10
2.1 Materials.....	10
2.2 Sample Preparation and coatings synthesis.....	10
2.3 Characterization of composite coatings	12
2.3.1 Compositional Characterization	12
2.3.2 Morphological Analysis	13
2.3.3 Mechanical Properties	13
2.3.4 Corrosion Assessment	14

Chapter 3: Results and Discussion.....	16
3.1 Properties of Ni-P-TiC nanocomposite coatings.....	16
3.1.1 Structural and compositional characterization	16
3.1.2 Morphological Analysis	18
3.1.3 Mechanical Properties	28
3.1.4 Corrosion Assessment	31
3.2 Properties of Ni-P-ZrC nanocomposite coatings	38
3.2.1 Structural and compositional characterization	38
3.2.2 Morphological Analysis	42
3.2.3 Mechanical Properties	47
3.2.4 Corrosion Assessment	54
Chapter 4: Conclusion and Future Recommendation	60
4.1 Conclusions	60
4.2 Future Recommendation	61
APPENDIX A – OUTCOMES OF RESEARCH WORK.....	73
Publications	73
Conferences and Posters.....	73
APPENDIX B : POSTER PRESENTATION	74
APPENDIX C- CONFERENCE 1.....	75
APPENDIX D -JOURNAL PUBLICATION 1	76

APPENDIX E – PUBLICATION SUBMITTED91

LIST OF TABLES

Table 1. Brief overview of nickel based nanocomposite coatings. DC: Direct Current, PC: Pulse Current, PRC:Pulse Reverse Current Electrodeposition techniques.	3
Table 2. Abrief overview of the nickel phosphorus based nanocomposite coatings. ELS: Electroless, DC: Direct Current, PC: Pulse Current, PRC: Pulse Reverse Current Deposition.	6
Table 3. Average thickness of Ni-P and Ni-P-TiC composite coatings measured with thickness gauge meter.	20
Table 4. EDS quantitative analysis of Ni-P and Ni-P-TiC composite coatings.....	23
Table 5. Electrochemical parameters derived from the potentiodynamic polarization curve of carbon steel, Ni-P, and Ni-P-TiC composite coating containing various concentration of TiC particles.....	38
Table 6. EDS quantitative analysis of Ni-P and Ni-P-ZrC nanocomposite coatings...	45
Table 7. Derived parameters from load indentation profiles of Ni-P and Ni-P-ZrC nanocomposite coatings.	48
Table 8. Electrochemical parameters derived from the Tafel plots of carbon steel, Ni-P, and Ni-P-0.75g/L ZrC nanocomposite coating.....	59

LIST OF FIGURES

Figure 1. Schematic diagram of the electrodeposition process to develop Ni-P-TiC composite coatings.....	11
Figure 2. XRD spectra of Ni-P and Ni-P-TiC composite coatings containing various concentrations of TiC particles.	17
Figure 3. XPS spectra presenting the elemental composition of Ni-P/1.5g/L TiC composite coatings, (a) Ni2p, (b) P2p and (c) Ti2p.....	18
Figure 4. FE-SEM micrographs of the Ni-P (a) and Ni-P-TiC composite coating with various concentrations of TiC (b, c, d, e). A cross-sectional micrograph (f) of Ni-P-TiC composite coatings with 1.5 g/L of TiC.....	19
Figure 5. Schematic diagram for the co-deposition of TiC particles at the cathode (substrate) to form Ni-P-TiC composite coatings.....	21
Figure 6. EDS analysis along with elemental mapping of Ni-P (a) and various compositions of Ni-P-TiC composite coatings; (b) 0.5g/L (c) 1.0g/L (d) 1.5g/L (e)2.0g/L and (f) cross-section of 1.5g/L of Ni-P-TiC composite coatings.....	23
Figure 7. TEM micrographs of Ni-P-2.0g/L TiC at various magnification of (a)high magnification (b)magnified portion marked (B) in (a) and (c) showing an interface of the Ni-P matrix and TiC reinforcement.	25
Figure 8. TEM micrograph of Ni-P-2.0g/L TiC presenting the agglomeration of the particles in the Ni-P matrix.	26
Figure 9. 3D-AFM micrograph along with their corresponding surface roughness profiles of the (a) Ni-P, Ni-P-TiC composite coatings (b) 0.5g/L, (c)1.0g/L, (d) 1.5g/L, and (e) 2.0g/L of TiC particles.....	28
Figure 10. Vickers microhardness of Ni-P and Ni-P-TiC composite coatings containing	

various concentrations of TiC particles.	29
Figure 11. Nanoindentation results of Ni-P and Ni-P-TiC composite coatings containing various concentrations of TiC particles; (a) loading/unloading profiles and (b) hardness.	31
Figure 12. (a) Bode plots of the substrate, Ni-P, and Ni-P-TiC composite coatings containing the magnitude plot and (b) phase angle plot after 2 hours of immersion in 3.5wt% NaCl solution.	33
Figure 13. Equivalent electric circuit used for fitting the experimental EIS data for (a) polished carbon steel used as substrate, (b) Ni-P and Ni-P-TiC composite coatings containing different concentrations of TiC particles.	34
Figure 14: (a) Nyquist plots for carbon steel (substrate) and Ni-P-TiC composite coatings along with fitted resistance values vs. the concentration of TiC particles after the 2 hours of immersion in 3.5wt% NaCl solution (b) evolution of R_{po} and R_{ct} with the TiC.	35
Figure 15. Potentiodynamic profiles of carbon steel, Ni-P and Ni-P-TiC composite coating with increasing concentration of TiC.	37
Figure 16. XRD spectra of ZrC nanoparticles, Ni-P and Ni-P-ZrC nanocomposite coatings and containing 0.75 g/L ZCNPs.	39
Figure 17. XPS survey spectrum for NiP-0.75ZrC nanocomposite coatings.	40
Figure 18. XPS spectra presenting the elemental composition of Ni-P-ZrC nanocomposite coatings, (a) Ni2p, (b) P2p and (c) Zr (d) metal carbide	41
Figure 19. FE-SEM micrographs of developed coatings; Ni-P (a & c), Ni-P-ZrC nanocomposite coatings (b & d), at two different magnifications. A cross-sectional micrograph (e) of Ni-P- ZrC nanocomposite coatings.	43

Figure 20. EDS elemental mapping of Ni-P (a), (b) Ni-P-ZrC nanocomposite coatings, and (c) detailed elemental mapping.	44
Figure 21. Schematic diagram for the co-deposition of ZrC nanoparticles at the cathode (substrate) to form Ni-P-ZrC composite coatings.....	46
Figure 22. Three-dimensional AFM micrograph of as-prepared coatings along with their surface roughness profile; (a) Ni-P and (b), Ni-P-ZrC nanocomposite coatings.	47
Figure 23. Mechanical properties of Ni-P and Ni-P-ZrC nanocomposite coatings; (a) Vickers microhardness and (b) Load indentation depth graph of Ni-P and Ni-P-0.75ZrC nanocomposite coatings.	48
Figure 24. Wear test of the as-electrodeposited nanocomposite coatings before and after the addition of ZrC nanoparticles.	50
Figure 25. SEM of (a) Ni-P and (b) Ni-P-0.75 g/L ZrC after wear test and their corresponding wear depth profile (c, d), respectively.....	51
Figure 26. High magnification SEM of the worn scar of (a) Ni-P and (b) Ni-P/0.75ZrC nanocomposite coating.....	52
Figure 27. a) Maximum erodent depth and volume loss for the Ni-P and Ni-P-0.75ZrC nanocomposite coatings at different particles velocity after 30 s of erosion time.....	53
Figure 28. Surface topography of a) Ni-P and b) Ni-P-0.75ZrC after 30 s of erosion time at 101 m/s of particle velocity.....	54
Figure 29. (a) Bode plot of the substrate, Ni-P, and Ni-P-0.75g/L-ZrC nanocomposite coatings containing frequency impedance magnitude curve and (b) frequency phase angle curve after 2 hours of immersion in 3.5 wt.% NaCl solution.....	56
Figure 30. Equivalent electric circuit used for fitting the experimental EIS data for (a) polished carbon steel, (b) Ni-P and Ni-P-0.75ZrC nanocomposite coatings.....	56

Figure 31. (a) Nyquist plot for carbon steel and the as-fabricated metallic coatings Ni-P and Ni-P-0.75g/L ZrC in 3.5 wt% NaCl solution (b) variation of R_{po} and R_{ct} on carbon steel substrate, Ni-P coatings, and Ni-P-0.75g/LZrC nanocomposite coating.57

Figure 32. Tafel profiles of the steel sample, Ni-P and Ni-P-0.75ZrC nanocomposite coating.....58

ABBREVIATION

XRD	X-Ray Diffraction
XPS	X-ray photoelectron spectroscopy
EIS	Electrochemical impedance spectroscopy
DC	direct current
PC	pulse current
PRC	pulse reverse current
SEM	Scanning electron microscopy
TEM	transmission electron microscopy
EDS	energy dispersive spectroscopy
NACE	National association of corrosion engineers
GDP	gross domestic product
TRL	technology readiness level
AFM	Atomic force microscopy

CHAPTER 1: INTRODUCTION

1.1 Background

Corrosion has a large share in the failure of equipment and processes. It is the gradual deterioration of the metallic surface due to the chemical reaction with its environment. Corrosion behaves like a slow poison for the industry utilizing metal in any form, from the raw materials to finished products and from metallic machinery to pipelines of onshore and offshore sites. It plays a significant role in the failure of various products and hinders the efficiency of many application like pipeline, marine and offshore structures [1-4]. Fatigue stress initiation and creep failures are also rooted back to a corrosion-related failure in heavy operating condition along with a sour corrosive environment [5]. Nearly 10-30 per cent of the maintenance budget is spent on corrosion control by the oil and gas refinery plants [6]. Estimation based on the IMPACT-NACE report of 2013 gives the global cost of corrosion to be US\$2.5 trillion in 2013, which is equivalent to 3.4% of the Gross Domestic Product (GDP) [7].

Understanding the fundamentals of corrosion mechanism has led to the development of various surface modification techniques to minimize corrosion. Surface modification techniques provide a dual benefit of corrosion prevention and modification of the surface characteristics to enhance its properties rather than replacing the bulk material to provide respective mechanical properties such as hardness, abrasion, wear and erosion. There are various surface modification techniques, namely carburizing, nitriding, carbonitriding, coating, flame hardening, laser hardening, chemical vapor deposition and physical vapor deposition, to improve the surface characteristic depending upon the demand of the industry. Coating the base metal with a corrosion-resistant layer of varying thickness to provide a barrier between the corroding environment and base metal to protect it from corrosion is one of the established surface modification technique [8].

Coatings of various types are widely known in the industry, such as bitumen, epoxy, metallic and polyolefin system. Coating bearing all the required properties, namely wear resistance, improved hardness, corrosion resistance, and decent erosion resistance, are scarcely reported in the literature. Metallic or inorganic coatings can answer some of the critical challenges of the oil and gas industry owing to their enhanced anti-corrosive properties, wear and abrasion resistance, ease of fabrication, and cost-effectiveness. Due to this reason, protective inorganic coatings are preferred options in the circumstances susceptible to mechanical damage such as wear, fatigue, creep, erosion, etc., in a corrosive environment. The development of alloys and composites in the metallic coating has further attracted researchers in tailoring the properties of the coat by altering chemical bath composition and optimizing various deposition parameters. Advancement in the technology has further led to the production of nanomaterials which find their application in the development of nanocomposite coating to improve mechanical properties along with corrosion resistance.

1.2 Overview of the State of the Art

Nickel electrodeposition can be traced back to 1837, when Bird obtained a crust of metallic nickel on a platinum electrode during the electrolysis of nickel chloride or nickel sulphate. J. Shore of England was granted the first patent for commercial nickel plating through nickel nitrate solution in 1840. Electrodeposition of nickel over a substrate is a well-established concept, although its optimization and compositions for improved results are still studied [9]. A review of Zhang et al. provided the development in nanocomposite coating of the last century and concluded magnetron sputtering as the best fabrication route [10]. Pulse electrodeposition of nickel was firstly studied by Qu and team in 2003, making a breakthrough in the fabrication route of nickel-based coating [11]. The concept of nickel-based nanocomposite coating was rigorously studied with various methods of electrodeposition. Chen et al. studied the incorporation

of Al₂O₃ and concluded the improvement in wear resistance of nickel coating [12]. Borkar and Sandip reported improvement in microhardness of nickel matrix by Al₂O₃, SiC and ZrO₂ nanoparticles and concluded the superiority of pulse deposition over direct current electrodeposition [13]. Improvement in oxidation resistance was observed by many researchers as a result of ceria nanoparticles in the nickel matrix [14, 15]. A brief overview of nickel-based nanocomposite coating is provided in table 1.

Table 1. A brief overview of nickel-based nanocomposite coatings. DC: Direct Current, PC: Pulse Current, PRC: Pulse Reverse Current Electrodeposition techniques.

Matrix	Reinforcement	Deposition		Coating	Reference
		Method		Characteristics	
Ni	Al ₂ O ₃ , SiC, ZrO ₂ (nano)	DC, PC, PRC		Microhardness and wear resistance	Borkar 2011 [13]
Ni	Al ₂ O ₃ sub micron	PC		Wear resistance	Chen 2006 [12]
Ni	TiC nano	PC		Microhardness	Kartal 2017 [16]
Ni	CeO ₂	DC		Wear, corrosion and oxidation	Qu 2006 [14]
Ni	None	PC		Hardness	Qu 2003 [11]
Ni	SiC sub microns	DC		Wear	Walsh 2015 [17]
Ni	ZrO ₂	PC, PRC		Hardness and wear	Wang 2005 [18]
Ni	None	DC, PC, PRC		Comparative	Wasekar 2016 [9]
Ni	CeO ₂	DC, PC, PCU		Oxidation resistance	Xue 2010 [15]

Alloying of nickel with tungsten, iron, phosphorus, and boron to improve the properties of nickel coating has been widely reported in the literature. Ni-P coating has gained much attention during the last decade due to its adaptability to a wide range of environmental and working conditions when the compositions of chemical bath and deposition conditions are carefully selected based on the requirement by varying the electrolyte from sulfate and sulfamate to methanesulfonate bath [19]. Ni-P alloys have found applications in aerospace, electronics and automotive industries due to their wear resistance capabilities, lower friction coefficient and anti-corrosive characteristics [20]. Ni-P has the edge over other alloy coatings such as Ni-Cu, Ni-Fe and Ni-Co and even Ni composites for the fabrication of microsystems, a recent doctoral thesis in the literature by Sadeghi describing various aspects of nickel phosphorus-based nanocomposite coating [21]. Although nickel-phosphorus (Ni-P) coatings have shown promising anti-corrosive properties, the amount of phosphorus in the deposit has an adverse effect on the mechanical properties, namely wear and erosion which restricts their application. Various methods are adopted to overcome this challenge, like the formation of complex alloys, fabrication of multilayer coats and development of composite coatings. Nanocomposite coating, which involves the codeposition of nanoparticles suspended in the chemical bath, has emerged as the most effective way due to its ease in fabrication, simple methodology and cost-effectiveness.

Fabrication of Ni-P based nanocomposite coatings through electroless method is widely studied in the literature. Fayyad et al. studied C_3N_4 and TiNi nano reinforcement in Ni-P matrix, and results indicated improvement in the corrosion resistance along with enhancement in the microhardness [22, 23] and concludes to be corrosion resistant [22-26]. Graphene reinforcement was recently studied by Rana et al., and results indicated the improvement in wear resistance and hardness of the coating [25]. Similar

improvement in the wear resistance was observed for TiO₂ and MoS₂ by Saravanan et al. [26] and Zou et al. [27]. Multilayer coating with YSZ was investigated by Luo et al. and concluded the improvement in microhardness, corrosion and wear resistance. In spite of appreciable results, electroless codeposition is costlier, with slow deposition rate, energy-intensive and contaminated final product inhibit the up-gradation of TRL from laboratory scale to pilot plant scale (TRL 4-6).

Direct current electrodeposition of Ni-P was comprehensively studied by Nava et al. [20], and the effect of heat treatment were enumerated by an increase in hardness of the Ni-P coatings. Codeposition of Y₂O₃ nanoparticles resulted in the enhancement of mechanical and corrosion resistance as investigated by Bahgat Radwan and coworkers [28]. He and team [29] investigated WS₂ reinforcement and remarked the hydrophobic and self-lubricating properties. Various studies for SiC particles concluded upgradation in tribological, mechanical and corrosion resistance [30-32]. Sheu et al. concluded an improvement in the hardness of the Ni-P matrix with the incorporation of Al₂O₃ particles [33]. Electrodeposition coating has gained wide acceptance in academia and industries due to its cost-effectiveness, simplicity, and capability to produce an expeditious result. In spite of various advantages, conventional DC electrodeposition provides continuous nucleation, which results in the agglomeration and aggregation at the coating interface. More details of Ni-P coatings can be read in the comprehensive review recently drafted by Lelevic and Walsh [34].

Pulse electrodeposition is a new technique than electroless and conventional electrodeposition. Its application in nickel-based coating was firstly investigated by Qu et al. [11]. Huo et al. studied the effect of heat treatment and operating conditions of pulse electrodeposition and concluded an upgradation in the wear and microhardness of the Ni-P coatings. Elias and colleagues concluded the improvement in the corrosion

resistance of multilayer Ni-P coatings [35]. As pulse electrodeposition are assumed to overcome the challenges of conventional electrodeposition, very few reinforcements like SiC, WC and Al₂O₃ are utilized to explore the intent potential of pulse electrodeposition due to its complexity and optimizing of many parameters like duty cycle, peak current density, pulse on time, pulse off time and composition of the electrolyte. It is expected to provide controlled coating thickness, tailor surface morphology and structure and come up with the homogenous distribution of nano additives. Some comparative studies of DC and pulse indicate better results in the case of pulse in nickel and nickel phosphorus-based nanocomposite coatings. Table 2 provides a brief overview of Ni-P nanocomposite coatings along with their coating characteristics.

Table 2. A brief overview of the nickel phosphorus-based nanocomposite coatings. ELS: Electroless, DC: Direct Current, PC: Pulse Current, PRC: Pulse Reverse Current Deposition.

Matrix	Reinforcement	Deposition Method	Coating Characteristic	Reference
Ni-P	Y ₂ O ₃	DC	Mechanical and corrosion resistance	Bahgat Radwan 2018 [28]
Ni-P	None	PC	Magnetic property	Dhanapal 2015 [36]
Ni-P	Multilayer	PC	Corrosion resistance	Elias 2016 [35]

Matrix	Reinforcement	Deposition Method	Coating Characteristic	Reference
Ni-P	C ₃ N ₄	ELS	Microhardness and corrosion resistance	Fayyad 2019 [22]
Ni-P	TiNi	ELS	Anti-bacterial and corrosion resistance	Fayyad 2019 [23]
Ni-P	SiC	PRC	Hardness and tribology	Hansal 2013 [37]
Ni-P	WS ₂	DC	Hydrophobic and self-lubricating	He 2017 [29]
Ni-P	SiC	PC , DC	Tribology	Hou 2006 [30]
Ni-P	None	PC	Wear and hardness	Hou 2007 [38]
Ni-P	multilayer YSZ	ELS	Microhardness, corrosion and wear resistance	Luo 2017 [24]
Ni-P	None	DC	Microhardness, corrosion and wear resistance	Nava 2013 [20]
Ni-P	Graphene	ELS	Hardness and wear	Rana 2019 [25]

Matrix	Reinforcement	Deposition Method	Coating Characteristic	Reference
Ni-P	TiO ₂	ELS	Wear	Saravanan 2020 [26]
Ni-P	Al ₂ O ₃	DC,PC	Hardness	Sheu 2013 [33]
Ni-P	SiC	DC	Corrosion resistance	Yuan 2009 [31]
Ni-P	WC	DC, PC	Microhardness	Zoikas 2009 [39]
Ni-P	SiC	DC, PC	Microhardness	Zoikas 2010 [32]
Ni-P	MoS ₂	ELS	Friction and wear	Zou 2006 [27]

1.3 Missing Point in the Literature

Following are some of the gap in the literature described as:

Although electrodeposition is considered to be superior to conventional electroless deposition in the fabrication of nickel-based and nickel phosphorus-based nano composite coatings. Its potential is not completely identified. Hence, it is worth investigating the potential of electrodeposition in the fabrication of nanocomposite coatings.

Nickel phosphorus coatings are proven to be corrosion resistant, but the reported results for nanocomposite coatings lack a quantifiable approach as the findings vary from ‘interesting’, ‘good’ and ‘appreciable’ without concise and comparable procedure generalized for evaluation of the performance of nanocomposite coating.

Various nano reinforcements which provided excellent results with nickel matrix-like

ZrO₂, TiC and ZrC are not being investigated with nickel-phosphorus matrix employing electrodeposition.

Most of the reinforcements are sub-micron and micron-sized. Hence it is the need of the hour to study the effects of nanoparticles incorporation as properties at nanoscale changes exponentially.

1.4 Goals and Objectives

This project aims at delivering a novel solution for corrosion protection along with the improvement in mechanical properties as per the requisites of offshore oil and gas equipment to minimize the operating cost by cutting down the cost of corrosion. Electrodeposition technique will be used to fabricate nanocomposite coatings through optimizing parameters and chemical bath composition. Nickel phosphorus-based nanocomposite coatings with enhanced mechanical characteristics will be fabricated and tested at the well-equipped testing facilities at Qatar University. The project will also aim to bring about a concise and comparable procedure for the evaluation of corrosion resistance. Rare and exceptional nanomaterials with amazing properties will be selected for the fabrication of nickel phosphorus-based nanocomposite coatings to explore the scientific advantages at the nanoscale. The objectives of the project are:

- To develop nickel-based nanocomposite coatings by optimizing the parameters through electrodeposition technique.
- To characterize the synthesized nanocomposite coatings through state-of-the-art testing facilities of Qatar University.
- To study the compositional, structural, morphological, mechanical and corrosion protection properties of the developed nanocomposite coatings.

CHAPTER 2: MATERIALS AND METHODS

2.1 Materials

Nickel sulphate hexahydrate, nickel chloride hexahydrate, boric acid, orthophosphoric acid, and sodium hypophosphite were bought from Sigma Aldrich, Germany. Sodium chloride, titanium carbide (TiC) and Zirconium Carbide (ZrC) powder with the average particle size < 80 nm and purity of 99.9% were imported from Sigma Aldrich. Mild steel sheets locally purchased were used as substrates.

2.2 Sample Preparation and coatings synthesis

The electrodeposition of Ni-P and Ni-P-TiC composite coatings was carried out on the mild steel substrate. Firstly, the mild steel sheet was cut down to the 32mm square sheets through sheet metal operation. The mild steel samples were then polished to obtain a mirror-like surface with SiC abrasive papers of grit size 120, 220, 320, 500, 800, 1000, and 1200. The substrates were washed with soap and water before moving to the following abrasive paper. After grinding, the substrates were sonicated in acetone for half an hour. One side of the substrates was covered with insulating tape to avoid electrodeposition on both sides of the substrates. The substrates were activated in 20% HCl solution for about 45 seconds, rinsed in distilled water, and finally put in the coating bath. During the electrodeposition process, the dc power supply's negative electrode was connected to the substrate forming a cathode, and the positive electrode of the power supply was connected to the nickel sheet to provide an anode. The schematic diagram of the electrodeposition experimental setup is represented in Figure 1. The nickel sheet (anode) and the substrate (cathode) were placed parallel and face to face each other at a distance of approximately 30 mm in the coating bath. The optimized electrodeposition conditions are tabulated in Table 3. Ni-P, Ni-P-TiC and Ni-P-ZrC composite coatings were developed at $65^{\circ}\text{C} \pm 2$. The time of the coatings is

half an hour from the start of the power supply. The coating bath was agitated at 300 ± 5 rpm for 60 minutes before initiating the electrodeposition process to avoid settling down the reinforcement nanoparticles. The coating bath was kept agitated during the entire coating process at 300 rpm for uniform distribution of reinforcing particles into the Ni-P matrix.

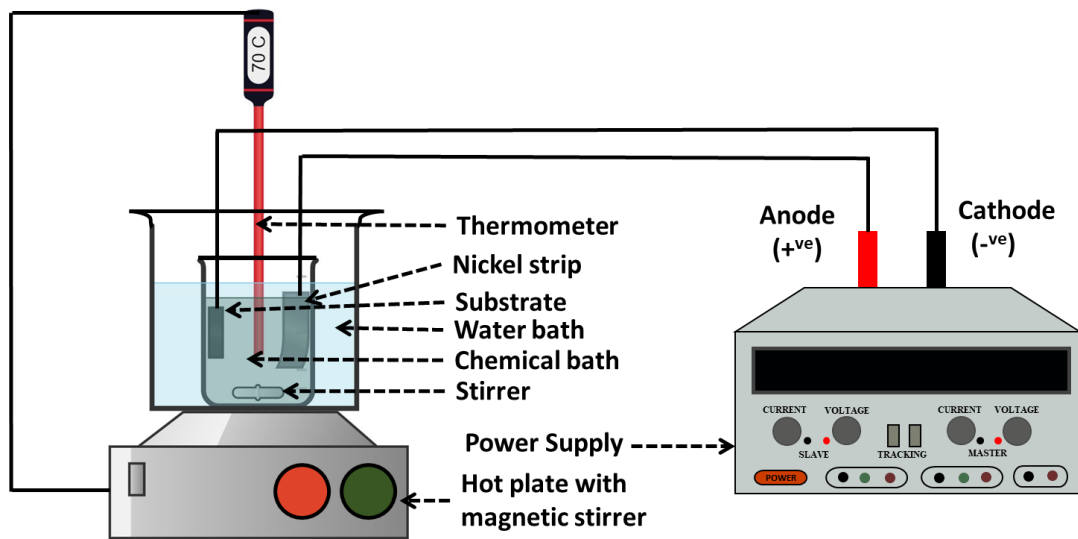


Figure 1. Schematic diagram of the electrodeposition process to develop Ni-P-TiC composite coatings.

Table 3. Optimized bath composition and parameters for co-electrodeposition of Ni-P-TiC composite coatings.

Chemical bath and Operating conditions	Bath Ni-P-TiC	Bath Ni-P-ZrC
Nickel Sulfate hexahydrate	250 g/L	250 g/L
Nickel Chloride hexahydrate	15 g/L	15 g/L
Boric acid	30 g/L	30 g/L

Chemical bath and Operating conditions	Bath Ni-P-TiC	Bath Ni-P-ZrC
Sodium Chloride	15 g/L	15 g/L
Phosphoric acid	6 g/L	6 g/L
Sodium Hypophosphite	20 g/L	20 g/L
TiC concentration	0, 0.5g/L, 1 g/L,1.5g/L and 2 g/L	-
ZrC concentration	-	0.75g/L
pH	2.0 ± 0.2	2.0 ± 0.2
Bath temperature	65±2°C	65±2°C
Deposition time	30 minutes	30 minutes
Current density for TiC	50 mA cm ⁻²	-
Current density for ZrC	-	48 mA cm ⁻²
Bath agitation	300 rpm	300 rpm

2.3 Characterization of composite coatings

2.3.1 Compositional Characterization

2.3.1.1 X-Ray Diffraction

Structural characterization of the synthesized coatings was carried out by employing an X-ray diffractometer (PANalytical, Empyrean, UK) fitted with Cu K α radiations with the scanning step of 0.02° in the range of 2 θ from 10° to 90°.

2.3.1.2 X-ray photoelectron spectroscopy

The composition of the prepared coatings was also determined by X-ray photoelectron spectroscopy- XPS (Kratos Analytical Ltd, UK) using a monochromatic Al-K α X-Ray source.

2.3.2 Morphological Analysis

2.3.2.1 Scanning electron microscopy (SEM) and transmission electron microscope (TEM)

The field emission scanning electron microscope (FE-SEM-Nova Nano-450, Netherlands) and high-resolution transmission electron microscope (HR-TEM FEI: TECNAI G2 FEG 200kV) were used to perform the morphological study.

2.3.2.2 AFM

The atomic force micrograph was obtained by employing the AFM device MFP-3D Asylum research (USA) equipped with silicon probe (Al reflex coated Veeco model-OLTESPA, Olympus; spring constant: 2 Nm^{-1} , resonant frequency: 70 kHz). All measurements were carried out under ambient conditions using standard topography A.C. air (tapping mode in the air).

2.3.3 Mechanical Properties

2.3.3.1 Microhardness

The hardness of the prepared coatings was tested with a Vickers microhardness tester (FM-ARS9000, USA). The measurement of the microhardness was carried out at respective weights with the dwell time of 10 seconds on the surface of nanocomposite coatings.

2.3.3.2 Nanoindentation

The nanoindentation measurements were performed employing AFM device MFP-3D Asylum research (USA) equipped Berkovich diamond indenter tip with a maximum 1mN indentation force (loading and unloading rate: $200 \mu\text{N/s}$ and dwell time at maximum load: 5s). Oliver and Pharr's method was used to find contact penetration from the unloading curves.

2.3.3.3 Wear

Wear performance of the as-prepared coatings was investigated by pin/ball on-disk/plate tribometer (MFT-5000F, Rtec Company) in which nanocomposite coatings were attached to disk and the counterparts were stainless steel balls. The sliding speed was made constant at 0.13 m s^{-1} during the test with a static diameter of wear track (10 mm), and the rotational speed of the disk was 250 rpm. Wear tests were performed at $25 \text{ }^{\circ}\text{C}$ under 4 N normal loads with a sliding distance of 125 m.

2.3.3.4 Erosion

Erosion testing was done for the as-synthesized nanocomposite coatings using an air-jet erosion tester. Alumina particles were employed as an erodent as it is commonly used for corrosion testing. The particle size of the as-received alumina (Al_2O_3) is in the range of 53-84 μm . The experimental set-up for performing the erosion tests was followed the ASTM G76 [40, 41]. The erodent particles flowed with a 0.94 g min^{-1} feed rate, then ejected from the nozzle with a velocity range from 19 to 101 m s^{-1} . The nozzle diameter is 2 mm, and the particle speeds were calculated based on the double-disc approach as Ruff and Ives presented a brief elucidation for calculating the particle speed by directly adjusting the gas pressure. The working distance between the nozzle outlet and the test specimen is 10 mm. the coating sample was mounted on the sample holder facing the nozzle with a 90° incident angle for different exposure times to achieve the maximum effect of surface deformation and depth. The depth and volume loss measurements for the exposed specimens measured using 3D- optical surface metrology system Lecia DCM8 profilometer.

2.3.4 Corrosion Assessment

2.3.4.1 Electrochemical Impedance Spectroscopy

. The electrochemical impedance spectroscopy (EIS) studies were carried out with

Gamry cell in which saturated silver/silver chloride (Ag/AgCl) was used as the reference electrode, whereas graphite and prepared coated samples were employed as counter and working electrodes, respectively. EIS was measured by AC signal with 10mV of amplitude within the frequency range of 10^5 - 10^{-2} Hz at open circuit potential.

2.3.4.2 Tafel

Potentiodynamic studies were carried out at ambient room temperature with a scan rate of 0.167mVs^{-1} after the determination of open circuit potential for more than 10 minutes of stabilization of the complete cell. A constant surface area of 0.765 cm^2 of all tested samples was exposed to 3.5 wt% NaCl solution in the entire study.

CHAPTER 3: RESULTS AND DISCUSSION

3.1 Properties of Ni-P-TiC nanocomposite coatings

3.1.1 Structural and compositional characterization

The structural analysis of the electrodeposited Ni-P and Ni-P-TiC composite coating was carried out through XRD, and the spectra of NiP and Ni-P-TiC composite coatings containing various compositions of TiC (0, 0.5, 1.0, 1.5, 2g/L) are shown in Figure 2. The semi-amorphous structure of the coatings can be deduced from the broad peaks in all the cases, and the broad peak located at $2\theta \sim 45.5$ can be assigned to the Ni (111) plane of face-centred cubic (FCC) structure. The formation of an amorphous structure can be ascribed to the lattice distortion experienced by the nickel crystal structure due to the presence of phosphorous atoms, which hinders the propagation of face-centred cubic occupancy of nickel atoms [42]. The amorphous nature of the coatings has already been reported [20, 43, 44] along with nanocrystalline structure as reported in the literature [45, 46]. The diffraction peaks of the TiC were not observed in the XRD spectra, probably due to their low contents in the Ni-P matrix. Similar results have also been reported in the literature [24, 47].

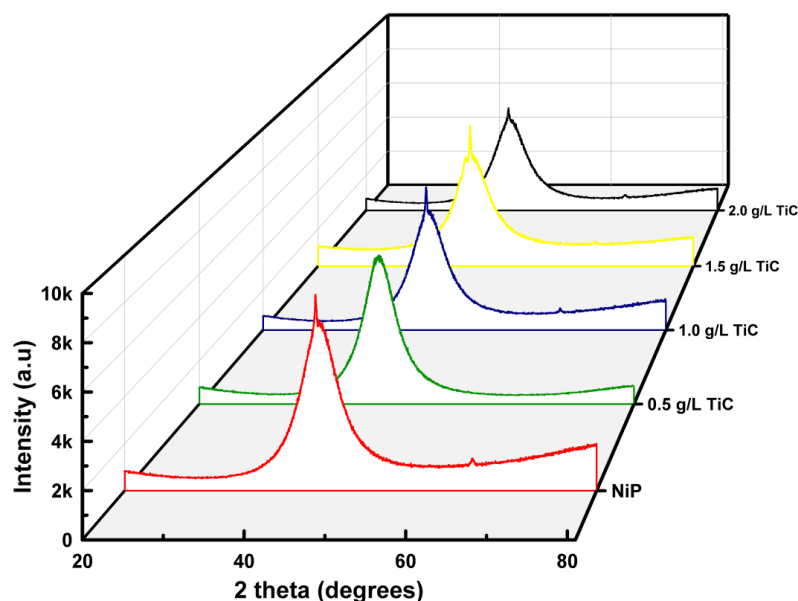


Figure 2. XRD spectra of Ni-P and Ni-P-TiC composite coatings containing various concentrations of TiC particles.

The presence of TiC in the Ni-P TiC composite coatings was confirmed using XPS analysis. To avoid any repetition, the fitted data of individual photoionizations and their corresponding chemical states for only Ni-P with 1.5 g/L TiC composition is presented in Figure 3. High energy resolution spectra of Ni2p (Figure. 3 (a)) region contains two distinct ionizations: Ni 2p_{3/2} and Ni 2p_{1/2} at 852.2 eV and 869.9 eV assigned to Ni in the metallic state, whereas the peaks of Ni²⁺ at 853.3eV, 857.6eV, and 872.7eV corresponds, respectively to the NiO and/or Ni(OH)₂ of Ni 2p_{3/2} and Ni 2p_{1/2}. The high-intensity peak for nickel proves the presence of metallic nickel. The formation of Ni(OH)₂ and NiO can be linked to the presence of hydroxyl ion from the aqueous electrolytic bath and other surface oxidation phenomenon [28, 48]. Concerning the P2p ionization, the peaks at 128.8 and 129.5 eV can be assigned to the elemental phosphorous (P) in the bulk of electrodeposited Ni-P-TiC composite coating, respectively (Figure.3b). It can be noticed that the peak at 130.69 eV is due to (i) elemental phosphorus hypophosphite and/or (ii) intermediate phosphorous ions (P(I)

and/or P(III)) valence, which are presented in the inner portion of the protective film of the Ni-P coatings. However, peaks at 132.7eV can be due to the combination of oxides and/or hydroxides (P_2O_3 and/or P-OH) chemical states [28]. The high-resolution spectra of the Ti2p spectrum were deconvoluted into three doublet peaks (Figure.3c) of titanium carbide, based at 454.9 and 460.8 eV, titanium oxides at 456.1 and 464.8 eV and TiO_2 at 459.2 and 466.4 eV as previously reported [49, 50].

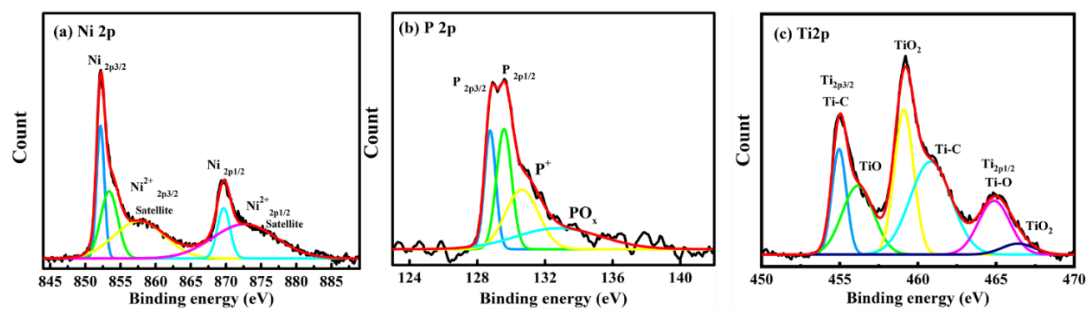


Figure 3. XPS spectra presenting the elemental composition of Ni-P/1.5g/L TiC composite coatings, (a) Ni2p, (b) P2p and (c) Ti2p

3.1.2 Morphological Analysis

The morphology of the Ni-P and Ni-P/TiC composite coatings containing various concentrations of TiC particles was studied with FE-SEM as specified in Figure 4. Ni-P coatings (Figure. 4(a)) does not show the formation of a well-defined nodular structure. A similar morphology of Ni-P coatings has been reported in the literature [24, 51]. On the other hand, FE-SEM micrographs of Ni-P-TiC composite coatings (Figure. 4(b-e)) show the compact, nodular morphology without any noticeable defects. The presence of TiC particles can also be observed in the FE-SEM images, especially at the 2.0 g/l of composition, in good agreement with the literature [28, 52]. Figure 4 (f) shows the cross-section of Ni-P-TiC (1.5 g/L) composite coatings. A smooth and well-adherent coating, without any apparent defects, can be observed, together with a

uniform interface. A uniform coating thickness of $\sim 15\mu\text{m}$ is achieved.

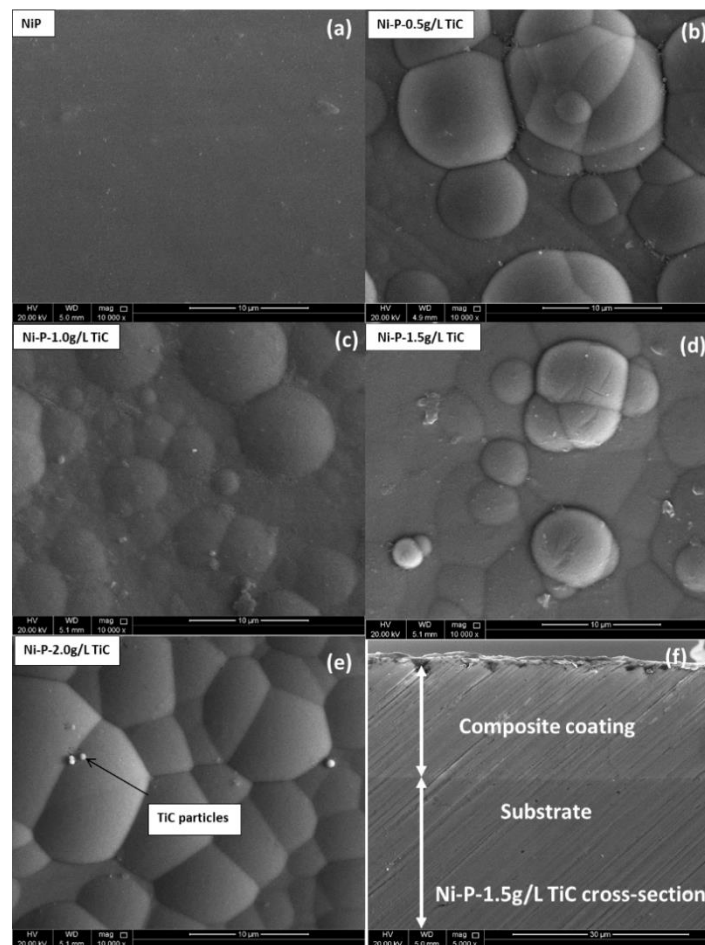


Figure 4. FE-SEM micrographs of the Ni-P (a) and Ni-P-TiC composite coating with various concentrations of TiC (b, c, d, e). A cross-sectional micrograph (f) of Ni-P-TiC composite coatings with 1.5 g/L of TiC.

The coating thickness was also measured with the coating gauge meter and presented in Table 4. It can be noticed that the coating thickness under all identical conditions is similar, and there are no noticeable changes in the thickness. It is worthy of mentioning that the reported values are an average of five readings. A slight difference in thickness

of coatings measured through FE-SEM analysis may be due to the surface preparation required for the test.

Table 3. The average thickness of Ni-P and Ni-P-TiC composite coatings measured with a thickness gauge meter.

Coatings Composition	Average coating thickness
Ni-P	17 $\mu\text{m} \pm 2$
Ni-P 0.5g/L TiC	17 $\mu\text{m} \pm 2$
Ni-P 1.0g/L TiC	17.4 $\mu\text{m} \pm 2$
Ni-P 1.5g/L TiC	17.2 $\mu\text{m} \pm 2$
Ni-P 2.0g/L TiC	17.6 $\mu\text{m} \pm 2$

The co-deposition mechanism of various reinforcements in the Ni-P matrix has been proposed by many researchers. Guglielmi [53] proposed a model containing two steps in which firstly, particles adsorb weakly on the cathode surface by Van der Waals forces and then, during the second stage, strong adsorption by coulombic forces. This model fails to account for particle size and hydrodynamics of the deposition. Bercot et al. [54] formulated a corrective factor to this model for accounting for magnetic stirring in their study, whereas Bahadormanesh and Dolati modified Guglielmi's model for the deposition of a high-volume percentage of the second phase and carried out a parametric study [55]. Moreover, Fransær et al. devised a trajectory model in which they presented an analysis of various forces on a spherical particle in a rotating disk electrode system [56]. According to Ceils et al. [57], the electrodeposition mechanism may consist of five steps; (i), formation of an ionic cloud around the reinforcement particles, (ii) movement of reinforcement particles by forced convection towards the

hydrodynamic layer of the cathode, (iii) diffusion of the particle through double layer, (iv) adsorption of the particle along with the ionic cloud at the cathode surface and (v) reduction of the ionic cloud leading to an irreversible entrapment of reinforcement particles in the metal matrix. As per the above discussion, it seems there are mainly three steps involved in the co-deposition of the reinforcement particles, such as TiC during the electrodeposition process; (i) movement of particles from bulk electrolyte to hydrodynamic boundary layer of the cathode which are governed by a combination of forced convection and electrophoresis, (ii) diffusion and adsorption of particles at the cathode due to Van der Waal forces, and (iii) permanent incorporation of particles due to the reduction of ionic cloud around the reinforced particle. This three-step phenomenon can be described in the schematic diagram in (Figure (5)).

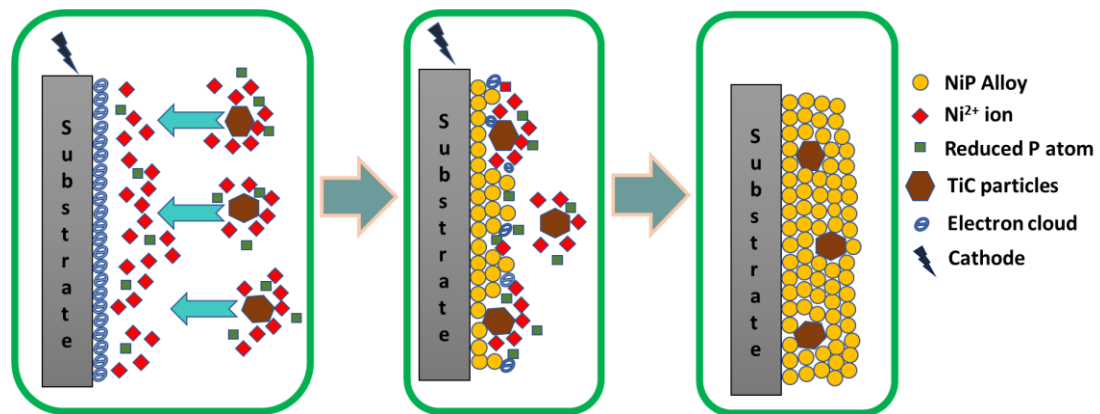


Figure 5. Schematic diagram for the co-deposition of TiC particles at the cathode (substrate) to form Ni-P-TiC composite coatings.

The co-electrodeposited of TiC in the Ni-P matrix was further evaluated with EDS analysis. The EDS analysis of Ni-P and Ni-P-TiC composite coatings containing various concentrations of TiC particles is presented in Figure 6 (a-f). The elemental mapping of Ni-P /TiC composite coatings is shown as an inset of Figure 6. The presence

of titanium (Ti), carbon (C), Phosphorus (P), and nickel (Ni) confirm the incorporation of TiC particles into the Ni-P matrix. Table 5 shows the weight percentage of various elements in the as-prepared composite coatings. As for Ni-P coating, nickel constitutes almost 89.51 wt.%, and the remaining is balanced by phosphorus. Introduction and increase of the concentration of TiC powder in the chemical bath do affect the concentration of nickel in the deposit, which appreciably decreases without significant effect over the phosphorus content, which remains around ten wt.% in all the coatings. The titanium content in the deposits increases from 0.39 wt.% to 0.84 wt.% when the concentration in the chemical bath is increased from 0.5g/L to 2.0g/L. However, the excessive weight percentage of carbon can be attributed to the combination of various effects such as the presence of carbon in the titanium carbide compound, impurities related to the environment and surface preparation for the microscopic analysis. The incorporation of TiC particles can be inferred from the titanium peaks in the EDS plot of 0.5,1.0,1.5 2.0 g/L and a cross-section of 1.5g/L of TiC. Peaks of iron are also observed in the cross-sectional EDS analysis which can be ascribed to the steel substrate. Further, corresponding EDS elemental mapping results shown as an inset of corresponding compositions depict the clear distribution of Ni, P, and TiC particles in the Ni-P matrix.

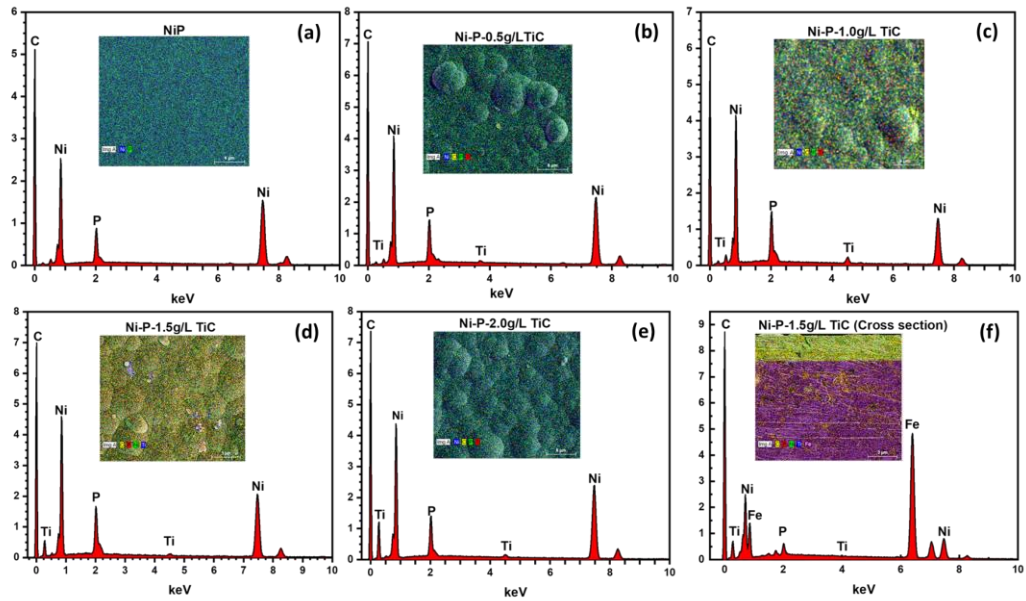


Figure 6. EDS analysis along with elemental mapping of Ni-P (a) and various compositions of Ni-P-TiC composite coatings; (b) 0.5g/L (c) 1.0g/L (d) 1.5g/L (e)2.0g/L and (f) cross-section of 1.5g/L of Ni-P-TiC composite coatings.

Table 4. EDS quantitative analysis of Ni-P and Ni-P-TiC composite coatings.

S. No	Sample Designation	Ni (wt.%)	P (wt.%)	Ti (wt.%)	C (wt.%)
1	Ni-P	89.51	10.49	-	-
2	Ni-P-0.5g/L TiC	73.47	9.94	0.39	16.2
3	Ni-P-1.0 g/L TiC	69.74	9.82	0.64	19.8
4	Ni-P-1.5 g/L TiC	66.19	10.52	0.79	22.5
5	Ni-P-2.0 g/L TiC	66.58	9.68	0.84	22.9

In order to further investigate the microstructural properties of the deposit, high resolution transmission electron microscopy analysis was carried out for the Ni-P-2.0g/L TiC. Figure 7 shows the TEM bright-field micrographs of electrodeposited Ni-P-2.0g/L TiC composite coating at various magnifications. All the images clearly reveal the presence of a separate second phase of TiC particles within the Ni-P matrix. Figure 7(a) presents a low magnification micrograph of the composite coating. The excessive darkness is due to the thickness of the coating deposited on the copper grit for TEM analysis. Figure(7 b) is the enlarged image at the marked location (B) in Figure7 (a) presenting the amorphous structure of the composite coating with the lighter region corresponding to the nickel lattice formation, as also reported by Huang et al. in their exhaustive study of microstructure in the Ni-P coating [58]. An irregular dark network is observed in Figure 7(b), which is prevalent to the mid-high phosphorus content within the electrodeposited composite coatings as previously reported [58, 59]. Figure 7(c) is the micrograph at very high magnification presenting the cubical polygonal structure of the reinforced titanium carbide embedded in the Ni-P matrix. The matrix-reinforcement interface can be clearly distinguished as comparatively sharp contrast can be identified in the micrographs. According to the literature, titanium carbide particles are reported to have a regular polygonal cubical structure [60].

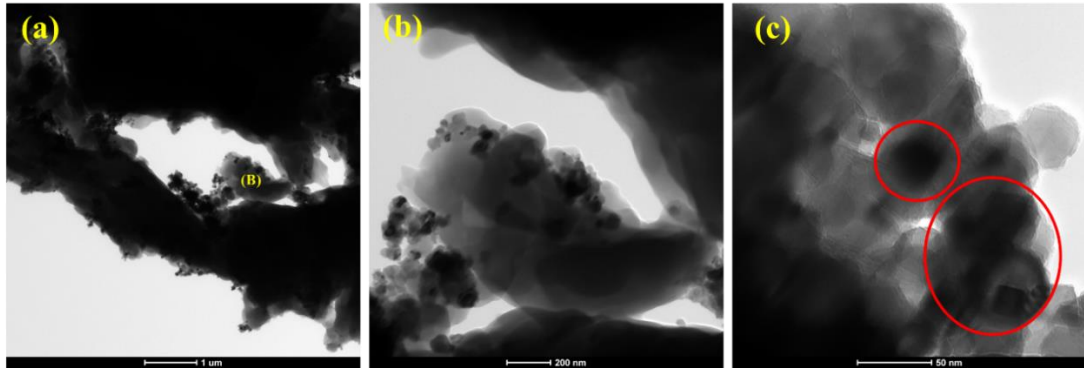


Figure 7. TEM micrographs of Ni-P-2.0g/L TiC at a various magnification of (a)high magnification (b)magnified portion marked (B) in (a) and (c) showing an interface of the Ni-P matrix and TiC reinforcement.

FE-SEM images could not accurately provide evidence of aggregation or agglomeration of TiC particles during the fabrication of the Ni-P-2.0g/L TiC composite coating. TEM analysis further confirms the agglomeration or aggregation of the cubical polygonal TiC particles, which are visible in Figure 8 for the Ni-P-2.0g/L TiC. Agglomeration of the particles in composite coatings has been confirmed through TEM micrograph as reported in the literature [59, 61].

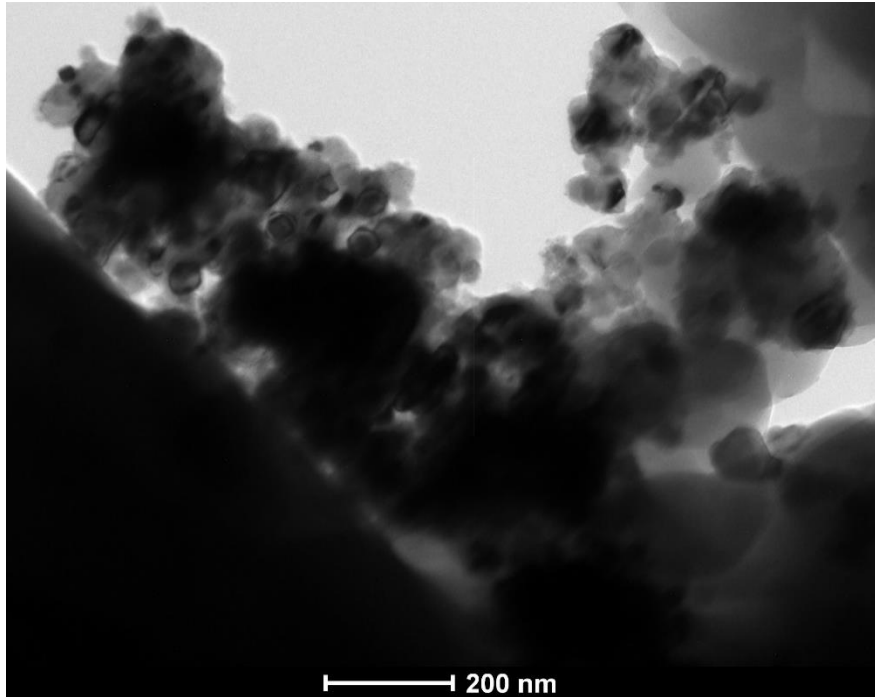


Figure 8. TEM micrograph of Ni-P-2.0g/L TiC presenting the agglomeration of the particles in the Ni-P matrix.

The surface topography of the electrodeposited Ni-P and Ni-P-TiC composite coatings was investigated through atomic force microscopy (AFM). Three-dimensional images of Ni-P and Ni-P/TiC composite coatings with the various compositions of TiC particles are presented in Figure 9 (a-e). It is observed that the Ni-P coatings indicate a relatively smooth surface when compared with the Ni-P-TiC composite coatings. The Ni-P-TiC composite coatings' surface is composed of valleys and intrusions due to the presence of TiC particles into the Ni-P matrix that provides a rougher texture. The quantitative analysis of surface topography indicates that the addition of TiC particles into the Ni-P matrix has resulted in an increase in the surface roughness. The average surface roughness (R_a) increases with the increasing amount of TiC particles, and the average value increased from 6.786nm (Ni-P coatings) to 33.014nm (Ni-P/TiC-2.0 g/L), contributing five times enhancement in the surface roughness. Moreover, R_q (

root mean square value of the roughness) is also presented, which shows a similar trend as the average roughness as presented in Figure 9. Furthermore, Rz values also display a similar increasing trend from 18.6nm roughness of Ni-P coating to the successive increase up to 53.8nm, 58.5nm, 70.2nm and 77.6nm for the increase in the concentration of TiC particles of 0.5g/L, 1.0g/L, 1.5g/L and 2.0g/L in the chemical bath. The increase in the surface roughness with an increasing amount of TiC particles can be attributed to the presence of insoluble and hard ceramic particles, which provides jerks and barriers to the free movement of the AFM cantilever tip. These findings are consistent with the previous studies [24, 28].

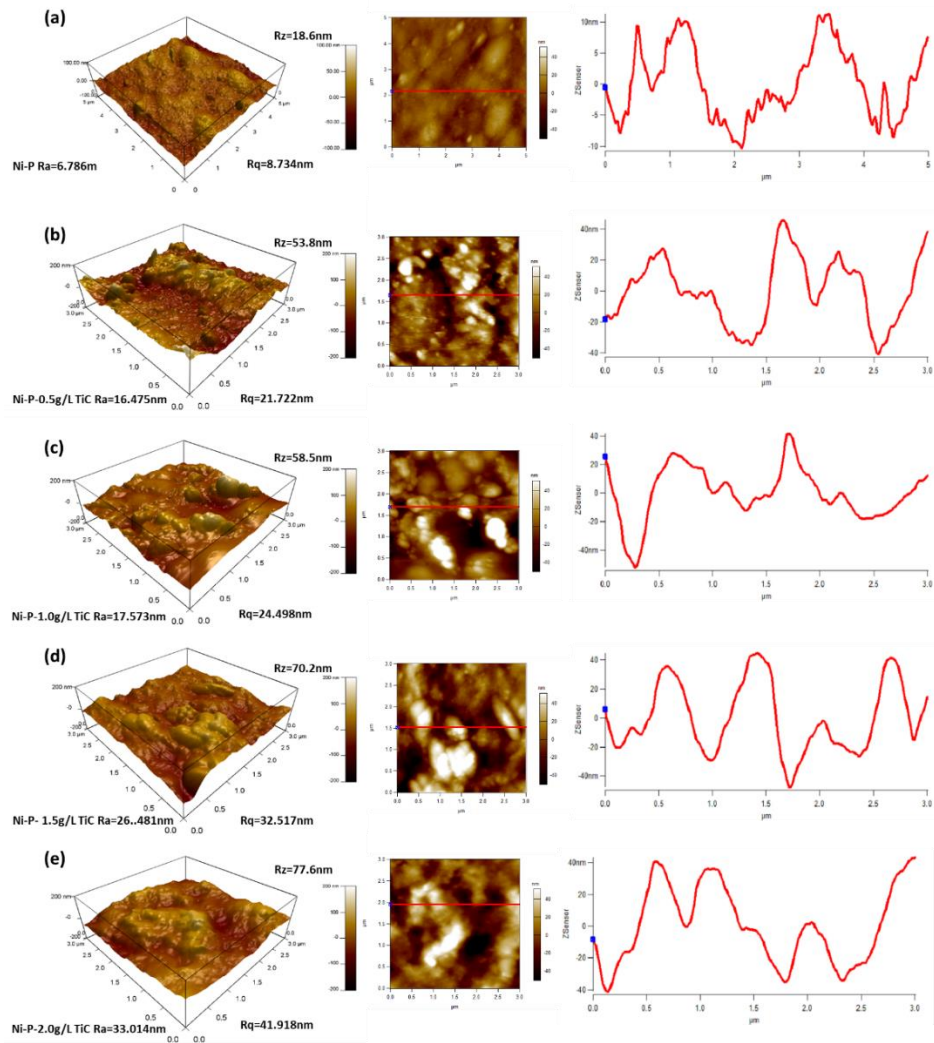


Figure 9. 3D-AFM micrograph along with their corresponding surface roughness profiles of the (a) Ni-P, Ni-P-TiC composite coatings (b) 0.5g/L, (c)1.0g/L, (d) 1.5g/L, and (e) 2.0g/L of TiC particles.

3.1.3 Mechanical Properties

Vickers microhardness results of Ni-P and Ni-P-TiC composite coatings are presented in Figure 10. As seen, Ni-P coating's hardness value is around 500HV, which increases to ~530HV and ~550HV on the incorporation of 0.5g/L and 1g/L of the TiC particles, respectively. The hardness value reaches its maximum value of ~593HV at the composition of 1.5g/L. The increase in the hardness is about 19%, which can be attributed to the dispersion hardening effect and improvement in the load-bearing

characteristics of the matrix due to the formation of a composite structure, aligned to previously reported literature [62, 63]. After reaching its terminal value, the microhardness decreases with further increase in TiC particles, and it decreases to ~550HV at 2.0g/L. A decrease in the hardness value at 2.0 g/L can be attributed to the excessive aggregation of the TiC particles in the Ni-P matrix, which impairs the load-bearing properties of the Ni-P/TiC composite coatings. This observation is also consistent with previous reports[64].

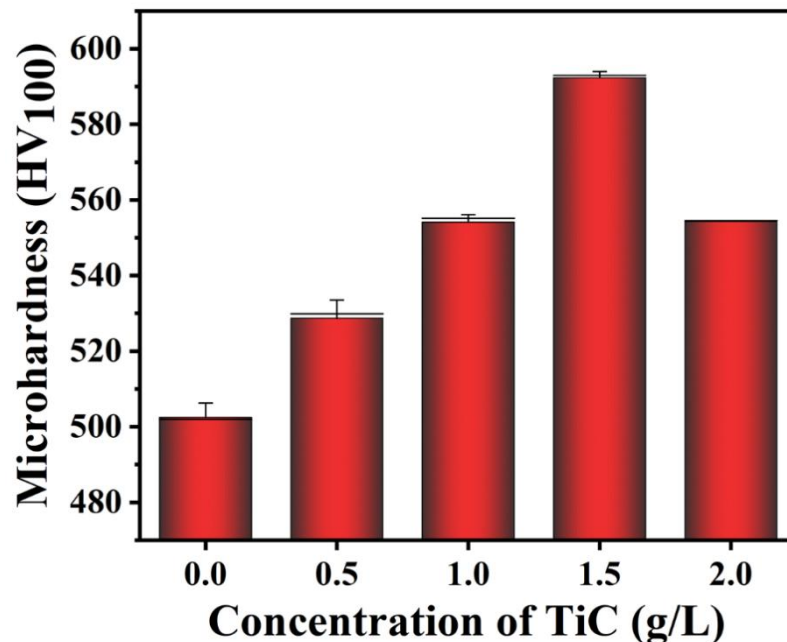


Figure 10. Vickers microhardness of Ni-P and Ni-P-TiC composite coatings containing various concentrations of TiC particles.

The indentation tests of the Ni-P and Ni-P-TiC composite coatings were performed to have an insight into the mechanical response of the developed coatings. The loading/unloading indentation profiles of Ni-P and Ni-P-TiC composite coatings containing various concentrations of TiC particles are presented in Figure 11. A gradual decrease in indentation depth with an increasing amount of TiC particles in the

Ni-P matrix is evident in Figure 11(a). The Ni-P coatings demonstrate an indentation depth of $\sim 50\text{nm}$, which reduces to 23.67nm at the composition of 1.5g/L of TiC. The decrease in depth is due to the enhancement in hardness of the coatings, which is directly associated with the dispersion hardening effect and improvement in the load-bearing properties, as explained previously. It can be further noticed that there is a decrease in indentation depth of $\sim 7\text{ nm}$ at the terminal composition (2.0 g/L TiC). This is because of the fact that an excessive amount of reinforcement accumulates in the matrix and thus harms the mechanical properties are in agreement with previous studies [65, 66]. The maximum decrease in the indentation depth is observed at 1.5g/L of TiC due to the uniform distribution of the reinforcing phase in the matrix without any significant agglomeration. The loading/unloading curves are uniform without any kinks, suggesting that the synthesized coatings are free of cracks and pores. For a more accurate comparison, a quantitative analysis of the indentation results obtained through the Oliver and Pharr technique is also represented in Figure 11(b). It can be noticed that the hardness of Ni-P coatings is 4.96 GPa , which increases with increasing concentration of TiC particles in the Ni-P matrix, reaching its terminal value of 5.98 GPa at the composition of 1.5 g/L . Further increase of TiC particles concentration in the Ni-P matrix decreases hardness, and it attains a value of 5.52 GPa at the TiC composition of 2.0 g/L . This result further supports the observation that incorporation of ceramic TiC increases the hardness of the NiP matrix, in good agreement with the literature [23, 28]. The decrease in the hardness for 2.0g/L can be due to the agglomeration of TiC particles in the Ni-P matrix. The nanoindentation results are in agreement with the Vickers microhardness test results.

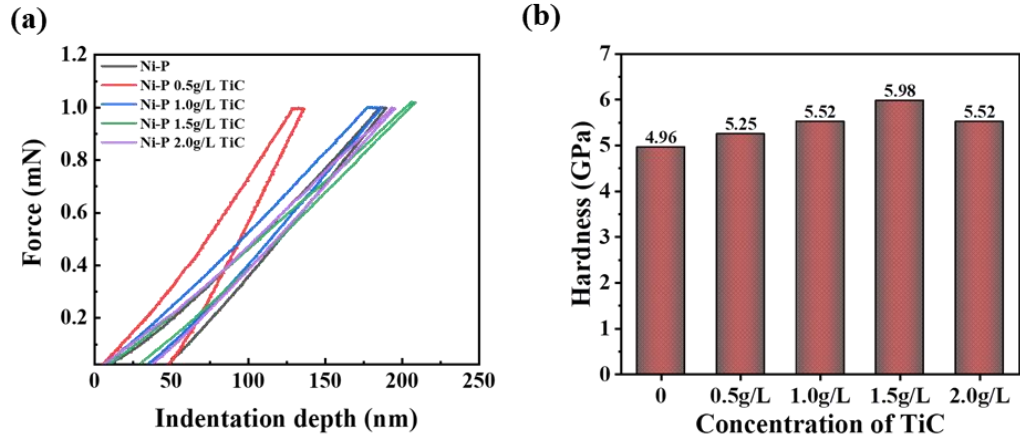


Figure 11. Nanoindentation results of Ni-P and Ni-P-TiC composite coatings containing various concentrations of TiC particles; (a) loading/unloading profiles and (b) hardness.

3.1.4 Corrosion Assessment

The corrosion resistance of the coatings was studied through electrochemical impedance spectroscopy (EIS) and potentiodynamic polarization techniques. The EIS plots (Bode plots) of the substrate (carbon steel), NiP, and NiP-TiC composite coatings containing various concentrations of TiC are presented in Figures 12 (a, b). Experimental data were fitted using an equivalent circuit based on a modified Randle circuit. It is composed of two-time constants in cascade assigned to the composite coatings and metal-coating interface exposed at the bottom of conductive paths, as presented in Figure 13 (a, b). The various elements in the circuit account for R_s - electrolyte resistance, R_{po} - pore resistance, R_{ct} - polarization resistance, and constant phase elements (CPE1 and CPE2) instead of capacitors to account for surface inhomogeneity. The constant phase elements can be calculated by the following equation[28]:

$$\frac{1}{Z_{CPE}} = Q(j\omega)^n \quad 1$$

where Q is the admittance and ω is the angular frequency of the alternating signal and n is the exponent of CPE, which determines the capacitance nature, i.e., when “ n ” approaches unity, the CPE approaches to pure capacitance and the element behaves like an ideal capacitor [28].

Referring to Figure 12, the medium-high-frequency regions of the Bode plot for carbon steel evidence one time constant, while for the coated samples, there is a broadening of the phase angle, suggesting two overlapped time constants – the one associated with the composite coating and another to the interfacial phenomena at the bottom of pores formed in the coating. The magnitude plot indicates that the corrosion resistance of the carbon steel sample is very low $\sim 270 \Omega\text{cm}^2$, a value that was obtained after fitting the experimental data using the proposed equivalent circuit (Figure 13 (a)). Ni-P coatings show an improvement in the impedance value of one order of magnitude, which can be ascribed to the formation of the hypophosphite layer due to electrochemical reactions of the salt solution with the surface of Ni-P coating [67, 68]. The inclusion of secondary phase TiC particles in the Ni-P matrix further changes the impedance response, leading to the broadening of the phase angle plot. This trend indicates, on the one hand, a more protective composite coating (shift towards higher frequencies) and, on the other hand, the presence of other processes (decreased corrosion activity) as previously reported in the literature [28, 69]. The increased impedance in the composite coatings can be attributed to the reduction in the number of active corrosion sites due to the occupancy of inert and corrosion-resistant TiC particles. The Ni-P-0.5g/L TiC showed almost doubled impedance values compared to a simple Ni-P coated sample (Figure.12). An increase in the concentration of TiC particles from 0.5g/L up to 2.0g/L has successively increased the corrosion resistance, and the maximum impedance values for Ni-P-2.0g/L

TiC reaches $23 \text{ k}\Omega \text{ cm}^2$ showing an improvement of $\sim 92\%$ when compared to Ni-P coatings. An increase in the pore resistance can be due to the presence of TiC particles in the pores of the Ni-P matrix that decreases the number of conductive paths and increases the surface roughness, as observed in AFM results [48]. Improvement in the polarization resistance can be related to the successive increase in the reinforcement of TiC particles in the Ni-P matrix, which hinders the electrolyte from reaching the substrate, decreasing the number of active sites and hence providing additional protection against corrosion [28, 48, 69].

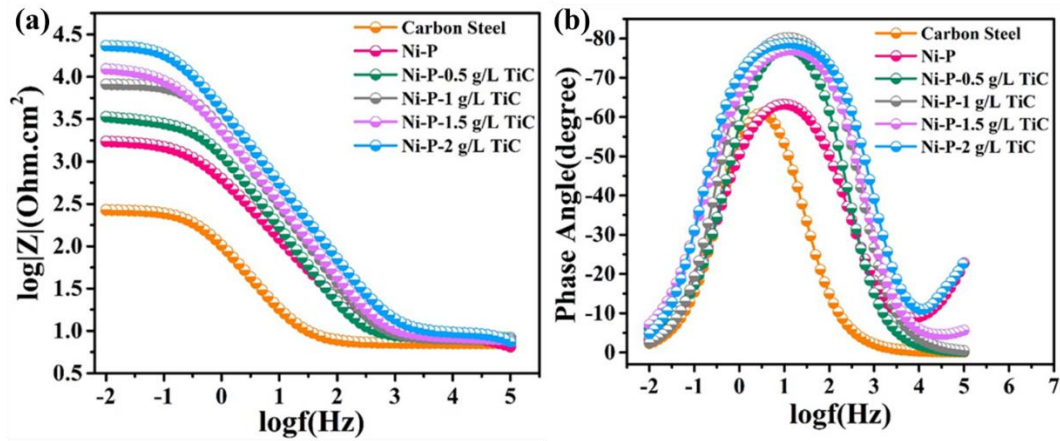


Figure 12. (a) Bode plots of the substrate, Ni-P, and Ni-P-TiC composite coatings containing the magnitude plot and (b) phase angle plot after 2 hours of immersion in 3.5wt% NaCl solution.

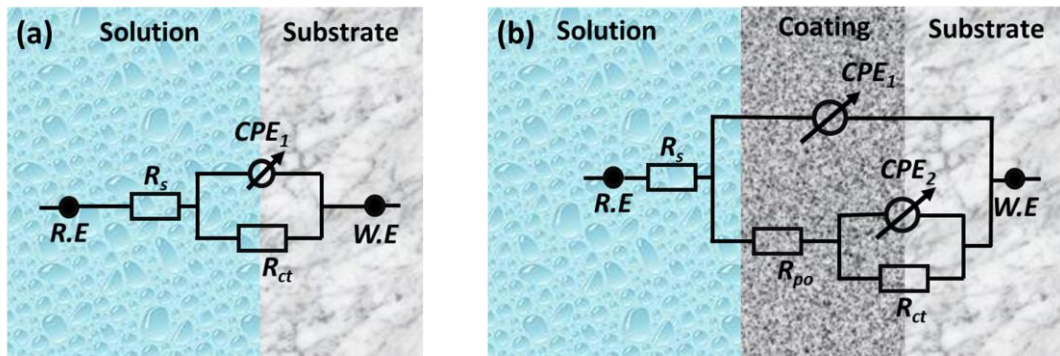


Figure 13. Equivalent electric circuit used for fitting the experimental EIS data for (a) polished carbon steel used as substrate, (b) Ni-P and Ni-P-TiC composite coatings containing different concentrations of TiC particles.

Figure 14 (a) depicts the Nyquist plots for carbon steel (substrate), Ni-P and Ni-P-TiC composite coatings containing various concentrations of TiC particles. Nyquist plots of Ni-P coatings and Ni-P-TiC composite coatings demonstrate distinct capacitive loops. The experimental plots for the coated samples were fitted using the two-time constant equivalent electric circuit described in Figure 13 (b), and the fitting goodness is represented in Figure 14 in the Nyquist plots. The capacitive loop diameter evidences a successive increase, confirming the higher corrosion resistance in the presence of TiC particles. Figure 14 depicts the evolution of the pore resistance and polarization resistance over time. The incorporation of TiC particles in the Ni-P matrix increases the pore resistance in the coating and acts as a barrier by that delays electrolyte uptake. The decrease of the active surface area is responsible for the increase in the polarization resistance (R_{ct}), as shown in Figure 14 (b). Moreover, increasing the concentration of TiC particles in the chemical bath leads to a decrease in the active region and, therefore, increases the corrosion resistance of the composite coatings. The enhancement in the corrosion resistance of the NiP coating in the presence of various concentrations of TiC can be enumerated by the combined effect of (i) Inert TiC particles reduce the active

area in the NiP matrix (ii) TiC particles are assumed to block the pores by filling them and restricting the diffusion of the Cl^- ions towards the metal surface and (iii) double-layer capacitance reduces. These findings are consistent with the previous studies [28, 48, 69, 70].

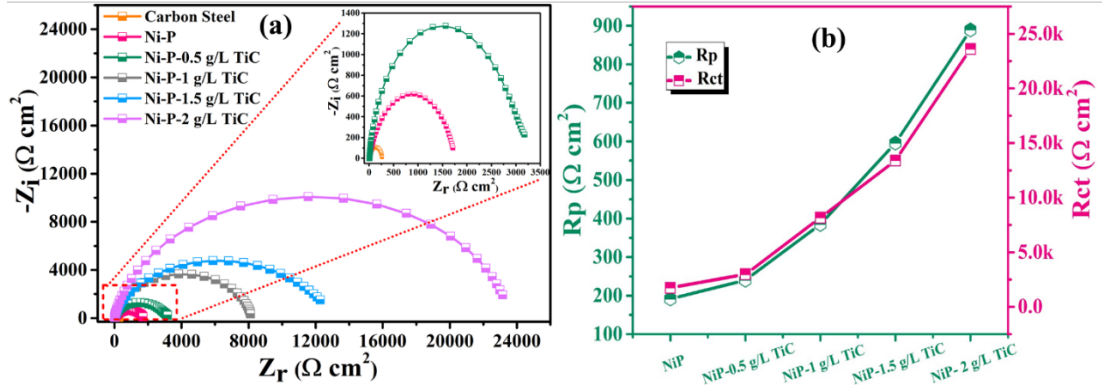


Figure 14: (a) Nyquist plots for carbon steel (substrate) and Ni-P-TiC composite coatings along with fitted resistance values vs the concentration of TiC particles after the 2 hours of immersion in 3.5wt% NaCl solution (b) evolution of R_p and R_{ct} with the TiC.

The corrosion resistance of the carbon steel, Ni-P, and Ni-P-TiC composite coatings containing various concentrations of TiC particles was also studied by d.c. Potentiodynamic polarization employing a scan rate of 0.167mV/sec, as shown in Figure 15. Electrochemical parameters such as corrosion potential (E_{corr}), corrosion current density (i_{corr}), anodic Tafel slope (β_a), and cathodic Tafel slope (β_c) were extrapolated from the fitted curve and tabulated in Table 6. Moreover, the corrosion protection efficiency (PE %) was calculated from the formula reported [28].

$$PE\% = 1 - \frac{i_2}{i_1} \quad 2$$

where i_1 is the current density of the carbon steel and i_2 is the current density of coated

samples. The maximum value of current density ($55.94\mu\text{A cm}^{-2}$) is observed for carbon steel at a corrosion potential of -533mV , the most cathodic one observed in Figure 15. The current density decreases to $38.43\mu\text{A cm}^{-2}$ for the Ni-P coatings and further decreases with increasing concentrations of TiC particles in the Ni-P matrix. Thus, the values of current density decrease to $25.62\mu\text{A cm}^{-2}$, $7.79\mu\text{A cm}^{-2}$, $6.49\mu\text{A cm}^{-2}$ and $4.91\mu\text{A cm}^{-2}$ for the 0.5 g/L, 1.0 g/L, 1.5g/L, and 2.0g/L TiC composite coatings respectively. Moreover, the corrosion potential becomes slightly more anodic for the Ni-P coatings and increases from $\sim -372\text{mV}$ to $\sim -312\text{ mV}$ with increasing concentrations of TiC, suggesting a slight inhibition of the anodic activity in the presence of the TiC particles in the Ni-P matrix. Interestingly, for the TiC concentrations of 1.0, 1.5 and 2.0 g/L, the anodic current density is independent of the content of TiC particles and significantly lower compared to the Ni-P coating. This trend evidences that the anodic activity is reduced in the presence of the TiC particles (for the 3 highest concentrations). However, the cathodic current density tends to increase as the concentration of particles increases, approaching the values observed for the Ni-P coating and steel. This indicates that the cathodic processes, mainly oxygen reduction, are favoured by the presence of TiC particles. The potentiodynamic polarization results show that Ni-P coatings had lower corrosion resistance compared to steel, displaying a corrosion protection efficiency of $\sim 31\%$. In such composite coatings, corrosion often initiates at grain boundaries of the nodules as a result of the adsorption of chloride ions. The anodic activity leads to the formation of soluble NiCl_2 , which can proceed to the formation of pits [71]. The corrosion protection efficiency, a consequence of the decreased corrosion current density, increases with the increasing concentration of TiC particles in the Ni-P matrix. The highest corrosion protection efficiency ($\sim 90\%$) was achieved at a TiC concentration of 2.0 g/L. To conclude, the

inclusion of TiC particles in the Ni-P alloy matrix has improved the corrosion resistance as the concentration of TiC particles. On the one hand, the presence of particles inhibits the anodic reactions, and, on the other hand, it contributes to reducing the number of active sites for the adsorption of chloride ions on the surface defects such as cracks and pores. Enhancement in the corrosion resistance by increased concentration of reinforcement is in good agreement with the literature [28, 72, 73].

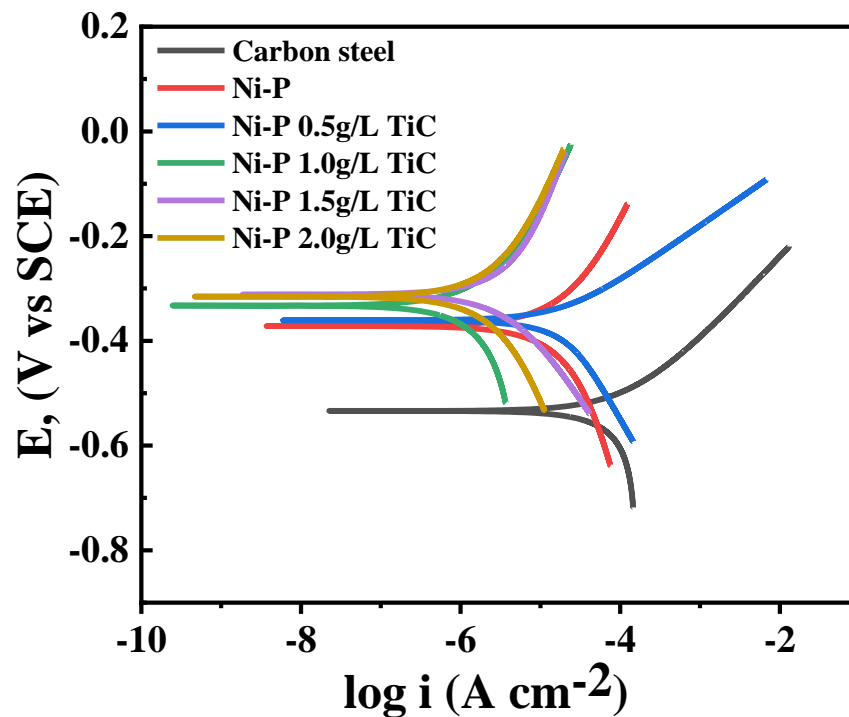


Figure 15. Potentiodynamic profiles of carbon steel, Ni-P and Ni-P-TiC composite coating with increasing concentration of TiC.

Table 5. Electrochemical parameters derived from the potentiodynamic polarization curve of carbon steel, Ni-P, and Ni-P-TiC composite coating containing various concentration of TiC particles.

Composition	β_a (V/decade)	β_c (V/decade)	$i_{corr}(\mu A$ cm ⁻²)	E_{corr} (mV)	PE%
Carbon steel	0.09617	0.2275	55.94	-534.0	
Ni-P	0.3514	0.6088	38.43	-372.0	31.3%
Ni-P 0.5g/L					
TiC	0.1059	0.2664	25.62	-361.0	54.2%
Ni-P 1.0g/L					
TiC	0.4342	0.2902	7.79	-333.0	86.0%
Ni-P 1.5 g/L					
TiC	0.4354	0.2434	6.49	-312.0	88.4%
Ni-P 2.0 g/L					
TiC	0.384	0.4246	4.91	-315.0	91.2%

3.2 Properties of Ni-P-ZrC nanocomposite coatings

3.2.1 Structural and compositional characterization

Structural analysis of the as-prepared Ni-P and Ni-P-ZrC metallic coatings was investigated using XRD, see Figure 16. The broad peak in the spectra of Ni-P and Ni-P-ZrC metallic coatings indicates the amorphous structure of the as-prepared coatings. The peak at $2\theta = 45$ represents a face-centred cubic lattice structure of Ni (111) plane, which has been disturbed by the incorporation of phosphorus atoms resulting in the entire structure being amorphous, which is consistent with the previous finding [42, 43, 74]. Peaks of ZrC cannot be distinguished in the spectra due to the low concentration of ZCNPs, and also, the broad peak of amorphous Ni may have shielded the peaks of

ZCNPs [24, 47]. The broad peak of nickel has sharpened in Ni-P-ZrC nanocomposite coatings, which could be attributed to the presence of ZCNPs, leading to a shift in the structure from amorphous to semi-amorphous [42]. However, as a comparison, the XRD spectrum of ZCNPs shows a well-defined crystalline behavior.

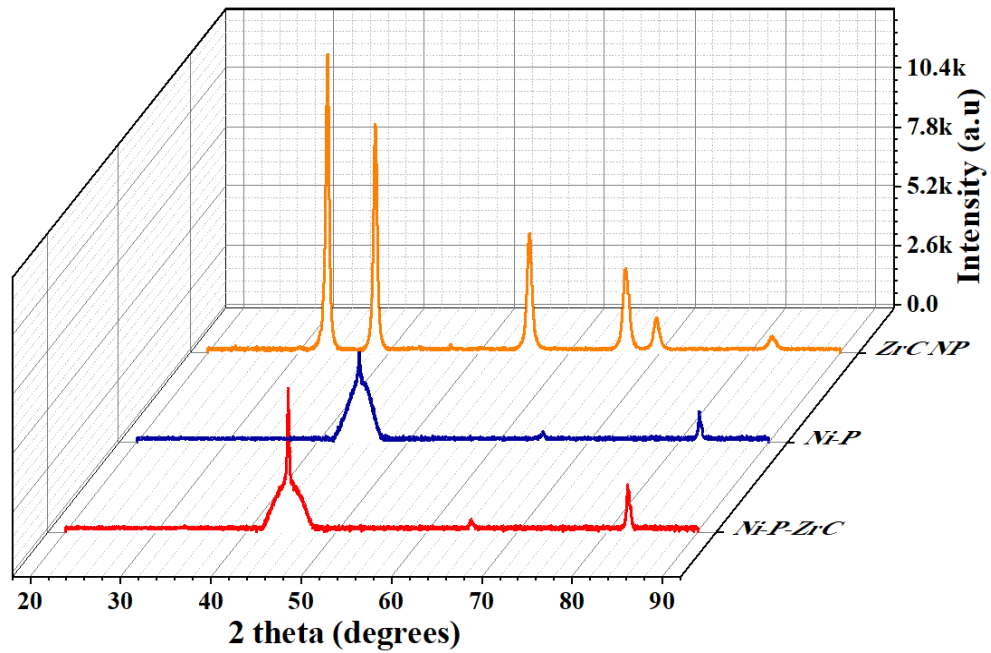


Figure 16. XRD spectra of ZrC nanoparticles, Ni-P and Ni-P-ZrC nanocomposite coatings and containing 0.75 g/L ZCNPs.

Figure 17 represent the XPS survey for NiP-0.75ZrC nanocomposite coating and the presence of ZCNPs in NiP-0.75ZrC nanocomposite coatings was confirmed from XPS analysis. It can be noticed the presence of the main peaks and the corresponding phases for the main elements, which correspond to Ni 2p, O 1s, C 1s, Zr 3d and P 2p. it worth mentioning that the presence of oxygen on the coating surface could be due to the incorporation with the other elements [75].

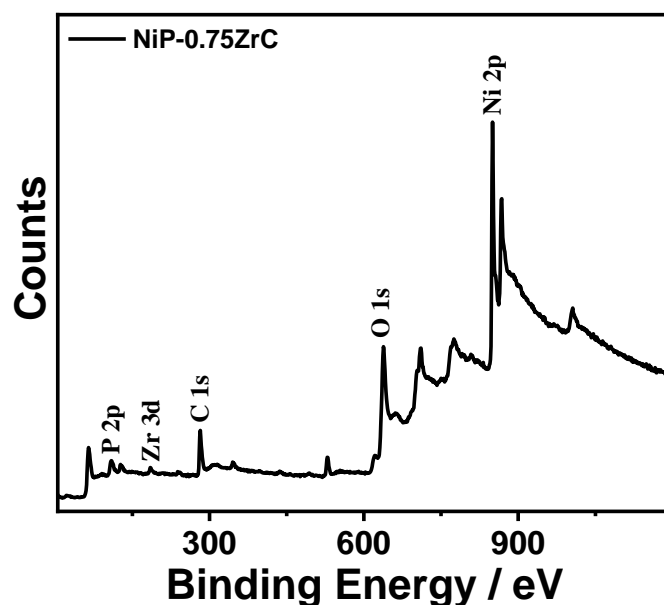


Figure 17. XPS survey spectrum for NiP-0.75ZrC nanocomposite coatings.

The fitted data of individual photoionization and their corresponding chemical states are presented in Figure. 18. High energy resolution spectra of Ni_{2p} (Figure. 18 (a)) region contains two distinct ionizations: Ni_{2p3/2} and Ni_{2p1/2} at 850.9 eV and 868.5 eV in the metallic state, whereas the peaks of Ni²⁺ at 852.3 eV, 856.6 eV, and 871.7 eV corresponds to the NiO and/or Ni(OH)₂ of Ni_{2p3/2} and Ni_{2p1/2}. However, a higher intensity peak for nickel proves the presence of metallic nickel. The formation of Ni(OH)₂ and NiO can be linked to the presence of hydroxyl ions from the aqueous electrolytic bath and other oxidation phenomena [28, 48]. Moreover, the peaks at 127.4 and 128.3 eV can be assigned to the elemental phosphorous (P) in the bulk of electrodeposited Ni-P-ZrC nanocomposite coatings, respectively (Figure.18 b). It can be noticed that the peak at 130.5 eV is due to; (i) the elemental phosphorus hypophosphite and/or (ii) the intermediate phosphorous ions (P(I) and/or P(III)) valence, which are presented in the inner portion of the protective film of the Ni-P coatings. However, peaks at 133.8eV can be due to the combination of oxides and/or hydroxides (P₂O₃ and/or P-OH) chemical states [28]. Figure. 18c shows the high-

resolution XPS spectra for Zr 3d. It has been reported that Zr 3d band is composed of Zr 3d_{5/2} and Zr 3d_{3/2}. The Zr 3d peak located at 180.4 and 183.1 clearly confirm the existence of the ZrC phase on the coating matrix [76, 77].

The XPS spectra for the C 1s show only C-C as a prominent peak at 284.6 eV, as seen in (Figure. 18d). It worth mentioning that the Zr-C bond is nominated at 282.5 eV despite the high intensity of the C-C bond, which diminishes the influence of the other bonds. Moreover, the peak at a binding energy of 284.3 and 285.2 is attributed to sp² and sp³ hybridization of carbon, respectively [78, 79].

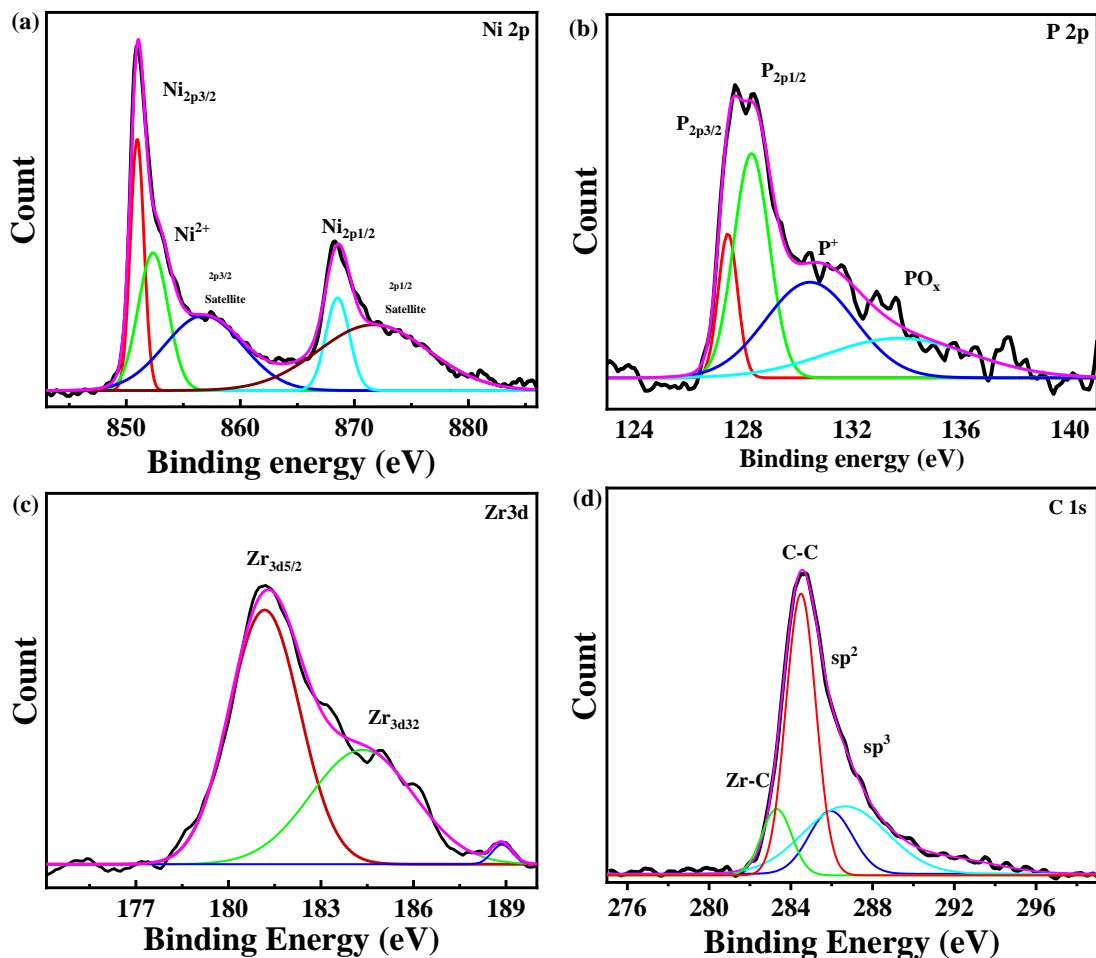


Figure 18. XPS spectra presenting the elemental composition of Ni-P-ZrC nanocomposite coatings, (a) Ni2p, (b) P2p and (c) Zr (d) metal carbide

3.2.2 Morphological Analysis

AFM and FESEM were used to explore morphological and topographical characteristics of the as-prepared metallic coatings. FE-SEM micrographs of Ni-P and Ni-P-ZrC coatings are depicted in Figure 19(c, d). As seen in the micrographs, Ni-P coatings Figure. 19(a, c)) have the plain type of structure, which modifies by the incorporation of ZCNPs. The growth of nodules is observed as a result of introducing ZCNPs in the chemical bath Figure. 19 (b, d). As for Ni-P coating, plain morphology is observed, which has changed to nodular by the addition of ZCNPs in the chemical bath. Nodular structure formation is visible at two distinct magnification for both Ni-P and Ni-P-ZrC nanocomposite coatings. This can be attributed to the increase in the number of sites for nucleation of Ni and P ions, which can be deposited on the substrate because of the large surface area of ZCNPs [24, 52, 80]. Moreover, the surface of as-prepared coatings is crack-free and pore-free, inferences the good quality of the developed Ni-P and Ni-P-ZrC nanocomposite coatings. The X-Section of Ni-P-ZrC nanocomposite coatings is presented in Figure. 19 (e). A smooth, uniform, adhered, and near to defect-free interface can be noticed between the coatings and the steel substrate. The coating thickness of $\sim 12.0 \mu\text{m}$ is achieved under the optimized experimental conditions.

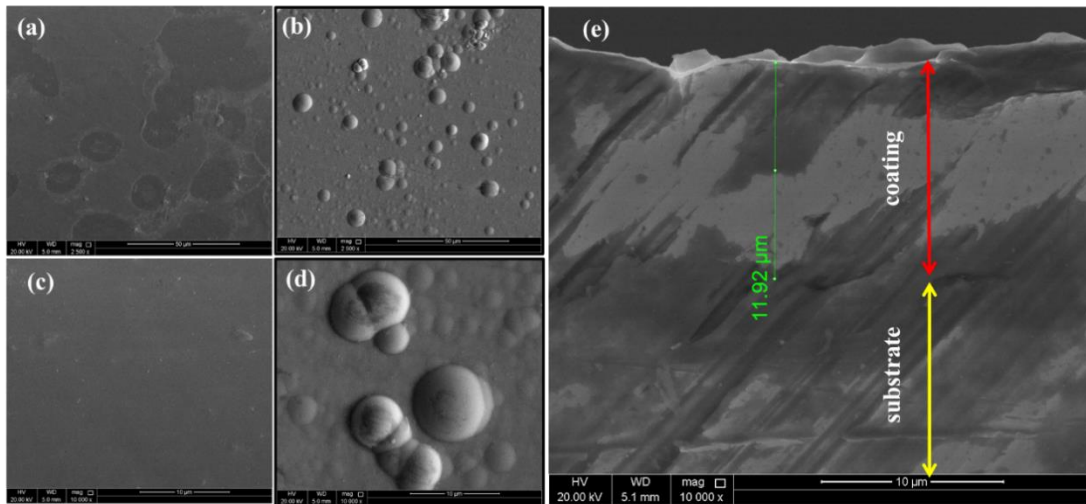


Figure 19. FE-SEM micrographs of developed coatings; Ni-P (a & c), Ni-P-ZrC nanocomposite coatings (b & d), at two different magnifications. A cross-sectional micrograph (e) of Ni-P- ZrC nanocomposite coatings.

The co-electrodeposited of ZCNPs in the Ni-P matrix was further evaluated using EDX analysis, see Figure. 6. The presence of Zirconium (Zr), carbon (C), phosphorus (P), and nickel (Ni) approve the ZCNPs incorporation into the Ni-P coating. The presence of carbon in excessive weight percentage can be accredited to integrate various effects such as the presence of carbon in the zirconium carbide compound, impurities related to the environment, and surface preparation for the microscopic analysis. For more clarity, the distribution of each element in Ni-P-ZrC nanocomposite coatings is also provided in Figure. 20 c, revealing the homogenous distribution of ZrC constituents in the Ni-P coating.

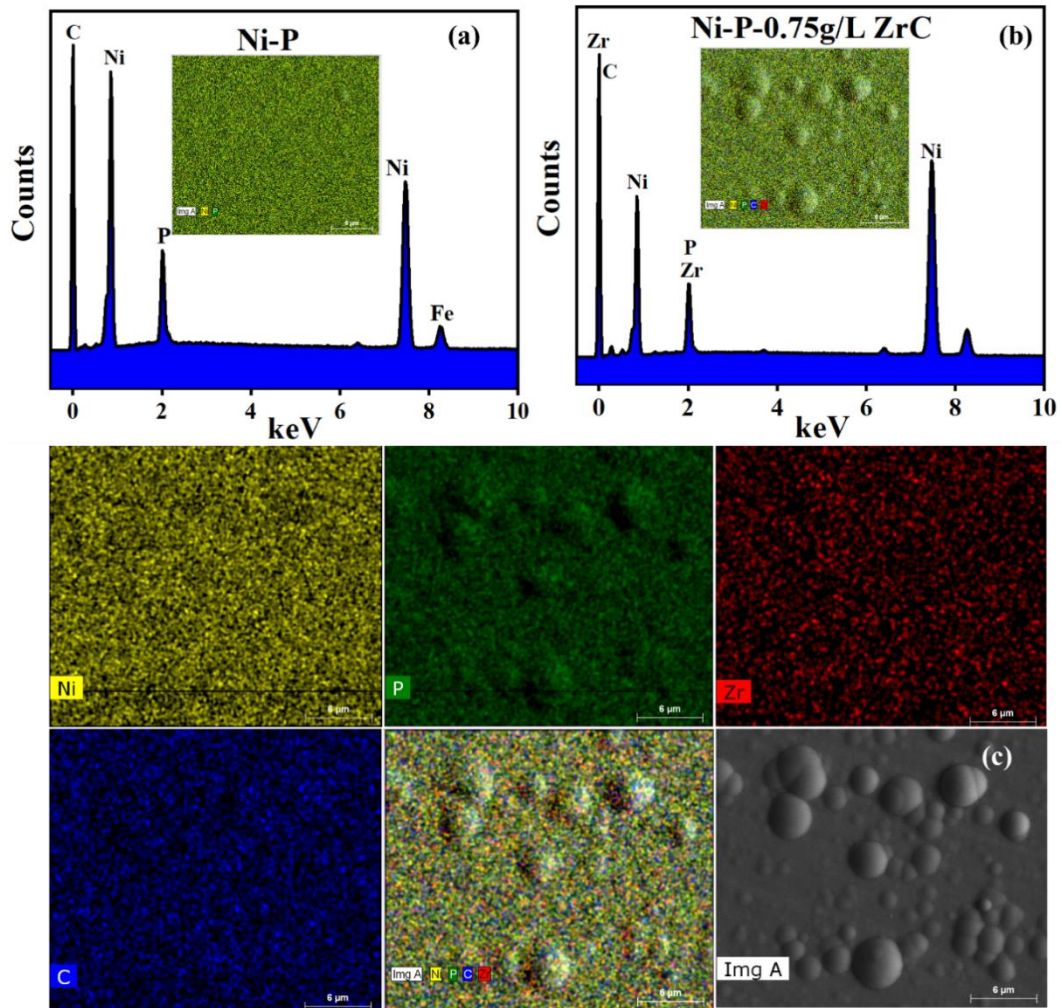


Figure 20. EDS elemental mapping of Ni-P (a), (b) Ni-P-ZrC nanocomposite coatings, and (c) detailed elemental mapping.

The composition of Ni-P and Ni-P-ZrC coatings, along with their cross-section, is provided in Table 7. The presence of nickel and phosphorus is evident in all the coatings in large percentages. However, a relatively high percentage of carbon can be attributed to the inference from the substrate and surrounding environmental carbon integrated along with the presence of carbon from ZCNPs [81]. The presence of iron in the cross-section is also observed, which is attributed to the carbon steel.

Table 6. EDS quantitative analysis of Ni-P and Ni-P-ZrC nanocomposite coatings.

Coating composition	Nickel	Phosphorus	Zirconium	Iron	Carbon
Ni-P	88.62%	11.38%	-	-	-
Ni-P- 0.75g/L ZrC	66.76%	8.18 %	1.69%	-	23.92%
Cross section Ni-P- 0.75g/L ZrC	26.92%	2.94%	0.64%	50.91%	18.59%

Many researchers have proposed the co-deposition process of several reinforcements within the Ni-P composite system. According to the Guglielmi model [53], particles first gently adsorb on the cathode surface through Van der Waals forces and then heavy adsorption and bonding by Coulomb forces. This model does not account for the size of the particle and hydrodynamics of the deposition. The correction factor to resolve for the magnetic stirring was proposed by Bercot et al. [54]. Bahadormanesh and Dolati improved the original model to account for the significant percentage of the second phase deposition [55]. Furthermore, Fransaer and co [56] developed a spherical particle trajectory model in which they listed out different forces on a spherical particle in a revolving disk electrode device. According to Celis et al. [57], the electrodeposition process of imparting ferrite reinforcement is said to involve five steps, including (i) creation of an ionic cloud around the reinforcement particles, ii) migration of reinforcement particles by induced convection towards the hydrodynamic layer of the

cathode, iii) diffusion of the particle by a double layer, iv) adsorption of the particle along with the ionic cloud at the cathode surface and v) reduction of the ionic cloud contributing to an irreversible entrapment of reinforcement particles in the metal matrix. According to the above discussion, the electrodeposition process requires the following steps: the passage of particles from the bulk electrolyte to the hydrodynamic boundary layer of the cathode. Particles in this layer are attributable to forced convection and electrophoresis. Particles movement at the cathode due to Van der Waal forces, and permanent incorporation of particles due to the reduction of ionic cloud around the hardened particle. This can be depicted as can be seen in Figure. 21.

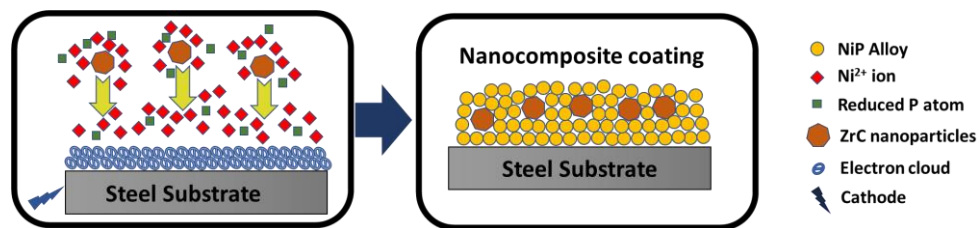


Figure 21. Schematic diagram for the co-deposition of ZrC nanoparticles at the cathode (substrate) to form Ni-P-ZrC composite coatings.

A comparison of the surface topography of Ni-P and Ni-P-ZrC nanocomposite coating is displayed in Figure. 22. The incorporation of ZCNPs has enhanced the grain growth and increased the surface roughness of the coatings which can be observed in the 3D AFM images, see Figure 22 (a, b). The corresponding roughness profiles of Ni-P and Ni-P-ZrC metallic coatings are also displayed for a clear comparison; see Figure. 22 (a, b). The Ra (average roughness) of the Ni-P coating is ~ 7.7 nm, which increases to 11.6 nm on the addition of 0.75 g/L of ZCNPs into the matrix, which can be essentially ascribed to the existence of insoluble and hard ceramic species into the Ni-P matrix. Moreover, R_q (RMS roughness) also increases from 10.4 nm to 15.4 nm for the metallic

coating compared to Ni-P coating, which is coherent with the average roughness. ZCNPs have boosted the surface roughness of Ni-P coatings [24, 28, 48].

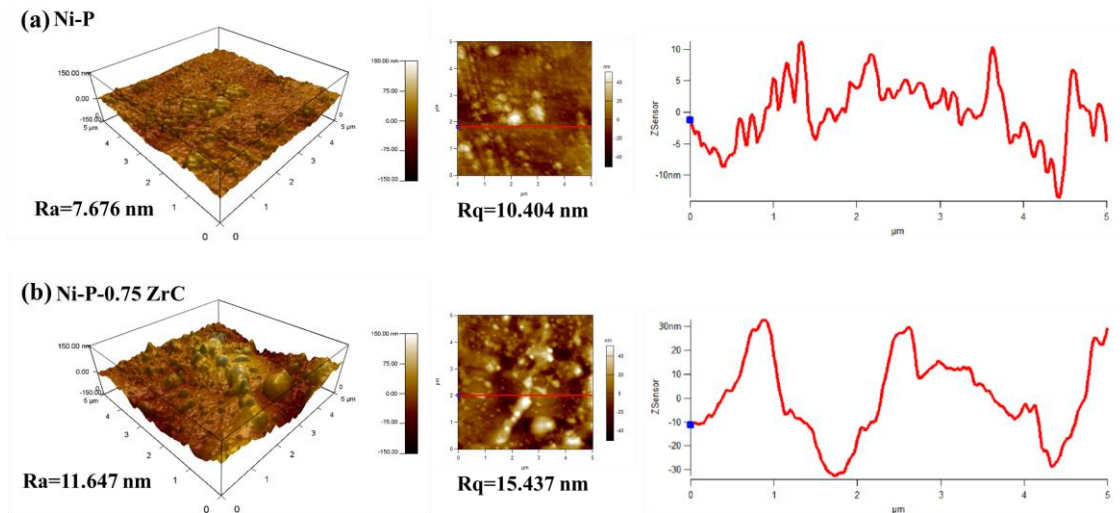


Figure 22. Three-dimensional AFM micrograph of as-prepared coatings along with their surface roughness profile; (a) Ni-P and (b), Ni-P-ZrC nanocomposite coatings.

3.2.3 Mechanical Properties

The mechanical properties of the prepared Ni-P and Ni-P-ZrC nanocomposite coatings were explored by Vickers microhardness testing and nanoindentation techniques. Microhardness outcomes for Ni-P and Ni-P-ZrC coatings are presented in Figure. 23a. It can be observed that the incorporation of ZCNPs has resulted in enhancing the coating hardness proving the classical concept of matrix and reinforcement to improve their individual properties. The Ni-P coatings demonstrate hardness of $\sim 520 \pm 10 \text{ HV}_{25}$, whereas hardness of Ni-P-ZrC nanocomposite coatings is enhanced to $\sim 580 \pm 15 \text{ HV}_{25}$ contributing an increase of $\sim 12\%$. This development in the hardness can be credited to the resistance to deformation offered by high strength ZCNPs by inhibiting the dislocation movement and restricting the plastic flow of the Ni-P matrix. It can be considered that a combination of dispersion hardening and construction of the

composite structure led to the improvement in microhardness [48, 82].

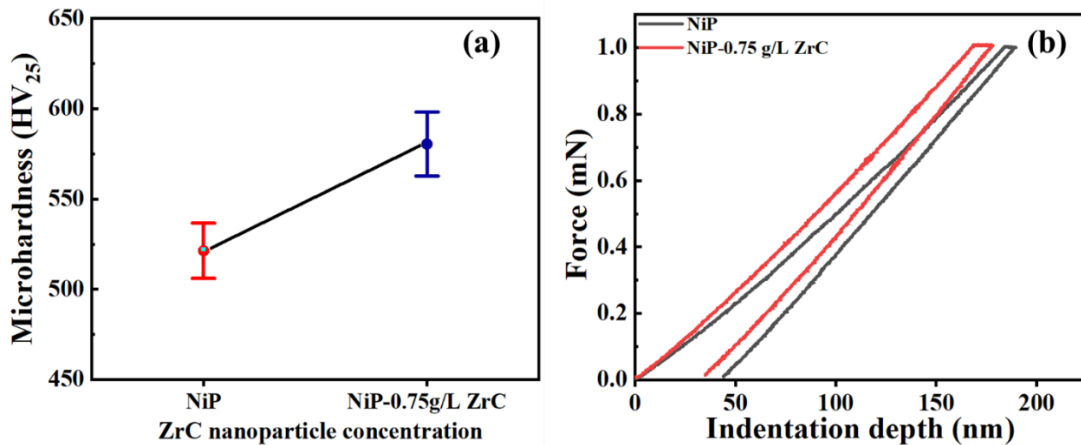


Figure 23. Mechanical properties of Ni-P and Ni-P-ZrC nanocomposite coatings; (a) Vickers microhardness and (b) Load indentation depth graph of Ni-P and Ni-P-0.75ZrC nanocomposite coatings.

Table 7. Derived parameters from load indentation profiles of Ni-P and Ni-P-ZrC nanocomposite coatings.

Composition	Elasticity (GPa)	Stiffness (kN/m)	Hardness (GPa)
Ni-P	14.05	7.49	4.98
Ni-P-ZrC	15.88	7.90	5.75

Mechanical properties of the as-plated coatings were further analyzed through the nanoindentation technique, and the outcomes are presented in Figure. 23b. It can be noted that the loading and unloading curve of Ni-P is a relatively larger area than that of Ni-P-ZrC metallic coatings. The indentation depth of Ni-P coating decreased from ~43.6 nm to ~33.1 nm by the incorporation of 0.75 g/L of ZCNPs, revealing an enhancement in the indentation resistance [23, 28, 48]. It is noteworthy that the deficiency of discontinuity in the nanoindentation plots indicates that the as-

electroplated nanocomposite coatings contain minimum defects (porosity, inhomogeneity, cracks, etc.).

The nanoindentation profiles were utilized for the quantitative investigation of the hardness of the as-electroplated coatings. For a clear comparison, various parameters resulting from load vs indentation depth profiles are also e in Table 8. The mechanical hardness of as-prepared metallic coatings was explored using the Oliver Pharr technique by applying the Berkovich diamond indenter tip under the maximum 1mN indentation force. The loading and unloading rate was adjusted at 200 $\mu\text{N/s}$, whereas the dwell time of 5 s was set at full load. The hardness of the Ni-P alloy improved from 4.98 GPa to 5.75 GPa upon the incorporation of 0.75 g L^{-1} of ZCNPs. The presence of ZrC nano species in the Ni-P matrix obstructs the movement of the dislocations leading to the development of the mechanical properties of the Ni-P-ZrC coating. Similarly, stiffness of Ni-P-0.75ZrC nanocomposite coating is observed to increase from 7.49 for Ni-P alloy to 7.90 kN/m, indicating an improvement in the deformation resistance was owing to the incidence of ZCNPs in the Ni-P matrix within the elastic limit. Moreover, the modulus of elasticity of Ni-P alloy is boosted from 14.1 GPa to 15.8 GPa by the incorporation of 0.75 ZCNPs [70].

Figure. 24 displays the coefficient of friction (COF) as a function of time for the electrodeposited Ni-P and Ni-P-0.75 ZrC coatings. The friction coefficient diminished from 0.34 for the electrodeposited Ni-P to 0.2 after the incorporation of 0.75 g/L of ZrC. The COF boosted at the initial stage of the friction time due to contact friction between the protruding part of the as-electroplated substrates and the stainless-steel ball. The COF of the metallic Ni-P metallic coating oscillated after 400 sec and significantly increased to a high value after 800 sec, which could be ascribed to the coating removed from the substrate resulting from damage (shear) of bonding between

the counter face asperities and metallic alloy. It is noteworthy that the presence of COF fluctuation could be divided into a vast and short domain. These fluctuations could be results from the removal and accumulation of the wear debris [23, 70, 82, 83]. On the other hand, in the case of Ni-P-ZrC, smooth and constant COF was observed after 200 sec of friction time, which is attributed to the lubrication influence of the nano species.

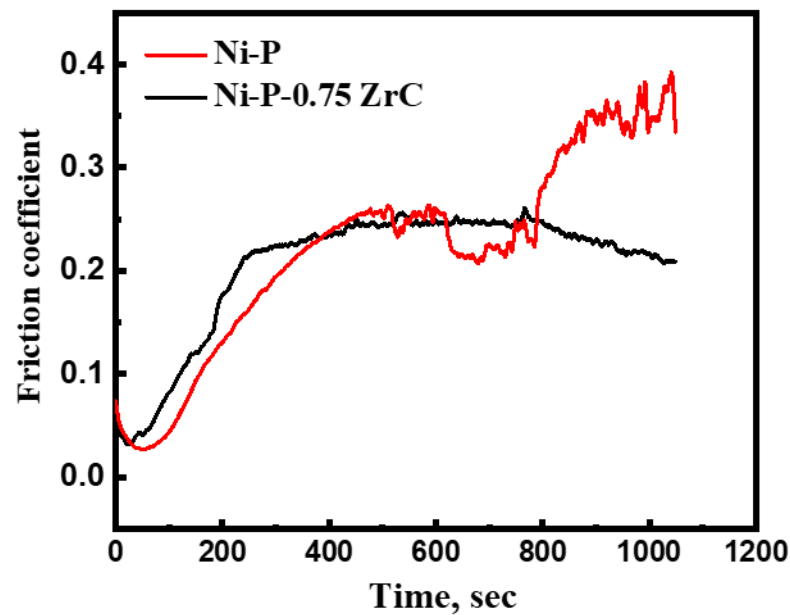


Figure 24. Wear test of the as-electrodeposited nanocomposite coatings before and after the addition of ZrC nanoparticles.

The wear rate (w_s) of the metallic Ni-P alloy before and after the incorporation of ZrC is calculated from the following equation [69].

$$w_s = \frac{w}{lL} \quad 3$$

where w is the weight loss (g), l is the sliding distance (m), and L is credited to the applied load (N). The wear rate (w_s) of Ni-P is lessened from $\sim 89 \mu \text{ gm N}^{-1} \text{ m}^{-1}$ to $38 \mu \text{ gm N}^{-1} \text{ m}^{-1}$ after the incorporation of ZrC nano species. Moreover, the wear track and depth of Ni-P alleviated from 456 and 8.1 μm to 295 and 4.4 μm as a result of the

incorporation of 0.75 g/L ZrC nanoparticles, Figure. 25 (c, d).

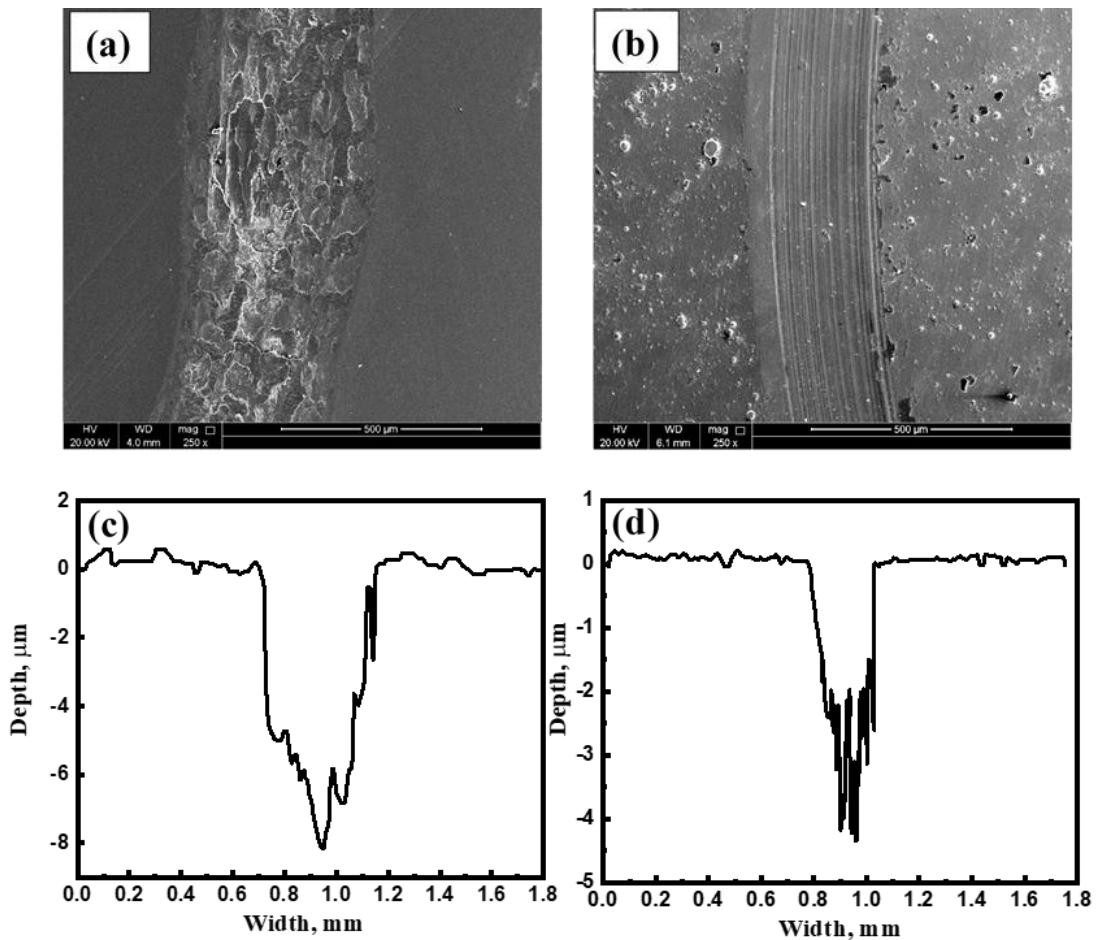


Figure 25. SEM of (a) Ni-P and (b) Ni-P-0.75 g/L ZrC after wear test and their corresponding wear depth profile (c, d), respectively.

Figure. 26 illustrates the SEM of the worn surface of the Ni-P metallic coatings at higher magnification. It can be observed the formation of fatigue microcracks in Ni-P metallic coating because of inherent properties, such as low hardness, ductility, an apparent poor adhesion, and internal stress in the coating matrix. The presence of grooves or cavities could be credited to the surface removed oxide layers or tribolayers, contributing to slipping wear by lying among the worn metallic coating and abrasive as a third body [69]. Accordingly, the wear regime in Ni-P alloy is adhesive. Figure. 26b.

shows characteristic plowing furrows without any visible microcracks, which is accredited to the higher hardness value of the nanocomposite coating. The incorporation of ZrC nanoparticles into NiP exhibits linear wear tracks, indicating an abrasive wear approach [84].

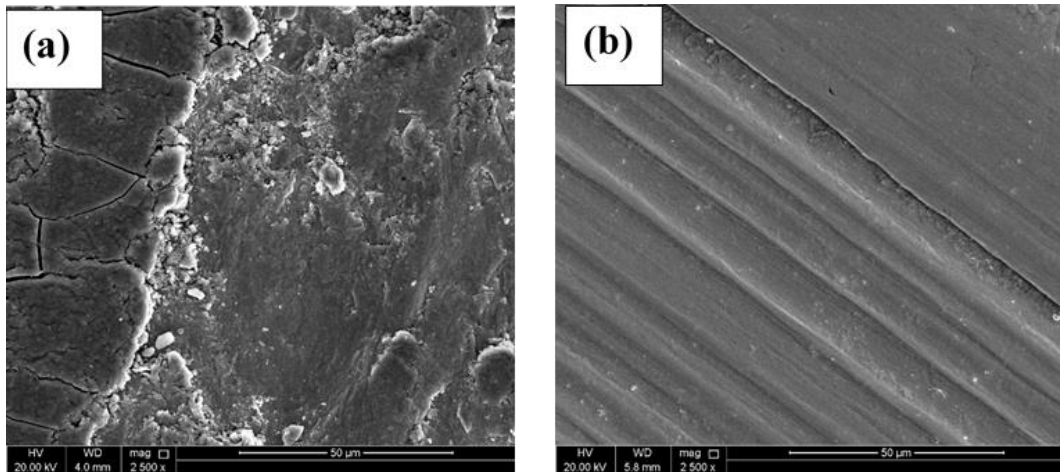


Figure 26. High magnification SEM of the worn scar of (a) Ni-P and (b) Ni-P/0.75ZrC nanocomposite coating.

Figure 27a represents the maximum measured depth versus particles speed-dependent at the same exposure time. It can be noticed that the depth is proportional to the particles' velocity, indicating higher coating loss at a higher speed. Moreover, the maximum erosion depth is lessened from 16.3 to 13.5 μm with amending 0.75 ZrC to the coating matrix at 101 m s^{-1} . In the meantime, Figure 27b depict the volume loss of NiP and NiP-0.75ZrC nanocomposite coatings at different speed of the erodent particles. The volume loss rate is derived from the average erosion depth and the measured eroded area per exposure time. As expected, the NiP-0.75ZrC nanocomposite coatings have better erosion resistance comparing with the Ni-P coating. Moreover, the volume loss rate at 19 m s^{-1} diminished from 1.23 to $0.38 \mu\text{m}^3\text{s}^{-1}$ for Ni-P and NiP-0.75ZrC nanocomposite coating, respectively, indicating that the damage of the NiP-

0.75ZrC coating is three times lower than bare coating at low erodent speed. Meanwhile, the volume loss rate at 101 m s^{-1} of the erodent particles reduced from 3.7 to $2.9 \text{ } \mu\text{m}^3 \text{ s}^{-1}$ for NiP and NiP-0.75ZrC coatings, respectively.

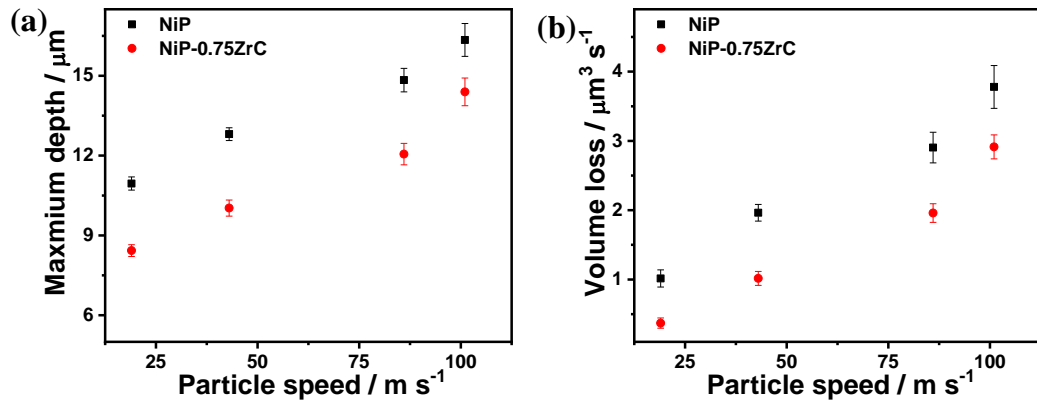


Figure 27. a) Maximum erodent depth and volume loss for the Ni-P and Ni-P-0.75ZrC nanocomposite coatings at different particles velocity after 30 s of erosion time.

Figure. 28 depicts the optical profilometry of the eroded substrates of the NiP and NiP-0.75ZrC nanocomposite coatings after 30 s of erosion time at 101 m s^{-1} . It can be noticed that the surface roughness for Ni-P coating is lower than the as-synthesized NiP-0.75ZrC metallic coating after erosion test, as seen in Figure. 28 (a, b). Additionally, the penetration depth of Ni-P alloy is higher than that of NiP-0.75ZrC nanocomposite coating, as demonstrated in Figure. 28 (c, d).

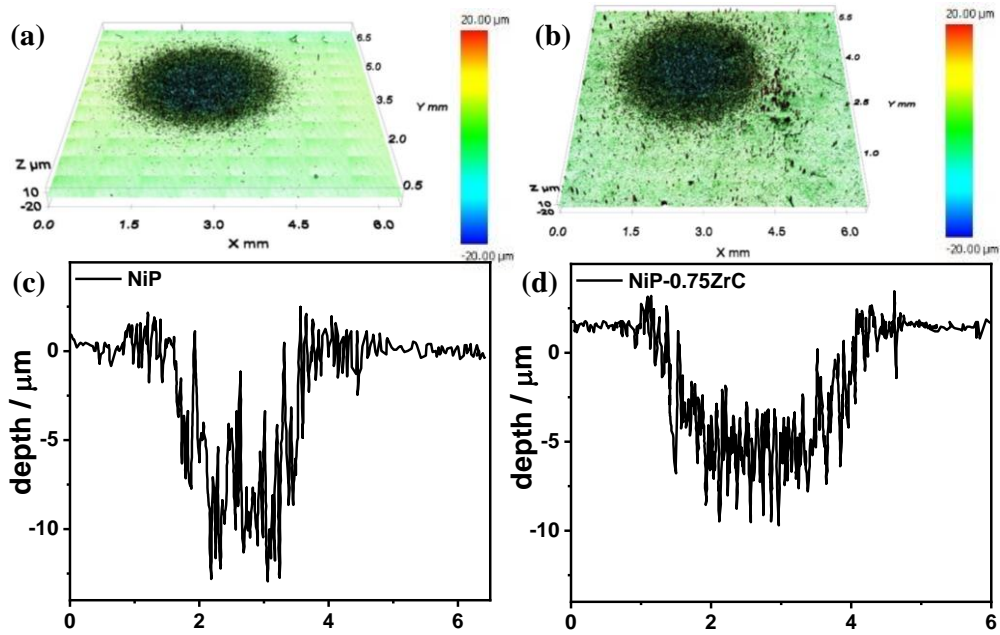


Figure 28. Surface topography of a) Ni-P and b) Ni-P-0.75ZrC after 30 s of erosion time at 101 m/s of particle velocity.

3.2.4 Corrosion Assessment

EIS is a widely accepted method to study the corrosion resistance of the as-fabricated coatings. EIS plots of the carbon steel, Ni-P, and Ni-P-0.75 ZrC nanocomposite coatings are shown in Figure. 29. Experimental data for the substrate were fitted using the modified version of the Randle cell in which pure capacitor was improvised with constant phase element to account for the pure capacitance as shown in Figure 30a. For explaining the corrosion behavior of Ni-P and Ni-P-ZrC nanocomposite coating, their experimental data were fitted using a two-time constant cascaded electrical equivalent circuit as shown in Figure. 30b. The electric circuits consist of R_s for the resistance of the brine solution used for the test, whereas R_{po} and R_{ct} account for the pore resistance and charge transfer resistance of the coat. Constant phase element (CPE_1 And CPE_2) were utilized instead of a pure capacitor to account for the discrepancy at the surface

and interface of the metallic coating computed from the following equation [48]:

$$\frac{1}{Z_{CPE}} = Q(j\omega)^n \quad 4$$

In which Q stands for admittance, ω is the angular frequency, and n is the exponent for the constant phase element, which is responsible for the nature of capacitance such that closer to unity means pure capacitor.

Bode plot of pure carbon steel substrate and nanocomposite coating is presented in Figure 29. It can be perceived that the corrosion resistance of the carbon steel sample is relatively low ($260 \Omega \text{ cm}^2$). Ni-P coatings possess more corrosion resistance than carbon steel as the impedance value of Ni-P coating is $1782.8 \Omega \text{ cm}^2$, which can be ascribed to the construction of a protective film of hypophosphite as a result of the electrochemical reaction of salt solution with the Ni-P coating [24, 68]. The incorporation of secondary phase ZrC nano species in the Ni-P alloy further changed the impedance response, leading to the broadening of the phase angle plot. It indicates a more protective composite coating (shift towards higher frequencies) and, on the other hand, the presence of other processes (decreased corrosion activity) [28, 69, 82]. The enhancement in the impedance of composite coatings can be attributed to reducing the active corrosion sites due to the trapping of inert and corrosion-resistant ZrC nanoparticles. Interestingly, the incorporation of 0.75 g/L of ZrC nanoparticles increased the R_{ct} value to $8353 \Omega \text{ cm}^2$, which is four times higher than that of Ni-P alloy.

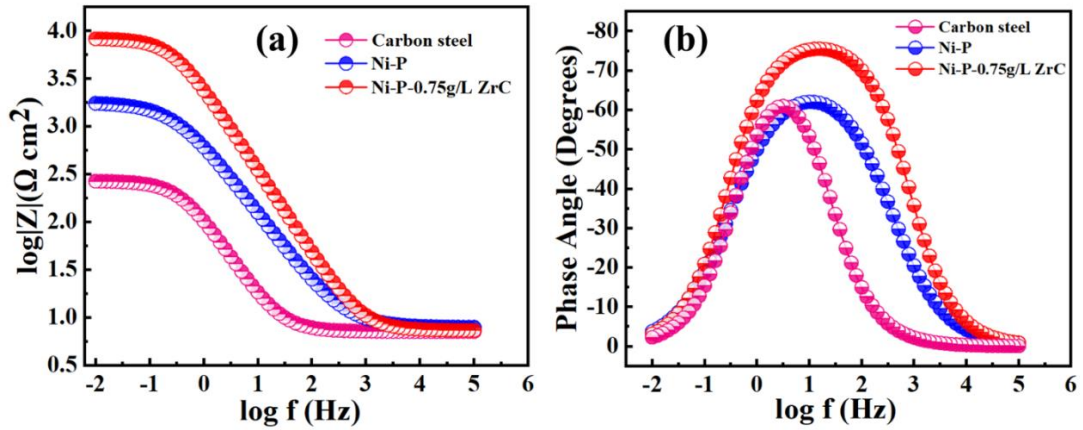


Figure 29. (a) Bode plot of the substrate, Ni-P, and Ni-P-0.75g/L-ZrC nanocomposite coatings containing frequency impedance magnitude curve and (b) frequency phase angle curve after 2 hours of immersion in 3.5 wt.% NaCl solution

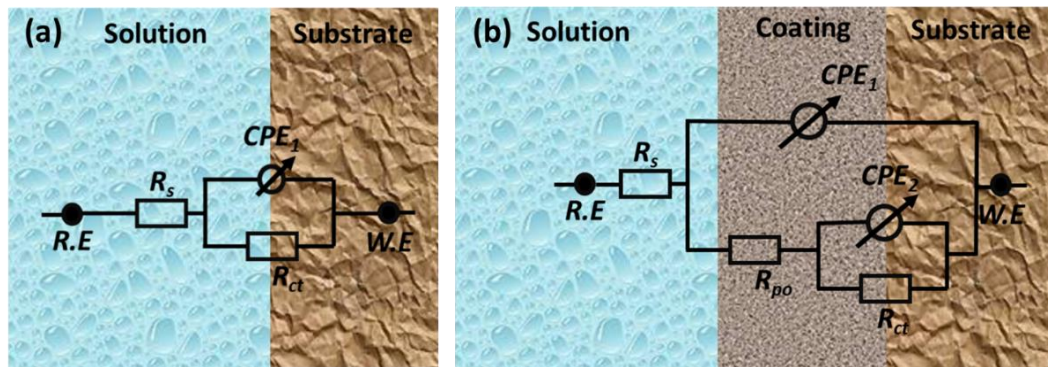


Figure 30. The equivalent electric circuit used for fitting the experimental EIS data for (a) polished carbon steel, (b) Ni-P and Ni-P-0.75ZrC nanocomposite coatings.

Figure.31 a show the Nyquist plots for carbon steel substrate, Ni-P, and Ni-P-0.75ZrC metallic coatings. The experimental data were fitted using the two-time constant equivalent circuit as exhibited in Figure.30 b. The semicircular radius of the Nyquist curve reveals a successive increase, pointing to high corrosion impedance resulting from incorporating ZrC nanoparticles. The incorporation of ZrC nano species in the Ni-P alloy increased the polarization and pore resistance of the as-fabricated coatings, see Figure. 31 b. Enhancement in the corrosion resistance of the Ni-P alloy as a result of

reinforcing the inert ZrC nano-species that fill the defects existing in Ni-P matrices such as pores and micro-cracks, leading to burden the entrance of the hydrated Cl^- species to reach the carbon steel surface [28, 48, 69].

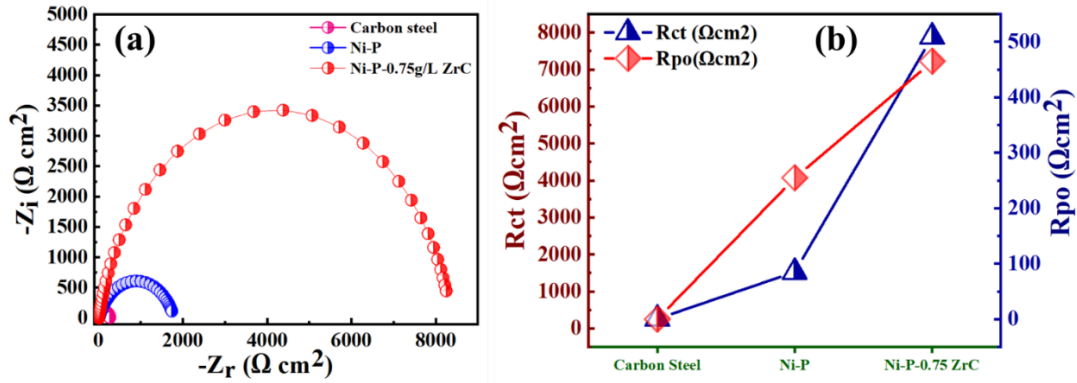


Figure 31. (a) Nyquist plot for carbon steel and the as-fabricated metallic coatings Ni-P and Ni-P-0.75g/L ZrC in 3.5 wt% NaCl solution (b) variation of R_{po} and R_{ct} on carbon steel substrate, Ni-P coatings, and Ni-P-0.75g/LZrC nanocomposite coating.

The corrosion resistance of carbon steel substrate, Ni-P, and Ni-P-ZrC nanocomposite coatings containing various concentrations of ZrC particles was also studied by Tafel polarization employing a scan rate of 1 mV s^{-1} as revealed in Figure. 32. Electrochemical factors such as corrosion current density (I_{corr}), corrosion potential (E_{corr}), anodic Tafel slope (β_a), and cathodic Tafel slope (β_c) were extrapolated from the fitted curve and presented in Table 9. Moreover, corrosion protection efficiency (PE %) was estimated from the following formulation [69] :

$$PE\% = 1 - \frac{i_2}{i_1} \quad 5$$

where i_1 is the current density of the Ni-P coatings and i_2 is the current density of coated samples.

Carbon steel is observed to have the highest current density of $56.9 \mu\text{A cm}^{-2}$ with an

electrode potential of 658 mV. However, the maximum value of current density for Ni-P coating is observed to be $16.5 \mu\text{A cm}^{-2}$ at a potential of 486 mV, showing development in the corrosion resistance of 71.03%. On the other hand, the incorporation of 0.75 g/L of ZrC nanoparticles considerably alleviated the i_{corr} to $8.3 \mu\text{A cm}^{-2}$ with almost 85.4% development in the corrosion resistance. The improvement can be associated with the incorporation of ZrC nanoparticles in the Ni-P coating matrix, has enhanced the corrosion mitigation after the addition of the ZrC nanoparticles by reducing the number of active positions for the adsorption of chloride ion on the surface defects of coatings such as cracks and pores [72, 85].

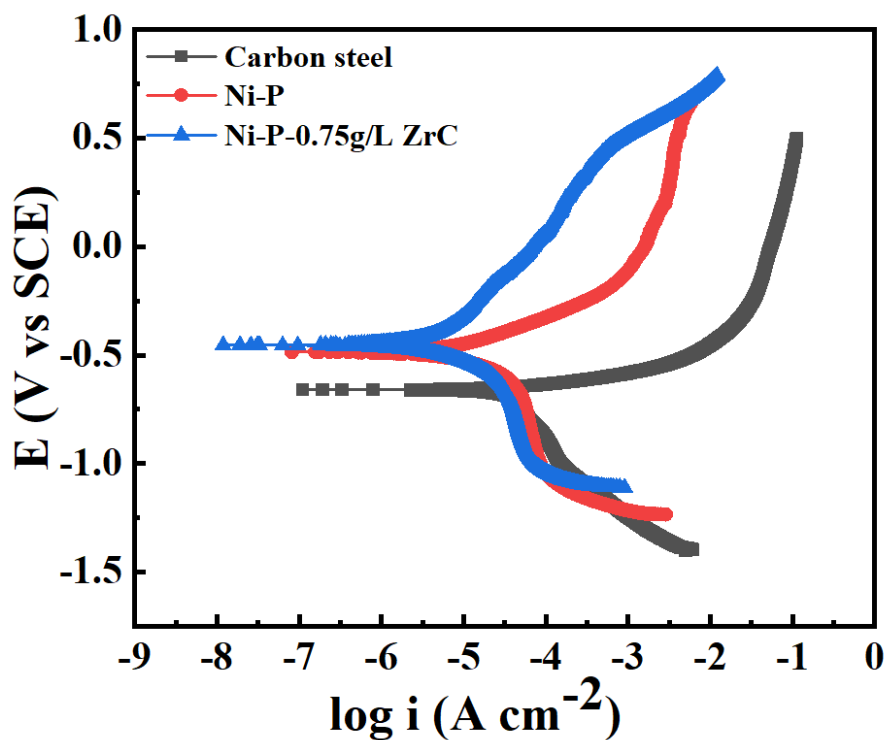


Figure 32. Tafel profiles of the steel sample, Ni-P and Ni-P-0.75ZrC nanocomposite coating.

Table 8. Electrochemical parameters derived from the Tafel plots of carbon steel, Ni-P, and Ni-P-0.75g/L ZrC nanocomposite coating.

Composition	β_a (V/decade)	β_c (V/decade)	$i_{corr}(\mu A\ cm^{-2})$	E_{corr} (mV)	PE%
Carbon steel	0.3148	0.4882	56.86	-658	-
Ni-P	0.1747	0.3237	16.47	-486	71 %
Ni-P 0.75g/L ZrC	0.4484	0.2756	8.30	-454	85 %

CHAPTER 4: CONCLUSION AND FUTURE RECOMMENDATION

4.1 Conclusions

Properties and performance of Ni-P coating were successfully modified by incorporating nanoparticles to obtain Ni-P-X (X=TiC, ZrC) nanocomposite coatings synthesized through the electrodeposition process. The effect of increased concentration and nature of reinforcement was thoroughly investigated through the state-of-the-art facilities. The concentration of reinforcing nanoparticles in the Ni-P matrix significantly influences the composition, morphological, structural, mechanical, wear, and corrosion protection properties of the developed nanocomposite coatings.

The salient conclusions from the current thesis can be enumerated as follows:

- Incorporating TiC and ZrC nanoparticles modifies the morphology of pure Ni-P coatings from fibrous to well-defined nodular geometry due to the heterogeneous nucleation sites provided by nanoparticles without altering their parent structure. The increase in concentration improves the nodular structure in both cases.
- All the compositions present a semi-amorphous structure and the presence of nanoparticles observed in XPS spectra and EDS results.
- Introducing nanoparticles (TiC, ZrC) into the Ni-P matrix leads to alter its mechanical properties.
- The best mechanical properties are achieved in Ni-P-TiC nanocomposite coatings at 1.5g/L of TiC providing 19% improvement in microhardness, whereas, in Ni-P-ZrC nanocomposite coatings, the concentration of 0.75g/L of ZrC is traced out to be optimum demonstrating 15% improvement in the microhardness of the prepared coatings.
- The enhancement in the mechanical properties can be attributed to the dispersion

hardening effect.

- Electrochemical Impedance Spectroscopy (EIS) analysis reveals that corrosion resistance of Ni-P coatings increases with the introduction and increment of nanoparticles. Moreover, 2.0 g/L of TiC ($26 \text{ k } \Omega \text{ cm}^2$) has shown more than three times of improvement than 0.75 g/L ZrC ($7.5 \text{ k}\Omega \text{ cm}^2$) in terms of total impedance and corrosion resistance.
- The type and concentration of reinforcement have a significant influence in modifying the mechanical and corrosion resistance properties of Ni-P coatings.
- As a comparison, Ni-P-TiC nanocomposite coatings at the concentration of 2.0 g/L of TiC demonstrate better corrosion resistance when compared with all other compositions of TiC and ZrC studied in the current study.

4.2 Future Recommendation

Extensive experimental research in the Ni-P matrix is to be carried out as compared to its counterparts, namely Ni-W, Ni-Co and pure Ni coatings. There needs to be a standardized procedure of characterization and reporting of microhardness and corrosion results to make it easier for comparison of results from different researchers around the globe. Small scale college projects must be collaborated to advertise the technology and attract industries. Parametric study for the optimized bath composition and its effect on the current density is to be investigated in future work to study the deposition as well as corrosion mechanism. Literature on the second phase particle in NiP coatings is still needed research with most of the famous ceramics for breakthrough in the field. Hybrid second phase nanocomposite is not investigated by the research community, which could open the door for the amazing improvement in the properties. Parametric study concerning the particle size from sub-micron size to nano

size can be studied, and the shift in the properties can be understood and harnessed for future research. Modelling and data mining of the present experimental data should be carried out to predict the lifetime of the coating. Heat treatment of the composite coatings is another attractive area of investigation in enhancing the properties of coatings. Finally, it is recommended to perform simulation and modelling of the mechanical and corrosion behavior of Ni-P-X (X=TiC, ZrC) nanocomposite coatings.

REFERENCES

1. Zamani, S.M., S.A. Hassanzadeh-Tabrizi, and H. Sharifi, *Failure analysis of drill pipe: A review*. Engineering Failure Analysis, 2016. **59**: p. 605-623.
2. Xie, M. and Z. Tian, *A review on pipeline integrity management utilizing in-line inspection data*. Engineering Failure Analysis, 2018. **92**: p. 222-239.
3. Amaya-Gómez, R., et al., *Reliability assessments of corroded pipelines based on internal pressure – A review*. Engineering Failure Analysis, 2019. **98**: p. 190-214.
4. Bhandari, J., et al., *Modelling of pitting corrosion in marine and offshore steel structures – A technical review*. Journal of Loss Prevention in the Process Industries, 2015. **37**: p. 39-62.
5. Ossai, C.I., B. Boswell, and I.J. Davies, *Pipeline failures in corrosive environments – A conceptual analysis of trends and effects*. Engineering Failure Analysis, 2015. **53**: p. 36-58.
6. Finšgar, M. and J. Jackson, *Application of corrosion inhibitors for steels in acidic media for the oil and gas industry: A review*. Corrosion Science, 2014. **86**: p. 17-41.
7. Shekari, E., F. Khan, and S. Ahmed, *Economic risk analysis of pitting corrosion in process facilities*. International Journal of Pressure Vessels and Piping, 2017. **157**: p. 51-62.
8. Wulf, S.-E., et al., *Electrochemical techniques as innovative tools for fabricating divertor and blanket components in fusion technology*. Fusion Engineering and Design, 2019.
9. Wasekar, N.P., et al., *Influence of mode of electrodeposition, current density and saccharin on the microstructure and hardness of electrodeposited*

- nanocrystalline nickel coatings*. Surface and Coatings Technology, 2016. **291**: p. 130-140.
10. Zhang, S., et al., *Recent advances of superhard nanocomposite coatings: a review*. Surface and Coatings Technology, 2003. **167**(2-3): p. 113-119.
 11. Qu, N.S., et al., *Pulse electrodeposition of nanocrystalline nickel using ultra narrow pulse width and high peak current density*. Surface and Coatings Technology, 2003. **168**(2): p. 123-128.
 12. Chen, L., et al., *Influence of pulse frequency on the microstructure and wear resistance of electrodeposited Ni–Al₂O₃ composite coatings*. Surface and Coatings Technology, 2006. **201**(3-4): p. 599-605.
 13. Borkar, T. and S.P. Harimkar, *Effect of electrodeposition conditions and reinforcement content on microstructure and tribological properties of nickel composite coatings*. Surface and Coatings Technology, 2011. **205**(17-18): p. 4124-4134.
 14. Qu, N.S., D. Zhu, and K.C. Chan, *Fabrication of Ni–CeO₂ nanocomposite by electrodeposition*. Scripta Materialia, 2006. **54**(7): p. 1421-1425.
 15. Xue, Y.-J., et al., *Effect of different electrodeposition methods on oxidation resistance of Ni–CeO₂ nanocomposite coating*. Surface and Coatings Technology, 2010. **204**(21-22): p. 3539-3545.
 16. Kartal, M., et al., *Production of pulse electrodeposited Ni–TiC nanocomposite coatings*. Materials Today: Proceedings, 2017. **4**(7): p. 6982-6989.
 17. Walsh, F.C., C.T.J. Low, and J.O. Bello, *Influence of surfactants on electrodeposition of a Ni-nanoparticulate SiC composite coating*. Transactions of the IMF, 2015. **93**(3): p. 147-156.

18. Wang, W., et al., *Fabrication and characterization of Ni–ZrO₂ composite nano-coatings by pulse electrodeposition*. Scripta Materialia, 2005. **53**(5): p. 613-618.
19. Sknar, Y.E., O.O. Savchuk, and I.V. Sknar, *Characteristics of electrodeposition of Ni and Ni-P alloys from methanesulfonate electrolytes*. Applied Surface Science, 2017. **423**: p. 340-348.
20. Nava, D., et al., *Effects of Heat Treatment on the Tribological and Corrosion Properties of Electrodeposited Ni-P Alloys*. Vol. 8. 2013. 2670-2681.
21. Sadeghi, A., *Microstructure evolution and strengthening mechanism in Ni-based composite coatings*. 2016.
22. Fayyad, E.M., et al., *Effect of electroless bath composition on the mechanical, chemical, and electrochemical properties of new NiP–C₃N₄ nanocomposite coatings*. Surface and Coatings Technology, 2019. **362**: p. 239-251.
23. Fayyad, E.M., et al., *Novel electroless deposited corrosion — resistant and anti-bacterial NiP–TiNi nanocomposite coatings*. Surface and Coatings Technology, 2019. **369**: p. 323-333.
24. Luo, H., et al., *Synthesis of a duplex Ni-P-YSZ/Ni-P nanocomposite coating and investigation of its performance*. Surface and Coatings Technology, 2017. **311**: p. 70-79.
25. Rana, A.R.K. and Z. Farhat, *Preparation and tribological characterization of graphene incorporated electroless Ni-P composite coatings*. Surface and Coatings Technology, 2019. **369**: p. 334-346.
26. Saravanan, I., et al., *Wear behaviour of electroless Ni-P and Ni-P-TiO₂ composite coatings on En8 steel*. Materials Today: Proceedings, 2020.

27. Zou, T.Z., et al., *Friction and wear properties of electroless Ni-P- (IF-MoS₂) composite coatings in humid air and vacuum*. Materials Science and Engineering: A, 2006. **426**(1): p. 162-168.
28. Bahgat Radwan, A., et al., *Properties enhancement of Ni-P electrodeposited coatings by the incorporation of nanoscale Y₂O₃ particles*. Applied Surface Science, 2018. **457**: p. 956-967.
29. He, Y., et al., *An electrodeposited Ni-P-WS₂ coating with combined super-hydrophobicity and self-lubricating properties*. Electrochimica Acta, 2017. **245**: p. 872-882.
30. Hou, K.-H., et al., *Ni-P-SiC composite produced by pulse and direct current plating*. Materials Chemistry and Physics, 2006. **100**(1): p. 54-59.
31. Yuan, X.-t., et al., *Effect of nano-SiC particles on the corrosion resistance of NiP-SiC composite coatings*. International Journal of Minerals, Metallurgy and Materials, 2009. **16**(4): p. 444-451.
32. Zoikis-Karathanasis, A., E.A. Pavlatou, and N. Spyrellis, *Pulse electrodeposition of Ni-P matrix composite coatings reinforced by SiC particles*. Journal of Alloys and Compounds, 2010. **494**(1): p. 396-403.
33. Sheu, H.-H., et al., *Effects of plating parameters on the Ni-P-Al₂O₃ composite coatings prepared by pulse and direct current plating*. Surface and Coatings Technology, 2013. **235**: p. 529-535.
34. Lelevic, A. and F.C. Walsh, *Electrodeposition of NiP alloy coatings: A review*. Surface and Coatings Technology, 2019. **369**: p. 198-220.
35. Elias, L., B. Bhat, and A. Hegde, *Development of nanolaminated multilayer Ni-P alloy coatings for better corrosion protection*. Vol. 6. 2016.

36. Dhanapal, K., V. Narayanan, and A. Stephen, *Effect of phosphorus on magnetic property of Ni–P alloy synthesized using pulsed electrodeposition*. *Materials Chemistry and Physics*, 2015. **166**: p. 153-159.
37. Hansal, W.E.G., et al., *Pulse-electrodeposited NiP–SiC composite coatings*. *Electrochimica Acta*, 2013. **114**: p. 851-858.
38. Hou, K.-H., M.-C. Jeng, and M.-D. Ger, *The heat treatment effects on the structure and wear behavior of pulse electroforming Ni–P alloy coatings*. *Journal of Alloys and Compounds*, 2007. **437**(1-2): p. 289-297.
39. Zoikis-Karathanasis, A., E.A. Pavlatou, and N. Spyrellis, *The effect of heat treatment on the structure and hardness of pulse electrodeposited NiP–WC composite coatings*. *Electrochimica Acta*, 2009. **54**(9): p. 2563-2570.
40. *Standard Test Method for Conducting Erosion Tests by Solid Particle Impingement Using Gas Jets*.
41. C. Okonkwo, P., et al., *Erosion Behavior of API X120 Steel: Effect of Particle Speed and Impact Angle*. *Coatings*, 2018. **8**(10): p. 343.
42. Yang, Y., et al., *Fabrication and characterization of electroless Ni–P–ZrO₂ nano-composite coatings*. *Applied Nanoscience*, 2011. **1**(1): p. 19-26.
43. Knyazev, A.V., et al., *Magnetic properties of electrodeposited amorphous nickel–phosphorus alloys*. *Russian Journal of Electrochemistry*, 2017. **53**(3): p. 270-274.
44. Shakoor, R., et al., *Synthesis, characterization and applications of electroless Ni–B coatings-A review*. 2016. **11**: p. 2486-2512.
45. Afroukhteh, S., C. Dehghanian, and M. Emamy, *Preparation of electroless Ni–P composite coatings containing nano-scattered alumina in presence of*

- polymeric surfactant*. Progress in Natural Science: Materials International, 2012. **22**: p. 318–325.
46. Li, B. and W. Zhang, *Microstructural, surface and electrochemical properties of pulse electrodeposited Ni–W/Si₃N₄ nanocomposite coating*. Ceramics International, 2018. **44**(16): p. 19907-19918.
 47. Safavi, M.S. and A. Rasooli, *Ni-P-TiO₂ nanocomposite coatings with uniformly dispersed Ni₃Ti intermetallics: Effects of current density and post heat treatment*. Surface and Coatings Technology, 2019. **372**: p. 252-259.
 48. Sliem, M.H., et al., *Enhanced mechanical and corrosion protection properties of pulse electrodeposited NiP-ZrO₂ nanocomposite coatings*. Surface and Coatings Technology, 2020. **403**: p. 126340.
 49. Restrepo Parra, E., P.J. Arango, and V. Benavides, *XPS structure analysis of TiN/TiC bilayers produced by pulsed vacuum arc discharge*. Dyna, 2010. **77**.
 50. Spanou, S., et al., *Self cleaning behaviour of Ni/nano-TiO₂ metal matrix composites*. Electrochimica Acta, 2013. **105**: p. 324-332.
 51. Pillai, A.M., A. Rajendra, and A.K. Sharma, *Electrodeposited nickel–phosphorous (Ni–P) alloy coating: an in-depth study of its preparation, properties, and structural transitions*. Journal of Coatings Technology and Research, 2012. **9**(6): p. 785-797.
 52. Ping, Z., et al., *Mechanically assisted electroplating of Ni–P coatings on carbon steel*. Surface and Coatings Technology, 2008. **202**(24): p. 6023-6028.
 53. Guglielmi, N., *Kinetics of the Deposition of Inert Particles from Electrolytic Baths*. Journal of The Electrochemical Society, 1972. **119**(8): p. 1009.

54. Berçot, P., E. Peña-Muñoz, and J. Pagetti, *Electrolytic composite Ni-PTFE coatings: an adaptation of Guglielmi's model for the phenomena of incorporation*. Surface and Coatings Technology, 2002. **157**(2): p. 282-289.
55. Bahadormanesh, B. and A. Dolati, *The kinetics of Ni-Co/SiC composite coatings electrodeposition*. Journal of Alloys and Compounds, 2010. **504**(2): p. 514-518.
56. Fransaer, J., J.P. Celis, and J.R. Roos, *Analysis of the Electrolytic Codeposition of Non-Brownian Particles with Metals*. Journal of The Electrochemical Society, 1992. **139**(2): p. 413-425.
57. Celis, J.P., J.R. Roos, and C. Buelens, *A Mathematical Model for the Electrolytic Codeposition of Particles with a Metallic Matrix*. Journal of The Electrochemical Society, 1987. **134**(6): p. 1402-1408.
58. Huang, H.-C., et al., *Microstructure evolution and hardening mechanisms of Ni-P electrodeposits*. Surface and Coatings Technology, 2010. **205**(7): p. 2097-2103.
59. Balaraju, J.N., T.S.N.S. Narayanan, and S.K. Seshadri, *Structure and phase transformation behaviour of electroless Ni-P composite coatings*. Materials Research Bulletin, 2006. **41**(4): p. 847-860.
60. Grove, D.E., U. Gupta, and A.W. Castleman, *Effect of Carbon Concentration on Changing the Morphology of Titanium Carbide Nanoparticles from Cubic to Cuboctahedron*. ACS Nano, 2010. **4**(1): p. 49-54.
61. Zhou, Y.-r., et al., *Electrodeposition and corrosion resistance of Ni-P-TiN composite coating on AZ91D magnesium alloy*. Transactions of Nonferrous Metals Society of China, 2016. **26**(11): p. 2976-2987.

62. Wang, Y., et al., *Duplex Ni–P–ZrO₂/Ni–P electroless coating on stainless steel*. Journal of Alloys and Compounds, 2015. **630**: p. 189-194.
63. Yusuf, M.M., et al., *Synthesis and characterisation of Ni–B/Ni–P–CeO₂ duplex composite coatings*. Journal of Applied Electrochemistry, 2018. **48**(4): p. 391-404.
64. Meshram, A.P., M.K. Punith Kumar, and C. Srivastava, *Enhancement in the corrosion resistance behaviour of amorphous NiP coatings by incorporation of graphene*. Diamond and Related Materials, 2020. **105**: p. 107795.
65. Ghavidel, N., et al., *Corrosion and wear behavior of an electroless Ni-P/nano-SiC coating on AZ31 Mg alloy obtained through environmentally-friendly conversion coating*. Surface and Coatings Technology, 2020. **382**: p. 125156.
66. Czagány, M. and P. Baumli, *Effect of surfactants on the behavior of the Ni-P bath and on the formation of electroless Ni-P-TiC composite coatings*. Surface and Coatings Technology, 2019. **361**: p. 42-49.
67. Luo, H., et al., *Development of electroless Ni–P/nano-WC composite coatings and investigation on its properties*. Surface and Coatings Technology, 2015. **277**: p. 99-106.
68. Luo, H., et al., *Characterization of microstructure and properties of electroless duplex Ni–W–P/Ni–P nano-ZrO₂ composite coating*. Materials Today Physics, 2018. **4**: p. 36-42.
69. Radwan, A.B. and R.A. Shakoor, *Aluminum nitride (AlN) reinforced electrodeposited Ni–B nanocomposite coatings*. Ceramics International, 2020. **46**(7): p. 9863-9871.
70. Shakoor, R.A., et al., *Properties of electrodeposited Ni–B–Al₂O₃ composite coatings*. Materials & Design, 2014. **64**: p. 127-135.

71. Song, Y., D. Shan, and E. Han, *Comparative study on corrosion protection properties of electroless NiP-ZrO₂ and NiP coatings on AZ91D magnesium alloy*. *Materials and Corrosion-werkstoffe Und Korrosion - MATER CORROS*, 2007. **58**: p. 506-510.
72. Farzaneh, A., et al., *Electrochemical and structural properties of electroless Ni-P-SiC nanocomposite coatings*. *Applied Surface Science*, 2013. **276**: p. 697-704.
73. Sadreddini, S. and A. Afshar, *Corrosion resistance enhancement of Ni-P-nano SiO₂ composite coatings on aluminum*. *Applied Surface Science*, 2014. **303**: p. 125-130.
74. Nava, D., et al., *Effects of Heat Treatment on the Tribological and Corrosion Properties of Electrodeposited Ni-P Alloys*. *International journal of electrochemical science*, 2013. **8**: p. 2670-2681.
75. Balaceanu, M., et al., *Surface Chemistry of Plasma Deposited ZrC Hard Coatings*. *Journal of Optoelectronics and Advanced Materials*, 2005. **7**.
76. Abdelkader, A.M. and D.J. Fray, *Synthesis of self-passivated, and carbide-stabilized zirconium nanopowder*. *Journal of Nanoparticle Research*, 2013. **15**(12): p. 2112.
77. Won, Y.S., et al., *Growth of ZrC thin films by aerosol-assisted MOCVD*. *Journal of Crystal Growth*, 2007. **304**(2): p. 324-332.
78. Kumar, S.S., et al., *Investigations on the effect of substrate temperature on the properties of reactively sputtered zirconium carbide thin films*. *Journal of Alloys and Compounds*, 2017. **695**: p. 1020-1028.

79. Long, Y., et al., *Phase composition, microstructure and mechanical properties of ZrC coatings produced by chemical vapor deposition*. *Ceramics International*, 2014. **40**(1, Part A): p. 707-713.
80. Elias, L., K.U. Bhat, and A.C. Hegde, *Development of nanolaminated multilayer Ni–P alloy coatings for better corrosion protection*. *RSC Advances*, 2016. **6**(40): p. 34005-34013.
81. Pouladi, S., M.H. Shariat, and M.E. Bahrololoom, *Electrodeposition and characterization of Ni–Zn–P and Ni–Zn–P/nano-SiC coatings*. *Surface and Coatings Technology*, 2012. **213**: p. 33-40.
82. Yusuf, M., et al., *Synthesis and characterisation of Ni–B/Ni–P–CeO₂ duplex composite coatings*. *Journal of Applied Electrochemistry*, 2018. **48**.
83. Allahyarzadeh, M.H., et al., *Mechanical properties and load bearing capability of nanocrystalline nickel-tungsten multilayered coatings*. *Surface and Coatings Technology*, 2020. **386**: p. 125472.
84. Alirezaei, S., et al., *Wear behavior of Ni–P and Ni–P–Al₂O₃ electroless coatings*. *Wear*, 2007. **262**(7): p. 978-985.
85. Sadreddini, S., Z. Salehi, and H. Rassaie, *Characterization of Ni–P–SiO₂ nano-composite coating on magnesium*. *Applied Surface Science*, 2015. **324**: p. 393-398.

APPENDIX A – OUTCOMES OF RESEARCH WORK

Publications

- 1) **Osama Fayyaz**, Adnan Khan, R. A. Shakoor*, Anwarul Hasan, Moinuddin M Yusuf, M. F. Montemor, Shahid Rasul, Kashif Khan, M. R. I. Faruque, Paul C. Okonkwo, “Enhancement of mechanical and corrosion resistance properties of electrodeposited Ni-P-TiC composite coatings”, **Scientific Reports, 11 (2021) 5327, (I.F=3.998).**
- 2) Khuram Shahzad, Eman M. Fayyad , Muddasir Nawaz, **Osama Fayyaz**, R. A. Shakoor*, Mohammad K. Hassan, Malik Adeel Ume, M. N. Baig, A. Raza and Aboubakr M. Abdullah, “Corrosion and Heat Treatment Study of Electroless NiP-Ti Nanocomposite Coatings Deposited on HSLA Steel,” **Nanomaterials, 10 (2020), 1932, (I.F=4.324).**
- 3) Mostafa H. Sliem, Khuram Shahzad, Sivaprasad V. N, R. A. Shakoor*,_Aboubakr M. Abdullah, **Osama Fayyaz**, Ramazan Kahraman, Malik Adeel Umer, “Enhanced mechanical and corrosion protection properties of pulsed electrodeposited NiP-ZrO₂ nanocomposite coatings”, **Surface and Coatings Technology, 403 (2020) 126340, (I.F=3.784).**
- 4) **Osama Fayyaz**, A. Bahgat Radwan, Mostafa H. Sliem, R. A. Shakoor, MD Anwarul Hasan, Aboubakr M. Abdullah, “Evaluation of the Mechanical and Corrosion Resistance Properties of electrodeposited Ni-P-ZrC nanocomposite coatings” **Submitted in Surfaces and Interfaces, (I.F=3.724)**
- 5) Khuram Shahzad, A. Bahgat Radwan, **Osama Fayyaz**, R. A. Shakoor, Madeeha Uzma, M. Adeel. Umer, M.N. Baig, A. Raza, “Evaluation of Corrosion and Wear resistance of Pulsed electrodeposited Ni-P-TiC nano composite coatings on HSLA Steel substrate”, **Submitted in Ceramics International, (I.F=3.83)**

Conferences and Posters

- 1) **Osama Fayyaz**, R.A. Shakoor, Elsadig Ahmed, Ramazan Kahraman, Aboubakr M Abdullah, Khaled Youssef, Shahid Rasul, Kashif Khan, Mohammad Rashed Iqbal Faruque, Wei Gao and Fatima Montemor, “Properties of Pulse-electrodeposited Ni-P-ZrO₂ nanocomposite coating”, **Materials Info 2020, 9-10 November 2020**
- 6) **Osama Fayyaz**, Khuram Shahzad, T. Qureshi, I. Fatima, R. A. Shakoor*, El-Sadig Mahdi, “Synthesis and Characterization of Ni-P/TiC Composite Coating through one Step Co-Electrodeposition” **Annual Research Forum-2020, Qatar University**

APPENDIX B : POSTER PRESENTATION



CAM
Center for Advanced Materials

Synthesis and characterization of Ni-P/TiC composite coating through one step co-electrodeposition



كلية الهندسة
College of Engineering
QATAR UNIVERSITY

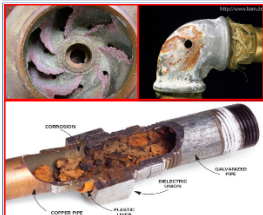
Abstract

- NiP coatings are well known for their corrosion resistance behavior but lack mechanical strength.
- In the present study, the effect of sub micron scale TiC particles on the structural, morphological, mechanical and electrochemical analysis of Ni-P/TiC coating were studied
- Co-electrodeposition of the Ni-P/TiC with varying the composition of TiC namely 0.5, 1.0, 1.5 and 2.0g/L. The surface of the coat represents nodular structure without any defects.
- Vickers microhardness is observed to increase with the composition and attains highest value at 1.5g/L of TiC.
- Improvement in mechanical properties of NiP coatings by the incorporation of TiC particles can be attributed to the dispersion hardening effect

Methodology

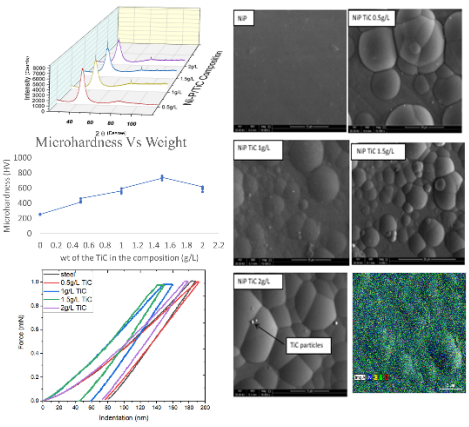


Corrosion Damages



- Metallic surfaces are coated to control deterioration due to "corrosion".
- Corrosion and wear results in decrease plant efficiency and safety concerns.
- 40% of total cost which is billions of dollars can be saved by utilizing proper corrosion prevention techniques.

Results



Conclusion

- Ni-P/TiC composite coatings were successfully developed through an electrodeposition process.
- Incorporation of TiC sub-micron particles to the Ni-P matrix has a significant influence on its structural, surface and mechanical properties.
- Ni-P/TiC composite coatings show improved surface and mechanical properties as compared to Ni-P.
- Ni-P/TiC composite coatings is attractive for many industries.

Acknowledgements This research work was made possible by QUIRCC-146 2020/2021 from Qatar University. QU Central Laboratory Unit (CLU) is acknowledged for SEM/EDX analysis.

APPENDIX C- CONFERENCE 1



Osama Fayyaz et al
Materials Info 2020
Volume 1

Virtual Congress on Materials Science & Engineering

Theme: Materials Science contribution towards future growth

November 09-10, 2020

(Properties of Pulse-electrodeposited Ni-P-ZrO₂ nanocomposite coating)

Osama Fayyaz¹, R.A. Shakoor², Elsadig Ahmed¹, Ramazan Kahraman³, Aboubakr M Abdullah², Khaled Youssef⁴, Shahid Rasul⁵, Kashif Khan⁶, Mohammad Rashed Iqbal Faruque⁷, Wei Gao⁸ and Fatima Montemor⁹

¹Department of Mechanical and Industrial Engineering, Qatar University, Qatar

²Center for Advanced Material, Qatar University, Qatar

³Department of Chemical Engineering, Qatar University, Qatar

⁴College of Art and Science, Qatar University, Qatar

⁵Department of Mechanical and Construction Engineering, Northumbria University, UK

⁶School of Mechanical, Aerospace and Automotive Engineering, Coventry University, UK

⁷Space Science Centre, Institute of Climate Change of the Universiti Kebangsaan Malaysia (UKM), Malaysia

⁸Department of Chemical and Materials Engineering, University of Auckland (UOA), New Zealand

⁹Instituto Superior Técnico (IST), University of Lisbon, Lisbon, Portugal

Corrosion is considered to be major challenge faced by oil and gas industry which becomes more disastrous in heavy operating conditions. In this research, zirconia nanoparticles were incorporated in NiP matrix to study the effect of concentration of ZrO₂ particles in the NiP-ZrO₂ nanocomposite coatings. Low alloy steel was used as the substrate and pulse electrodeposition technique was utilized owing to its advantages over other deposition methods. Co-electrodeposition of various concentrations of zirconia nanoparticles (0.0, 0.25, 0.50, 0.75, and 1.0 g/L) was carried out in the optimized chemical bath. Numerous techniques were adopted to evaluate the structural, morphological, mechanical and electrochemical properties of nanocomposite coating. SEM and EDS results prove the successful reinforcement of zirconia nanoparticles in NiP matrix. XRD and XPS analysis validates the structural formation of pure phase of NiP without any evident defect. An appreciable enhancement in the mechanical properties was noticed with an increase in the amount of zirconia nanoparticles. Likewise, EIS analysis confirms a gradual increase in corrosion protection behavior of the NiP-ZrO₂ nanocomposite coatings with increasing zirconia concentration. The decent mechanical and corrosion resistance properties of NiP-ZrO₂ nanocomposite coatings provide an exciting option for their suitability in numerous applications.

Biography

I am a graduate student at the prestigious institute of Qatar University in the department of mechanical and industrial engineering. I have completed Bachelor of Engineering from Visvesvaraya Technological University India in the field of mechanical engineering with distinction grade throughout my academic career. My interest in material sciences have led me to pursue my research work in advanced material at the Center for Advanced Materials-Qatar University under my guide Dr Abdul Shakoor (impact factor = 385) who has co-authored more than 100 research articles in high impact scientific journal. Currently, my research areas are surface modification and surface characterization through state-of-the-art techniques. I have participated in various research-based internships. I have co-authored couple of published articles in composite coating.

of1806234@qu.edu.qa

MATERIALS INFO 2020

NOVEMBER 09-10, 2020



OPEN Enhancement of mechanical and corrosion resistance properties of electrodeposited Ni–P–TiC composite coatings

Osama Fayyaz^{1,2}, Adnan Khan¹, R. A. Shakoor^{1,3}, Anwarul Hasan², Moinuddin M. Yusuf⁴, M. F. Montemor⁵, Shahid Rasul⁴, Kashif Khan⁵, M. R. I. Faruque⁶ & Paul C. Okonkwo⁷

In the present study, the effect of concentration of titanium carbide (TiC) particles on the structural, mechanical, and electrochemical properties of Ni–P composite coatings was investigated. Various amounts of TiC particles (0, 0.5, 1.0, 1.5, and 2.0 g L⁻¹) were co-electrodeposited in the Ni–P matrix under optimized conditions and then characterized by employing various techniques. The structural analysis of prepared coatings indicates uniform, compact, and nodular structured coatings without any noticeable defects. Vickers microhardness and nanoindentation results demonstrate the increase in the hardness with an increasing amount of TiC particles attaining its terminal value (593HV_{0.05}) at the concentration of 1.5 g L⁻¹. Further increase in the concentration of TiC particles results in a decrease in hardness, which can be ascribed to their accumulation in the Ni–P matrix. The electrochemical results indicate the improvement in corrosion protection efficiency of coatings with an increasing amount of TiC particles reaching to ~ 92% at 2.0 g L⁻¹, which can be ascribed to a reduction in the active area of the Ni–P matrix by the presence of inactive ceramic particles. The favorable structural, mechanical, and corrosion protection characteristics of Ni–P–TiC composite coatings suggest their potential applications in many industrial applications.

Corrosion is the gradual destruction of metal because of the chemical reaction with its environment. Corrosion has a large share in the failure of equipment and loss of production. Corrosion behaves like a slow poison for the destruction of industrial finished products, machinery, pipelines from onshore to offshore sites etc^{1,2}. Corrosion is the major challenge faced by many industries nowadays due to various failures such as fatigue stress initiation and creep failure rooting back to corrosion³. Corrosion of valves in the reverse osmosis system results in equipment failure⁴. The loss of containment in the onshore pipelines is threatened by the corrosive environment⁵. One of the various corrosion types, such as pitting, is one of the hazardous forms of corrosion in marine and offshore structures⁶. Nearly 10 to 30% of the maintenance budget is spent on corrosion control by the oil refinery plants, as deduced by Finágar et al.⁷. Shekari et al.⁸ mentioned the report of NACE, which estimated the global cost of corrosion to be US\$2.5 trillion in 2013, which was equivalent to 3.4% of the Gross Domestic Product (GDP).

Understanding of corrosion mechanism has led to the development of various techniques to prevent and minimize corrosion damages. Surface modification techniques provide a dual benefit of corrosion prevention and improvement of the surface properties such as hardness, abrasion, wear, inertness, and erosion, avoiding replacing the bulk of material⁹. Various surface modification techniques like carburizing, nitriding, carbonitriding, flame hardening, laser hardening, chemical vapor deposition and physical vapor deposition, etc. have been reported in the literature¹⁰. Providing a barrier between the corroding environment and the base metal with a corrosion-resistant layer is termed as a coating, which is primarily applied to prevent the loss of metal. The coating of base metal with a varying thickness can be carried out in various ways¹¹. Electrodeposition coating

¹Center for Advanced Materials (CAM), Qatar University, 2713 Doha, Qatar. ²Department of Mechanical and Industrial Engineering, College of Engineering, Qatar University, 2713 Doha, Qatar. ³Departamento de Engenharia Química, Centro de Química Estrutural, Instituto Superior Técnico, Universidade de Lisboa, Av Rovisco Pais, 1049-001 Lisboa, Portugal. ⁴Department of Mechanical and Construction Engineering, Northumbria University, Newcastle, UK. ⁵School of Mechanical, Aerospace and Automotive Engineering, Coventry University, Coventry, UK. ⁶Space Science Centre, Institute of Climate Change of the Universiti Kebangsaan Malaysia (UKM), Bangi, Malaysia. ⁷Department of Mechanical and Mechatronics Engineering, College of Engineering, Dhofar University, Salalah, Oman. ⁸email: shakoor@qu.edu.qa

has gained wide acceptance in academia and industries due to its cost-effectiveness, simplicity, and capability to produce expeditious results^{12,13}. It is also used in the decorative sector, and the growth of the electroplating market is forecasted to reach US\$ 21 billion by 2026¹⁴.

Ni–P coatings have found applications in numerous industries such as aerospace, electronics, and automotive due to their good wear resistance, a higher degree of hardness, lower friction coefficient, and interesting anti-corrosive resistance¹⁵. A careful selection of coating bath composition and optimization of electrodeposition parameters is vital to achieving the desired properties of Ni–P coating, leading to widening their range of applications^{16,17}. There are mainly two proposed mechanisms for the formation of Ni–P coatings over a substrate in the respective chemical bath and operating conditions, namely direct and indirect mechanisms. Among these two, the latter i. e. indirect coating mechanism is mainly supported by the majority of the researchers. More details about the mechanism of electrodeposition of Ni–P coatings on the substrates can be glanced in the review¹⁸. Ni–P coatings have the edge over other alloy coatings such as Ni–Cu, Ni–Fe, and Ni–Co and even Ni-composites for the fabrication of microsystems¹⁹. For instance, Ni–P–Co coatings are reported to have better hardness and lubricity, along with many other appealing characteristics^{19,20}. Various chemical baths consisting of sulfate, sulfamate, and methanesulfonate have been reported in the literature for obtaining Ni–P coatings²¹.

Co-deposition of reinforcing particles to enhance Ni–P coatings specific properties through composites formation is a leading trend in the academic and classical industries^{22–24}. Recently, research in the area of Ni–P composite coatings is quite common, which has led to the development of some novel composite coating systems^{25–33}. Although the Ni–P–X (X = TiO₂, SiO₂, ZrO₂, CeO₂ etc.) composite coatings are grabbing substantial attention^{24–27}, the effect of electrodeposited titanium carbide (TiC) has not been fully investigated in spite of its attractive properties such as high hardness, wear resistance, corrosion resistance and high stability at elevated temperature^{28,29}. The present study deals with the synthesis and characterization of Ni–P–TiC composite coatings developed through conventional electrodeposition techniques. This work is mainly focused on the electrodeposition which is completely different technique from electroless deposition. Also, the chemical bath modified and the optimized parameters for our study is completely different from the previously reported work. Moreover, our study also considers the effect of increasing the TiC particles (< 200 nm) which on one hand improves the mechanical properties through matrix-reinforcement composite phenomenon and on other hand improves the corrosion resistance by blocking the active surface area. This further endorses the novelty of our present study that the effect of various TiC particles concentrations on the structural, surface, mechanical, and corrosion-resistant properties of Ni–P coatings have been deeply investigated. The results evidence an improvement in the mechanical properties and corrosion resistance supporting the use of Ni–P–TiC composite coatings for onshore and off shore pipelines³⁰, tool finish and machining hard surfaces⁴¹, microsystems and micro engines¹⁹, as a replacement for hard chromium coatings¹⁶, and catalytic coatings for hydrogen evolution in water electrolysis¹⁸ etc.

Material and methods

Materials. Nickel sulphate hexahydrate, nickel chloride hexahydrate, boric acid, orthophosphoric acid, and sodium hypophosphite were bought from the Sigma Aldrich, Germany. Sodium chloride and submicron-sized titanium carbide (TiC) powder with an average particle size < 200 nm and purity of 99.9% were also imported from Sigma Aldrich.

Sample preparation and coatings synthesis. The electrodeposition of Ni–P and Ni–P–TiC composite coatings was carried out on the mild steel substrate. Firstly, the mild steel sheet was cut down to the 32 mm square sheets through sheet metal operation. The mild steel samples were then polished to obtain a mirror-like surface with SiC abrasive papers of grit size 120, 220, 320, 500, 800, 1000, and 1200. The substrates were washed with soap and water before moving to the next abrasive paper. After grinding, the substrates were sonicated in the acetone for half an hour. One side of the substrates was covered with insulating tape to avoid electrodeposition on both sides of the substrates. The substrates were activated in 20% HCl solution for about 45 s, rinsed in distilled water, and finally put in the coating bath. During the electrodeposition process, the dc power supply's negative electrode was connected to the substrate forming a cathode, and the positive electrode of the power supply was connected to the nickel sheet to provide an anode. The schematic diagram of the electrodeposition experimental setup is represented in Fig. 1. The nickel sheet (anode) and the substrate (cathode) were placed parallel and face to face each other at a distance of approximately 30 mm in the coating bath. The optimized electrodeposition conditions are tabulated in Table 1. Ni–P and Ni–P–TiC composite coatings were developed at 65 °C ± 2. The time of the coatings is half an hour from the start of the power supply. The coating bath was agitated at 300 ± 5 rpm for 60 min before initiating the electrodeposition process to avoid settling down of the TiC particles. The coating bath was kept agitated during the entire coating process at 300 rpm for uniform distribution of reinforcing particles into the Ni–P matrix.

Sample characterization. The thickness of the synthesized Ni–P and Ni–P–TiC composite coatings was determined by thickness gauge (model BDYSTD-E, USA). Structural characterization of the synthesized coatings was carried out employing X-ray diffractometer (PANalytical, Empyrean, UK) fitted with Cu K α radiations with the scanning step of 0.02° in the range of 2 θ from 10° to 90°. The field emission scanning electron microscope (FE-SEM-Nova Nano-450, Netherlands), atomic force microscopy (AFM-USA) and high-resolution transmission electron microscope (HR-TEM FEI : TECNAI G2 FEG 200 kV) were used to perform the morphological study. The composition of the prepared coatings was also determined by X-ray photoelectron spectroscopy—XPS (Kratos Analytical Ltd, UK) using a monochromatic Al-K α X-Ray source. The hardness of the prepared coatings was tested with Vickers microhardness tester (FM-ARS9000, USA). The measurement of the

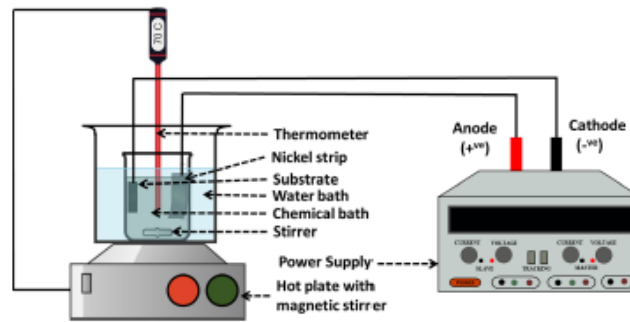


Figure 1. Schematic diagram of the electrodeposition process to develop Ni–P–TiC composite coatings.

Chemical bath and operating conditions	Bath Ni–P/TiC
Nickel Sulfate hexahydrate	250 g L ⁻¹
Nickel Chloride hexahydrate	15 g L ⁻¹
Boric acid	30 g L ⁻¹
Sodium Chloride	15 g L ⁻¹
Phosphoric acid	6 g L ⁻¹
Sodium hypophosphite	20 g L ⁻¹
TiC particles concentration	0, 0.5 g L ⁻¹ , 1 g L ⁻¹ , 1.5 g L ⁻¹ and 2 g L ⁻¹
pH	2.0 ± 0.2
Bath temperature	65 ± 2 °C
Deposition time	30 min
Current density	50 mA/cm ²
Bath agitation	300 rpm

Table 1. Optimized bath composition and parameters for co-electrodeposition of Ni–P–TiC composite coatings.

microhardness was carried out at 100 gf with the dwell time of 10 s on the surface of the coatings. The nanoindentation measurements were performed employing AFM device MFP-3D Asylum research (USA) equipped with silicon probe (Al reflex coated Veeco model-OLTESPA, Olympus; spring constant: 2 Nm⁻¹, resonant frequency: 70 kHz). All measurements were carried out under ambient conditions using standard topography A.C. air (tapping mode in the air). The indentation was performed with Berkovich diamond indenter tip with a maximum 1 mN indentation force (loading and unloading rate: 200 μN/s and dwell time at maximum load: 5 s). Oliver and Pharr's method was used to find contact penetration from the unloading curves. The electrochemical impedance spectroscopy (EIS) studies were carried out with Gamry cell in which saturated silver/silver chloride (Ag/AgCl) was used as the reference electrode, whereas graphite and prepared coated samples were employed as counter and working electrodes, respectively. EIS was measured by AC signal with 10 mV of amplitude within the frequency range of 10⁵–10⁻² Hz at open circuit potential. Moreover, potentiodynamic studies were carried out at ambient room temperature with a scan rate of 0.167 mV s⁻¹ after the determination of open circuit potential for more than 10 min of stabilization of complete cell. A constant surface area of 0.765 cm² of all tested samples was exposed to 3.5 wt% NaCl solution in the entire study^{33,42,43}.

Results and discussion

XRD analysis. The structural analysis of the electrodeposited Ni–P and Ni–P–TiC composite coating was carried out through XRD and the spectra of NiP and Ni–P–TiC composite coatings containing various compositions of TiC (0, 0.5, 1.0, 1.5, 2 g L⁻¹) are shown in Fig. 2. The semi-amorphous structure of the coatings can be deduced from the broad peaks in all the cases, and the broad peak located at 2θ ~ 45.5 can be assigned to the Ni (111) plane of face-centered cubic (FCC) structure. The formation of an amorphous structure can be ascribed to the lattice distortion experienced by the nickel crystal structure due to the presence of phosphorous atoms, which hinders the propagation of face-centered cubic occupancy of nickel atoms⁴⁴. The amorphous nature of the coatings has already been reported^{38,15,45} along with nanocrystalline structure as reported in the literature^{46,47}.

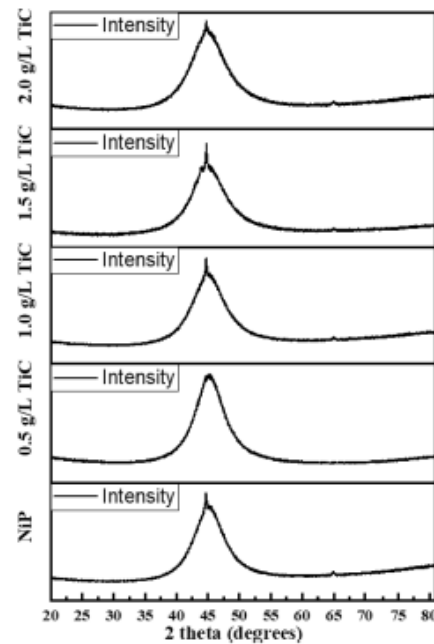


Figure 2. XRD spectra of Ni-P and Ni-P-TiC composite coatings containing various concentrations of TiC particles.

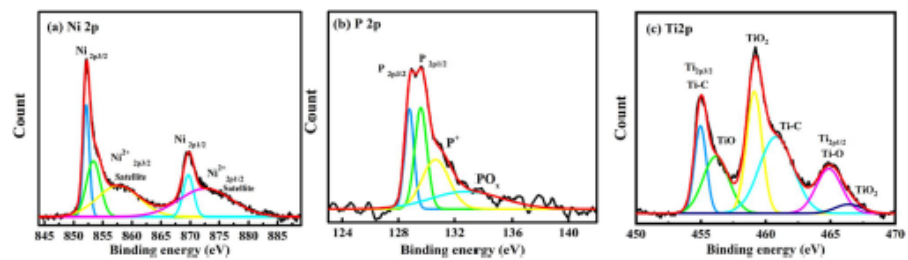


Figure 3. XPS spectra presenting the elemental composition of Ni-P/1.5 g L⁻¹ TiC composite coatings, (a) Ni2p, (b) P2p and (c) Ti2p.

The diffraction peaks of the TiC were not observed in the XRD spectra, probably due to their low contents in the Ni-P matrix. Similar results have also been reported in the literature^{29,48}.

XPS analysis. The presence of TiC in the Ni-P TiC composite coatings was confirmed using XPS analysis. To avoid any repetition, the fitted data of individual photoionizations and their corresponding chemical states only the 1.5 g L⁻¹ TiC composition is presented in Fig. 3. High energy resolution spectra of Ni2p (Fig. 3a) region contains two distinct ionizations: Ni 2p_{3/2} and Ni 2p_{1/2} at 852.2 eV and 869.9 eV assigned to Ni in the metallic state, whereas the peaks of Ni²⁺ at 853.3 eV, 857.6 eV, and 872.7 eV corresponds, respectively to the NiO and/or Ni(OH)₂ of Ni 2p_{3/2} and Ni 2p_{1/2}. The high intensity peak for nickel proves the presence of metallic nickel. The formation of Ni(OH)₂ and NiO can be linked to the presence of hydroxyl ion from the aqueous electrolytic bath

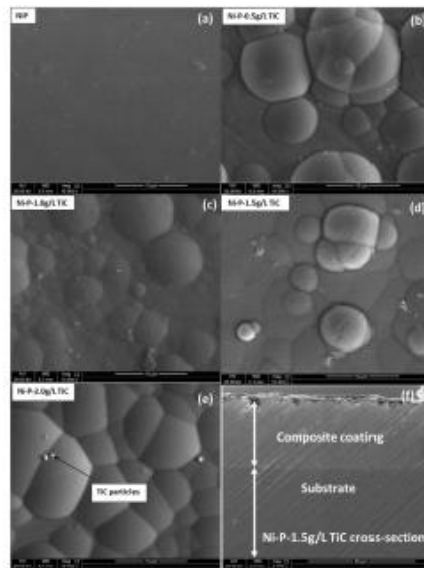


Figure 4. FE-SEM micrographs of the Ni-P (a) and Ni-P-TiC composite coating with various concentrations of TiC (b,c,d,e). A cross-sectional micrograph (f) of Ni-P-TiC composite coatings with 1.5 g L^{-1} of TiC.

Coatings Composition	Average coating thickness
Ni-P	$17 \mu\text{m} \pm 2$
Ni-P 0.5 g L^{-1} TiC	$17 \mu\text{m} \pm 2$
Ni-P 1.0 g L^{-1} TiC	$17.4 \mu\text{m} \pm 2$
Ni-P 1.5 g L^{-1} TiC	$17.2 \mu\text{m} \pm 2$
Ni-P 2.0 g L^{-1} TiC	$17.6 \mu\text{m} \pm 2$

Table 2. Average thickness of Ni-P and Ni-P-TiC composite coatings measured with thickness gauge meter.

and other surface oxidation phenomenon^{33,49}. Concerning the P2p ionization, the peaks at 128.8 and 129.5 eV can be assigned to the elemental phosphorous (P) in the bulk of electrodeposited Ni-P-TiC composite coating, respectively (Fig. 3b). It can be noticed that the peak at 130.69 eV is due to (i) elemental phosphorous hypophosphite and/or (ii) intermediate phosphorous ions (P(I) and/or P(III)) valence which are presented in the inner portion of the protective film of the Ni-P coatings. However, peaks at 132.7 eV can be due to the combination of oxides and/or hydroxides (P_2O_3 and/or P-OH) chemical states³³. The high-resolution spectra of the Ti2p spectrum were deconvoluted into three doublet peaks (Fig. 3c) of titanium carbide, based at 454.9 and 460.8 eV, titanium oxides at 456.1 and 464.8 eV and TiO_2 at 459.2 and 466.4 eV as previously reported^{50,51}.

Microstructural analysis. The morphology of the Ni-P and Ni-P/TiC composite coatings containing various concentrations of TiC particles was studied with FE-SEM as specified in Fig. 4. Ni-P coatings (Fig. 4(a)) does not show the formation of a well-defined nodular structure. A similar morphology of Ni-P coatings has been reported in the literature^{29,52}. On the other hand, FE-SEM micrographs of Ni-P-TiC composite coatings (Fig. 4b–e) show the compact, nodular morphology without any noticeable defects. The presence of TiC particles can also be observed in the FE-SEM images, especially at the 2.0 g L^{-1} of composition in good agreement with literature^{33,53}. Figure 4f shows the cross-section of Ni-P-TiC (1.5 g L^{-1}) composite coatings. A smooth and well-adherent coating, without any apparent defects can be observed, together with a uniform interface. A uniform coating thickness of $\sim 15 \mu\text{m}$ is achieved.

The coating thickness was also measured with the coating gauge meter and presented in Table 2. It can be noticed that the coating thickness under all identical conditions are similar, and there are no noticeable changes

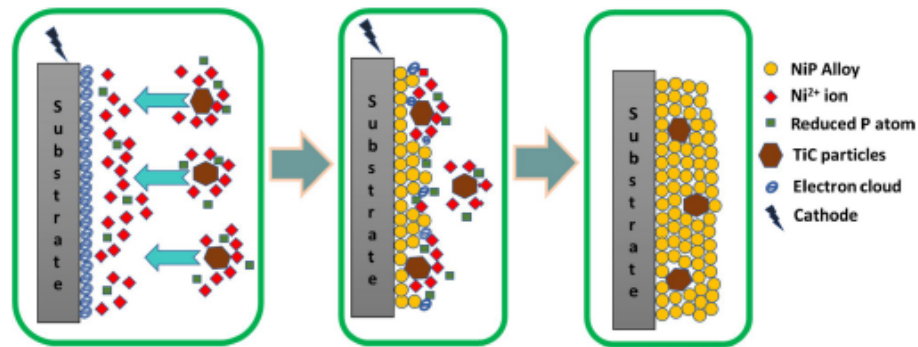


Figure 5. Schematic diagram for the co-deposition of TiC particles at the cathode (substrate) to form Ni-P-TiC composite coatings.

in the thickness. It is worthy of mentioning that the reported values are an average of five readings. A slight difference in thickness of coatings measured through FE-SEM analysis may be due to the surface preparation required for the test.

Co-deposition mechanism of various reinforcements in Ni-P matrix has been proposed by many researchers. Guglielmi⁵⁴ proposed a model containing two steps in which firstly, particles adsorb weakly on the cathode surface by Van der Waals forces and then during the second stage strong adsorption by coulombic forces. This model fails to account for particle size and hydrodynamics of the deposition. Bercot et al.⁵⁵ formulated a corrective factor to this model for accounting for magnetic stirring in their study, whereas Bahadormanesh and Dolati modified Guglielmi's model for the deposition of a high-volume percentage of the second phase and carried out a parametric study⁵⁶. Moreover, Fransær et al. devised a trajectory model in which they presented an analysis of various forces on a spherical particle in a rotating disk electrode system⁵⁷. According to Cetis et al.⁵⁸, the electrodeposition mechanism may consist of five steps; (i), formation of an ionic cloud around the reinforcement particles, (ii) movement of reinforcement particles by forced convection towards the hydrodynamic layer of the cathode, (iii) diffusion of the particle through double layer, (iv) adsorption of the particle along with the ionic cloud at the cathode surface and (v) reduction of the ionic cloud leading to an irreversible entrapment of reinforcement particles in the metal matrix. As per the above discussion, it seems there are mainly three steps involved in the co-deposition of the reinforcement particles, such as TiC during the electrodeposition process; (i) movement of particles from bulk electrolyte to hydrodynamic boundary layer of the cathode which are governed by a combination of forced convection and electrophoresis, (ii) diffusion and adsorption of particles at the cathode due to Van der Waal forces, and (iii) permanent incorporation of particles due to the reduction of ionic cloud around the reinforced particle. This three-step phenomenon can be described in the schematic diagram in Fig. 5.

The co-electrodeposited of TiC in the Ni-P matrix was further evaluated with EDS analysis. The EDS analysis of Ni-P and Ni-P-TiC composite coatings containing various concentrations of TiC particles, is presented in Fig. 6a-f. The elemental mapping of Ni-P/TiC composite coatings is shown as an inset of Fig. 6. The presence of titanium (Ti), carbon (C), Phosphorus (P), and nickel (Ni) confirm the incorporation of TiC particles into the Ni-P matrix. Table 3 shows the weight percentage of various elements in the as prepared composite coatings. As for Ni-P coating, nickel constitutes almost 89.51 wt.% and the remaining is balanced by phosphorus. Introduction and increase of the concentration of TiC powder in the chemical bath does affect the concentration of nickel in the deposit, which appreciably decreases without significant effect over the phosphorus content which remains around 10 wt.% in all the coatings. The titanium content in the deposits increases from 0.39 to 0.84 wt.% when the concentration in the chemical bath is increased from 0.5 to 2.0 g L⁻¹. However, the excessive weight percentage of carbon can be attributed to the combination of various effects such as presence of carbon in the titanium carbide compound, impurities related to environment and surface preparation for the microscopic analysis. Incorporation of TiC particles can be inferred from the titanium peaks in the EDS plot of 0.5, 1.0, 1.5, 2.0 g L⁻¹ and cross-section of 1.5 g L⁻¹ of TiC. The carbon peak in all the plots can be attributed to the steel substrate's carbon composition due to background interference as previously reported by Pouladi et al.⁵⁹. Peaks of iron are also observed in the cross-sectional EDS analysis which can be ascribed to the steel substrate. Further, corresponding EDS elemental mapping results shown as an inset of corresponding compositions depicts the clear distribution of Ni, P, and TiC particles in the Ni-P matrix.

In order to further investigate the microstructural properties of the deposit, high resolution-transmission electron microscopy analysis were carried out for the Ni-P-2.0 g L⁻¹ TiC. Figure 7 shows the TEM bright field micrographs of electrodeposited Ni-P-2.0 g L⁻¹ TiC composite coating at various magnifications. All the images clearly reveal the presence of a separate second phase of TiC particles within the Ni-P matrix. Figure 7a presents a low magnification micrograph of the composite coating. The excessive darkness is due to the thickness of the coating deposited on the copper grid for TEM analysis. Figure 7b is the enlarged image at the marked location

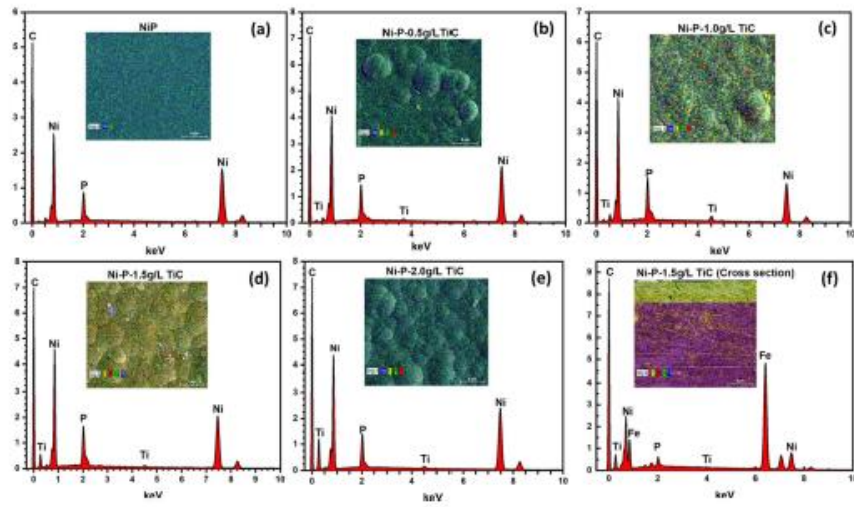


Figure 6. EDS analyses along with elemental mapping of Ni-P (a) and various compositions of Ni-P-TiC composite coatings, (b) 0.5 g L⁻¹, (c) 1.0 g L⁻¹, (d) 1.5 g L⁻¹, (e) 2.0 g L⁻¹ and (f) cross-section of 1.5 g L⁻¹ of Ni-P-TiC composite coatings.

S. no	Sample designation	Ni (wt.%)	P (wt.%)	Ti (wt.%)	C (wt.%)
1	Ni-P	89.51	10.49	—	—
2	Ni-P-0.5 g L ⁻¹ TiC	73.47	9.94	0.39	16.2
3	Ni-P-1.0 g L ⁻¹ TiC	69.74	9.82	0.64	19.8
4	Ni-P-1.5 g L ⁻¹ TiC	66.19	10.52	0.79	22.5
5	Ni-P-2.0 g L ⁻¹ TiC	66.58	9.68	0.84	22.9

Table 3. EDS quantitative analysis of Ni-P and Ni-P-TiC composite coatings.

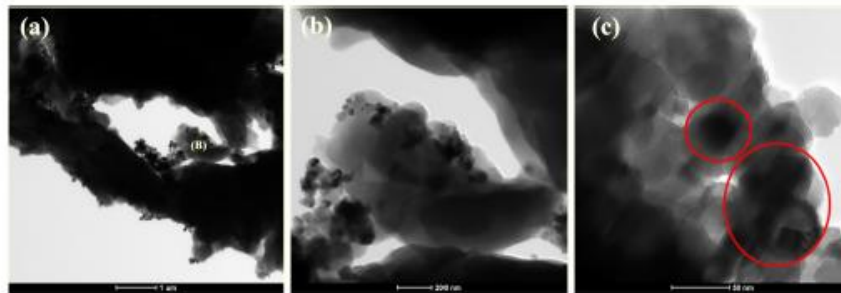


Figure 7. TEM micrographs of Ni-P-2.0 g L⁻¹ TiC at various magnification of (a) high magnification (b) magnified portion marked (B) in (a) and (c) showing an interface of the Ni-P matrix and TiC reinforcement.

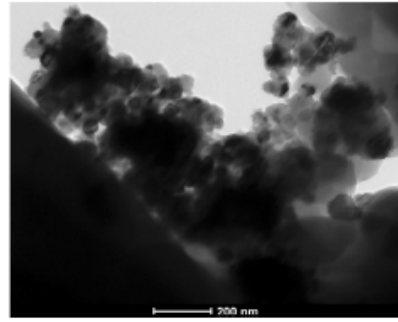


Figure 8. TEM micrograph of Ni-P-2.0 g L⁻¹ TiC presenting the agglomeration of the particles in the Ni-P matrix.

(B) in Fig. 7a presenting the amorphous structure of the composite coating with the lighter region corresponding to the nickel lattice formation as also reported by Huang et al. in their exhaustive study of microstructure in the Ni-P coating⁶⁰. An irregular dark network is observed in the Fig. 7b which is prevalent to the mid-high phosphorus content within the electrodeposited composite coatings as previously reported^{60,61}. Figure 7c is the micrograph at very high magnification presenting the cubical polygonal structure of the reinforced titanium carbide embedded in the Ni-P matrix. The matrix-reinforcement interface can be clearly distinguished as comparatively sharp contrast can be identified in the micrographs. According to literature, titanium carbide particles are reported to have regular polygonal cubical structure⁶².

FE-SEM images could not accurately provide the evidence of aggregation or agglomeration of TiC particles during the fabrication of the Ni-P-2.0 g L⁻¹ TiC composite coating. TEM analysis further confirms the agglomeration or aggregation of the cubical polygonal TiC particles, which are visible in Fig. 8 for the Ni-P-2.0 g L⁻¹ TiC. Agglomeration of the particles in composite coatings has been confirmed through TEM micrograph as reported in literature^{61,63}.

The surface topography of the electrodeposited Ni-P and Ni-P-TiC composite coatings was investigated through atomic force microscopy (AFM). Three-dimensional images of Ni-P and Ni-P/TiC composite coatings with the various compositions of TiC particles are presented in Fig. 9a–e. It is observed that the Ni-P coatings indicate a relatively smooth surface when compared with the Ni-P-TiC composite coatings. The Ni-P-TiC composite coatings' surface is composed of valleys and intrusions due to presence of TiC particles into the Ni-P matrix that provides a rougher texture. The quantitative analysis of surface topography indicates that the addition of TiC particles into the Ni-P matrix has resulted in an increase in the surface roughness. The average surface roughness (Ra) increases with the increasing amount of TiC particles and the average value increased from 6.786 nm (Ni-P coatings) to 33.014 nm (Ni-P/TiC-2.0 g L⁻¹), contributing five times enhancement in the surface roughness. Moreover, Rq (root mean square value of the roughness) is also presented which shows the similar trend as the average roughness as presented in the Fig. 9. Furthermore, Rz values also displays the similar increasing trend from 18.6 nm roughness of Ni-P coating to the successive increase upto 53.8 nm, 58.5 nm, 70.2 nm and 77.6 nm for the increase in the concentration of TiC particles of 0.5 g L⁻¹, 1.0 g L⁻¹, 1.5 g L⁻¹ and 2.0 g L⁻¹ in the chemical bath. The increase in the surface roughness with an increasing amount of TiC particles can be attributed to the presence of insoluble and hard ceramic particles, which provides jerks and barriers to the free movement of the AFM cantilever tip. These findings are consistent with the previous studies^{29,35}.

Mechanical properties. *Vickers microhardness.* Vickers microhardness results of Ni-P and Ni-P-TiC composite coatings are presented in Fig. 10. As seen, Ni-P coating's hardness value is around 500HV, which increases to ~ 530 HV and ~ 550 HV on the incorporation of 0.5 g L⁻¹ and 1 g L⁻¹ of the TiC particles, respectively. The hardness value reaches its maximum value of ~ 593 HV at the composition of 1.5 g L⁻¹. The increase in the hardness is about 19%, which can be attributed to the dispersion hardening effect and improvement in the load-bearing characteristics of the matrix due to the formation of a composite structure, aligned to previously reported literature^{64,65}. After reaching to its terminal value, the microhardness decreases with further increase in TiC particles and it decreases to ~ 550 HV at 2.0 g L⁻¹. A decrease in the hardness value at 2.0 g L⁻¹ can be attributed to the excessive aggregation of the TiC particles in Ni-P matrix, which impairs the load-bearing properties of the Ni-P/TiC composite coatings. This observation is also consistent with previous reports⁶⁶.

Nanoindentation. The indentation tests of the Ni-P and Ni-P-TiC composite coatings were performed to have an insight of the mechanical response of the developed coatings. The loading/unloading indentation profiles of Ni-P and Ni-P-TiC composite coatings containing various concentrations of TiC particles are presented

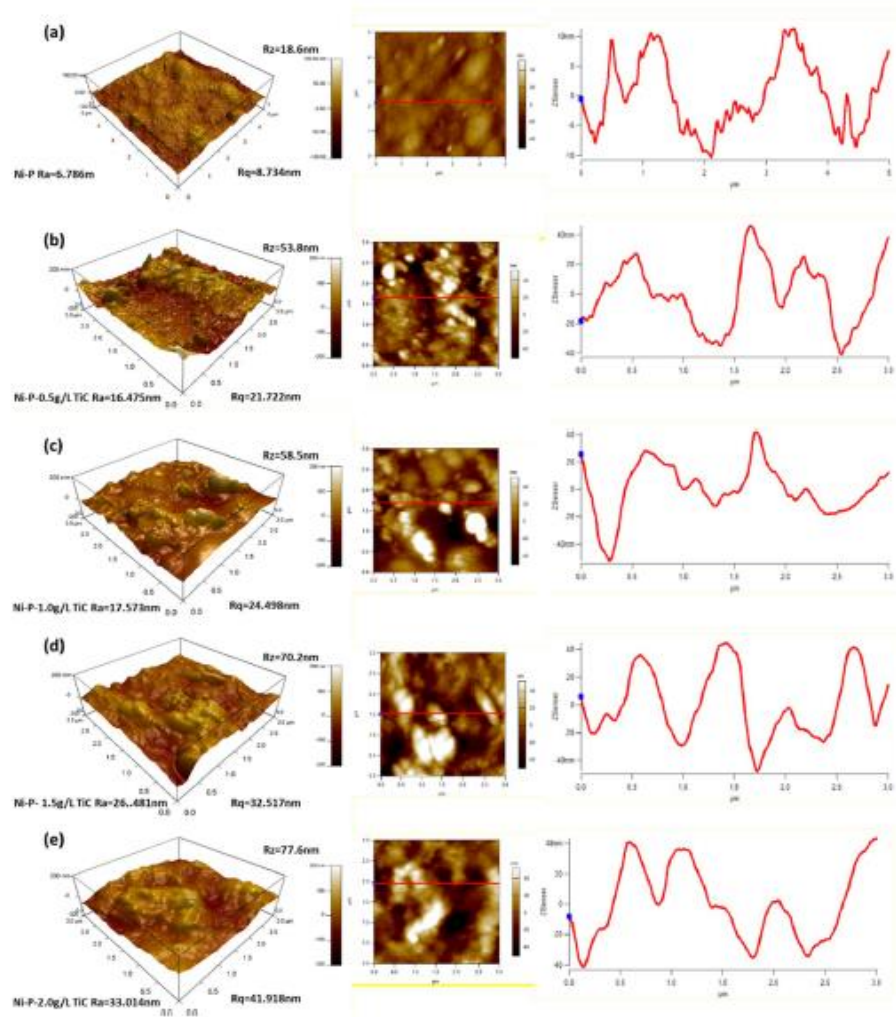


Figure 9. 3D-AFM micrograph along with their corresponding surface roughness profiles of the (a) Ni-P, Ni-P-TiC composite coatings (b) 0.5 g L^{-1} , (c) 1.0 g L^{-1} , (d) 1.5 g L^{-1} , and (e) 2.0 g L^{-1} of TiC particles.

in Fig. 11. A gradual decrease in indentation depth with an increasing amount of TiC particles in the Ni-P matrix is evident in Fig. 11a. The Ni-P coatings demonstrate an indentation depth of $\sim 50 \text{ nm}$, which reduces to 23.67 nm at the composition of 1.5 g L^{-1} of TiC. The decrease in depth is due to the enhancement in the hardness of the coatings, which is directly associated with the dispersion hardening effect and improvement in the load-bearing properties, as explained previously. It can be further noticed that there is a decrease in the indentation depth of $\sim 7 \text{ nm}$ at the terminal composition (2.0 g L^{-1} TiC). This is because of the fact that an excessive amount of reinforcement accumulates in the matrix and thus harms the mechanical properties in agreement with previous studies^{67,68}. The maximum decrease in the indentation depth is observed at 1.5 g L^{-1} of TiC due to the uniform distribution of the reinforcing phase in the matrix without any significant agglomeration. The loading/unloading curves are uniform without any kinks, suggesting that the synthesized coatings are free of cracks

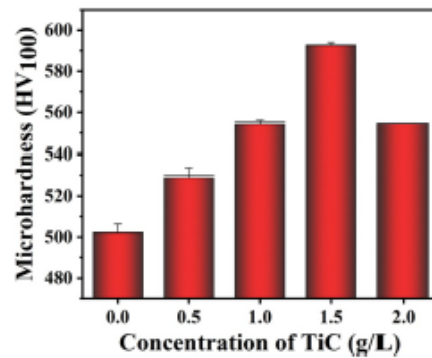


Figure 10. Vickers microhardness of Ni-P and Ni-P-TiC composite coatings containing various concentrations of TiC particles.

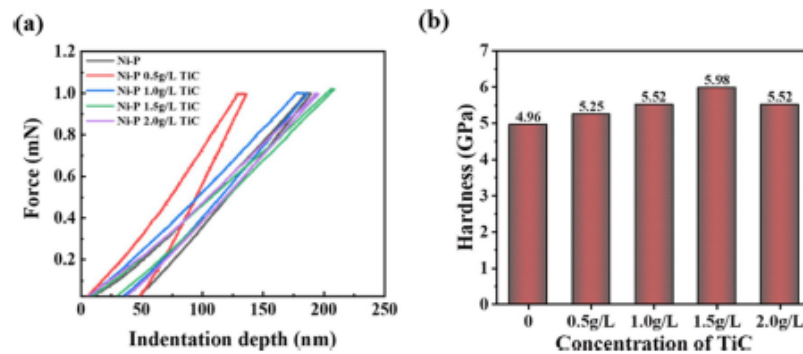


Figure 11. Nanotindentation results of Ni-P and Ni-P-TiC composite coatings containing various concentrations of TiC particles; (a) loading/unloading profiles and (b) hardness.

and pores. For more accurate comparison, a quantitative analysis of the indentation results obtained through Oliver and Pharr technique is also represented in Fig. 11b. It can be noticed that the hardness of Ni-P coatings is 4.96 GPa, which increases with increasing concentration of TiC particles in the Ni-P matrix, reaching its terminal value of 5.98 GPa at the composition of 1.5 g L⁻¹. Further increase of TiC particles concentration in the Ni-P matrix decreases hardness and it attains a value of 5.52 GPa at the TiC composition of 2.0 g L⁻¹. This result further supports the observation that incorporation of ceramic TiC increases the hardness of the NiP matrix, in good agreement with literature^{33,49}. The decrease in the hardness for 2.0 g L⁻¹ can be due to agglomeration of TiC particles in the Ni-P matrix. The nanotindentation results are in agreement with the Vickers microhardness test results.

Corrosion behavior

Electrochemical impedance spectroscopy (EIS). The corrosion resistance of the coatings was studied through electrochemical impedance spectroscopy (EIS) and potentiodynamic polarization techniques. The EIS plots (Bode plots) of the substrate (carbon steel), NiP, and NiP-TiC composite coatings containing various concentrations of TiC are presented in Fig. 12a,b. Experimental data were fitted using an equivalent circuit based on a modified Randle circuit. It is composed of two-time constants in cascade assigned to the composite coatings and metal-coating interface exposed at the bottom of conductive paths, as presented in Fig. 13a,b. The various elements in the circuit account for: R_s —electrolyte resistance, R_{po} —pore resistance, R_{ct} —polarization resistance, and constant phase elements (CPE1 and CPE2) instead of capacitors to account for surface inhomogeneity. The constant phase elements can be calculated by the following equation³³:

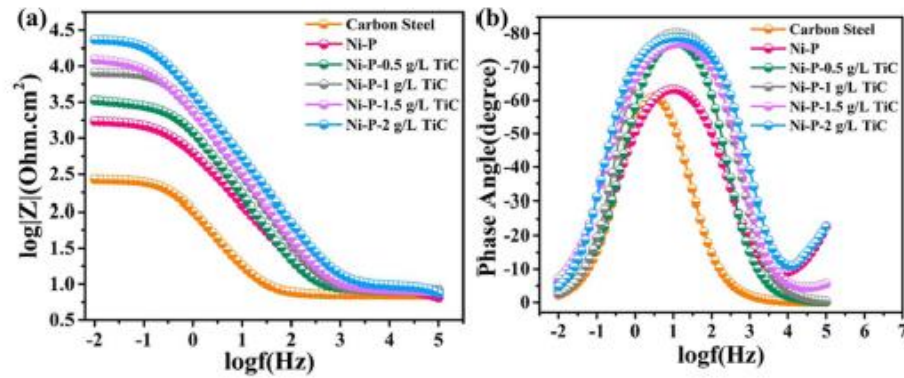


Figure 12. (a) Bode plots of the substrate, Ni-P, and Ni-P-TiC composite coatings containing the magnitude plot and (b) phase angle plot after 2 h of immersion in 3.5wt% NaCl solution.

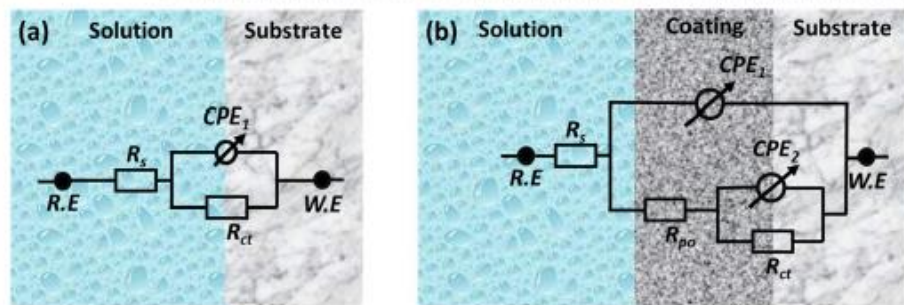


Figure 13. Equivalent electric circuit used for fitting the experimental EIS data for (a) polished carbon steel used as substrate, (b) Ni-P and Ni-P-TiC composite coatings containing different concentrations of TiC particles.

$$\frac{1}{Z_{CPE}} = Q(j\omega)^n$$

where Q is the admittance and ω is the angular frequency of the alternating signal and n is the exponent of CPE which determines the capacitance nature, i.e., when “ n ” approaches unity, the CPE approaches to pure capacitance and the element behaves like an ideal capacitor³³.

Referring to Fig. 12, the medium-high-frequency regions of the Bode plot for carbon steel evidence one time constant, while for the coated samples there is a broadening of the phase angle, suggesting two overlapped time constants—the one associated to the composite coating and another to the interfacial phenomena at the bottom of pores formed in the coating. The magnitude plot indicates that the corrosion resistance of the carbon steel sample is very low $\sim 270 \Omega \text{ cm}^2$, a value that was obtained after fitting the experimental data using the proposed equivalent circuit (Fig. 13a). Ni-P coatings show an improvement in the impedance value of one order of magnitude which can be ascribed to the formation of the hypophosphite layer due to electrochemical reactions of the salt solution with the surface of Ni-P coating^{30,31}. The inclusion of secondary phase TiC particles in the Ni-P matrix further changes the impedance response, leading to the broadening of the phase angle plot. This trend indicates, by the one hand, a more protective composite coating (shift towards higher frequencies) and, on the other hand, the presence of other processes (decreased corrosion activity) as previously reported in literature^{33,42}. The increased impedance in the composite coatings can be attributed to the reduction on the number active corrosion sites due to the occupancy of inert and corrosion-resistant TiC particles. The Ni-P-0.5 g L⁻¹ TiC showed almost doubled impedance values compared to a simple Ni-P coated sample (Fig. 12). An increase in the concentration of TiC particles from 0.5 g L⁻¹ up to 2.0 g L⁻¹ has successively increased the corrosion resistance and the maximum impedance values for Ni-P-2.0 g L⁻¹ TiC reaches 23 k $\Omega \text{ cm}^2$ showing an improvement of $\sim 92\%$ when compared to Ni-P coatings. An increase in the pore resistance can be due to

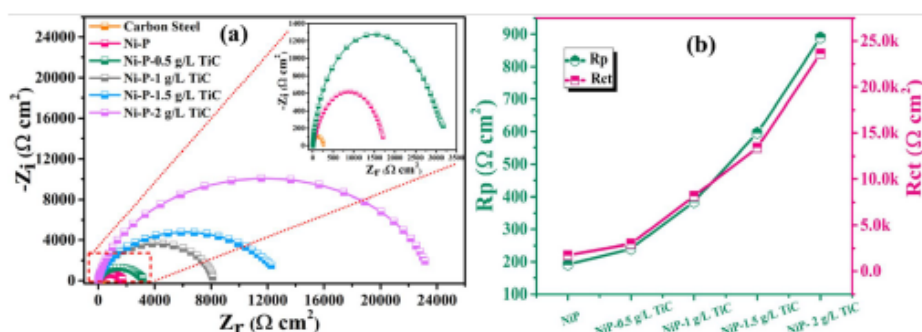


Figure 14. (a) Nyquist plots for carbon steel (substrate) and Ni-P-TiC composite coatings along with fitted resistance values vs. the concentration of TiC particles after the 2 h of immersion in 3.5wt% NaCl solution (b) evolution of R_p and R_{ct} with the TiC particles concentration.

the presence of TiC particles in the pores of Ni-P matrix that decreases the number of conductive paths and increases the surface roughness as observed in AFM results⁴⁹. Improvement in the polarization resistance can be related to the successive increase in the reinforcement of TiC particles in the Ni-P matrix which hinders the electrolyte from reaching the substrate, decreasing the number of active sites and hence providing additional protection against corrosion^{33,42,49}.

Figure 14a depicts the Nyquist plots for carbon steel (substrate), Ni-P and Ni-P-TiC composite coatings containing various concentrations of TiC particles. Nyquist plots of Ni-P coatings and Ni-P-TiC composite coatings demonstrate distinct capacitive loops. The experimental plots for the coated samples were fitted using the two-time constant equivalent electric circuit described in Fig. 13b and the fitting goodness is represented in Fig. 14 in the Nyquist plots. The capacitive loop diameter evidences a successive increase, confirming the higher corrosion resistance in the presence of TiC particles. Figure 14 depicts the evolution of the pore resistance and polarization resistance over time. The incorporation of TiC particles in the Ni-P matrix increases the pore resistance in the coating and acts as a barrier by that delays electrolyte uptake. The decrease of the active surface area is responsible for the increase in the polarization resistance (R_{ct}) as shown in Fig. 14b. Moreover, increasing the concentration of TiC particles in the chemical bath leads to a decrease in the active region and, therefore, increases the corrosion resistance of the composite coatings. The enhancement in the corrosion resistance of the NiP coating in the presence of various concentrations of TiC can be enumerated by the combined effect of (i) Inert TiC particles reduce the active area in the NiP alloy (ii) TiC particles are assumed to block the pores by filling them and restricting the diffusion of the Cl^- ions towards the metal surface and (iii) double-layer capacitance reduces. These findings are consistent with the previous studies^{33,42,49}.

Potentiodynamic polarization analysis. The corrosion resistance of the carbon steel, Ni-P, and Ni-P-TiC composite coatings containing various concentrations of TiC particles was also studied by d.c. potentiodynamic polarization employing a scan rate of 0.167 mV s^{-1} as shown in Fig. 15. Electrochemical parameters such as corrosion potential (E_{corr}), corrosion current density (i_{corr}), anodic Tafel slope (β_a), and cathodic Tafel slope (β_c) were extrapolated from the fitted curve and tabulated in Table 4. Moreover, the corrosion protection efficiency (PE %) was calculated from the formula as reported³³.

$PE\% = 1 - \frac{i_1}{i_2}$ where i_1 is the current density of the carbon steel and i_2 is the current density of coated samples. The maximum value of current density ($55.94 \mu\text{A cm}^{-2}$) is observed for carbon steel at a corrosion potential of -533 mV , the most cathodic one observed in Fig. 15. The current density decreases to $38.43 \mu\text{A cm}^{-2}$ for the Ni-P coatings and further decreases with increasing concentrations of TiC particles in the Ni-P matrix. Thus, the values of current density decrease to $25.62 \mu\text{A cm}^{-2}$, $7.79 \mu\text{A cm}^{-2}$, $6.49 \mu\text{A cm}^{-2}$ and $4.91 \mu\text{A cm}^{-2}$ for the 0.5 g L^{-1} , 1.0 g L^{-1} , 1.5 g L^{-1} , and 2.0 g L^{-1} TiC composite coatings respectively. Moreover, the corrosion potential, becomes slightly more anodic for the Ni-P coatings and increases from $\sim -372 \text{ mV}$ to $\sim -312 \text{ mV}$ with increasing concentrations of TiC suggesting a slight inhibition of the anodic activity in the presence of the TiC particles in the Ni-P matrix. Interestingly, for the TiC concentrations of 1.0 , 1.5 and 2.0 g L^{-1} , the anodic current density is independent of the content of TiC particles, and significantly lower compared to the Ni-P coating. This trend evidences that the anodic activity is reduced in the presence of the TiC particles (for the 3 highest concentrations). However, the cathodic current density tends to increase as the concentration of particles increases, approaching the values observed for the Ni-P coating and steel. This indicates that the cathodic processes, mainly oxygen reduction, are favored by the presence of TiC particles. The potentiodynamic polarization results show that Ni-P coatings had lower corrosion resistance compared to steel, displaying a corrosion protection efficiency of $\sim 31\%$. In such composite coatings, corrosion often initiates at grain boundaries of the nodules as result of the adsorption of chloride ions. The anodic activity leads to the formation of soluble $NiCl_2$, which can proceed to formation of pits⁷². The corrosion protection efficiency, consequence of the decreased corrosion current density, increases with the increasing concentration of TiC particles in the Ni-P matrix. The highest corrosion protection efficiency

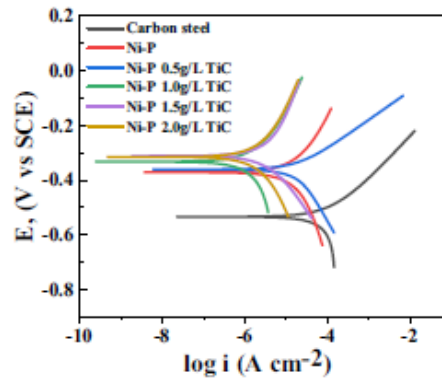


Figure 15. Potentiodynamic profiles of carbon steel, Ni-P and Ni-P-TiC composite coating with increasing concentration of TiC.

Composition	β_a (V/decade)	β_c (V/decade)	i_{corr} ($\mu\text{A cm}^{-2}$)	E_{corr} (mV)	PEN
Carbon steel	0.09617	0.2275	55.94	-534.0	
Ni-P	0.3514	0.6088	38.43	-372.0	31.3%
Ni-P 0.5 g L ⁻¹ TiC	0.1059	0.2664	25.62	-361.0	54.2%
Ni-P 1.0 g L ⁻¹ TiC	0.4342	0.2902	7.79	-333.0	86.0%
Ni-P 1.5 g L ⁻¹ TiC	0.4354	0.2434	6.49	-312.0	88.4%
Ni-P 2.0 g L ⁻¹ TiC	0.384	0.4246	4.91	-315.0	91.2%

Table 4. Electrochemical parameters derived from the potentiodynamic polarization curve of carbon steel, Ni-P, and Ni-P-TiC composite coating containing various concentration of TiC particles.

(~ 90%) was achieved at a TiC concentration of 2.0 g L⁻¹. To conclude, the inclusion of TiC particles in the Ni-P alloy matrix has improved the corrosion resistance as the concentration of TiC particles. By the one hand, the presence of particles inhibits the anodic reactions and, on the other hand, it contributes to reduce the number of active sites for the adsorption of chloride ions on the surface defects such as cracks and pores. Enhancement in the corrosion resistance by increased concentration of reinforcement is in good agreement with literature^{33,35,36}.

Conclusions

Ni-P-TiC composite coatings containing various concentrations of TiC particles were synthesized using the electrodeposition technique. The amount of TiC particles in the Ni-P matrix has a significant influence on its morphological, structural, mechanical, and corrosion protection properties. The hardness of Ni-P-TiC composite coatings increases with an increasing amount of TiC particles in the Ni-P matrix. However, an excessive amount of TiC particles (2.0 g L⁻¹) leads to particles agglomeration and thus reduction in hardness. Electrochemical studies confirm the increased the corrosion protection offered by the Ni-P coatings with an increasing amount of TiC particles. The Ni-P-TiC composite coatings demonstrate superior mechanical and corrosion protection properties when compared to Ni-P coatings suggesting their utilization in many industries such as automobile, marine, electronic, oil, and gas industries.

Received: 12 November 2020; Accepted: 20 January 2021

Published online: 05 March 2021

References

- Zamani, S. M., Hassanzadeh-Taheriz, S. A. & Shartfi, H. Failure analysis of drill pipe: a review. *Eng. Fail. Anal.* **59**, 605–623 (2016).
- Xie, M. & Tian, Z. A review on pipeline integrity management utilizing in-line inspection data. *Eng. Fail. Anal.* **92**, 222–239 (2018).
- Ossai, C. I., Boswell, B. & Davies, I. I. Pipeline failures in corrosive environments—a conceptual analysis of trends and effects. *Eng. Fail. Anal.* **53**, 36–58 (2015).
- Xu, X. *et al.* Corrosion of stainless steel valves in a reverse osmosis system: analysis of corrosion products and metal loss. *Eng. Fail. Anal.* **105**, 40–51 (2019).
- Amaya-Gómez, R. *et al.* Reliability assessments of corroded pipelines based on internal pressure—a review. *Eng. Fail. Anal.* **98**, 190–214 (2019).

6. Bhandari, J. et al. Modelling of pitting corrosion in marine and offshore steel structures—a technical review. *J. Loss Prev. Process Ind.* **37**, 39–62 (2015).
7. Pinigar, M. & Jackson, J. Application of corrosion inhibitors for steels in acidic media for the oil and gas industry: a review. *Corros. Sci.* **86**, 17–41 (2014).
8. Shekari, E., Khan, F. & Ahmed, S. Economic risk analysis of pitting corrosion in process facilities. *Int. J. Press. Vessels Pip.* **157**, 51–62 (2017).
9. Shakoore, R. A. et al. Properties of electrodeposited Ni–B–Al₂O₃ composite coatings. *Mater. Des.* **64**, 127–135 (2014).
10. Shakoore, R. et al. Synthesis, characterization and applications of electroless Ni–B coatings—a review. *Int. J. Electrochem. Sci.* **11**, 2486–2512 (2016).
11. Pfeifer, M. Chapter 5 - manufacturing process considerations. In *Materials Enabled Design* (ed. Pfeifer, M.) 115–160 (Butterworth-Heinemann, 2009).
12. Gurrappa, I. & Binder, L. Electrodeposition of nanostructured coatings and their characterization—a review. *Sci. Technol. Adv. Mater.* **9**(4), 043001 (2008).
13. Lelevic, A. & Walsh, F. C. Electrodeposition of Ni–P composite coatings: a review. *Surf. Coat. Technol.* **378**, 124803 (2019).
14. Giurlant, W. et al. Electroplating for decorative applications: recent trends in research and development. *Coatings* **8**, 260 (2018).
15. Nava, D. et al. Effects of heat treatment on the tribological and corrosion properties of electrodeposited Ni–P alloys. *Int. J. Electrochem. Sci.* **8**, 2670–2681 (2013).
16. Lelevic, A. & Walsh, F. C. Electrodeposition of Ni–P composite coatings: a review. *Surf. Coat. Technol.* **378**, 124803 (2019).
17. Fayyad, E. et al. Recent advances in electroless-plated Ni–P and its composites for erosion and corrosion applications: a review. *Emerg. Mater.* **1**, 3–24 (2018).
18. Sadeghi, A. *Microstructure evolution and strengthening mechanism in Ni-based composite coatings* (2016).
19. Ma, C. et al. The electrodeposition and characterisation of low-friction and wear-resistant Co–Ni–P coatings. *Surf. Coat. Technol.* **235**, 495–505 (2013).
20. Bahadormanesh, B. & Ghorbani, M. Electrodeposition of Zn–Ni–P compositionally modulated multilayer coatings: an attempt to deposit Ni–P and Zn–Ni alloys from a single bath. *Electrochim. Commun.* **81**, 93–96 (2017).
21. Sknar, Y. E., Savchuk, O. O. & Sknar, I. V. Characteristics of electrodeposition of Ni and Ni–P alloys from methanesulfonate electrolytes. *Appl. Surf. Sci.* **423**, 340–348 (2017).
22. Shakoore, R. A. et al. Synthesis and properties of electrodeposited Ni–B–CeO₂ composite coatings. *Mater. Des.* **59**, 421–429 (2014).
23. Wang, Y. et al. Microstructure and properties of sol-enhanced Ni–Co–TiO₂ nano-composite coatings on mild steel. *J. Alloy. Compd.* **649**, 222–228 (2015).
24. Shakoore, R. A. et al. Electrodeposition of Ni–B–Zn alloy coatings and their characterization. In *Proceedings of the 4th International Gas Processing Symposium* (eds Al-Marri, M. J. & Eljack, F. T.) 149–157 (Elsevier, 2015).
25. Hansal, W. E. G. et al. Pulse-electrodeposited Ni–P–SiC composite coatings. *Electrochim. Acta* **114**, 851–858 (2013).
26. Zoltik-Karathanasis, A., Milickovic-Kosanovic, T. & Deligkiozi, I. Effect of organic additives in the structure and functional properties of Ni–P composite coatings reinforced by nano-SiC and MWCNT. In *10th Pan-Hellenic Scientific Congress of Chemical Engineering, Patra* (2015).
27. Chuang, Y.-C. et al. Effect of surfactant on the electrodeposition of Ni–P coating in emulsified supercritical CO₂ baths. *Thin Solid Films* **529**, 322–326 (2013).
28. Alleg, S. et al. Microstructure and magnetic properties of Ni–P alloys. *J. Supercond. Nov. Magn.* **29**(4), 1001–1011 (2016).
29. Luo, H. et al. Synthesis of a duplex Ni–P–YSZ/Ni–P nanocomposite coating and investigation of its performance. *Surf. Coat. Technol.* **311**, 70–79 (2017).
30. Dhanapal, K., Narayanan, V. & Stephen, A. Effect of phosphorus on magnetic property of Ni–P alloy synthesized using pulsed electrodeposition. *Mater. Chem. Phys.* **166**, 153–159 (2015).
31. Elias, L., Damle, V. H. & Hegde, A. C. Electrodeposited Ni–P alloy thin films for alkaline water splitting reaction. *IOP Conf. Ser. Mater. Sci. Eng.* **149**, 012179 (2016).
32. Elias, L., Bhat, B. & Hegde, A. Development of nanolaminated multilayer Ni–P alloy coatings for better corrosion protection. *RSC Advances* **6**, 34005–34013 (2016).
33. Bahgat Radwan, A. et al. Properties enhancement of Ni–P electrodeposited coatings by the incorporation of nanoscale Y₂O₃ particles. *Appl. Surf. Sci.* **457**, 956–967 (2018).
34. Tamilarasan, T. R. et al. Wear and scratch behaviour of electroless Ni–P–nano-TiO₂: Effect of surfactants. *Wear* **346–347**, 148–157 (2016).
35. Farzaneh, A. et al. Electrochemical and structural properties of electroless Ni–P–SiC nanocomposite coatings. *Appl. Surf. Sci.* **276**, 697–704 (2013).
36. Sadreddini, S. & Afshar, A. Corrosion resistance enhancement of Ni–P–nano SiO₂ composite coatings on aluminum. *Appl. Surf. Sci.* **303**, 125–130 (2014).
37. Jin, H., Jiang, S. & Zhang, L. Structural characterization and corrosive property of Ni–P/CeO₂ composite coating. *J. Rare Earths* **27**(1), 109–113 (2009).
38. Li, C. et al. Microstructure evolution and mechanical properties of reactive plasma sprayed Ti₃SiC₂–Ti₅Si₃–TiC composite coatings. *Mater. Chem. Phys.* **254**, 123495 (2020).
39. He, X., Song, R. G. & Kong, D. J. Effects of TiC on the microstructure and properties of TiC/TiAl composite coating prepared by laser cladding. *Opt. Laser Technol.* **112**, 339–348 (2019).
40. Wang, C. et al. Indentation and bending behavior of electroless Ni–P–Ti composite coatings on pipeline steel. *Surf. Coat. Technol.* **334**, 243–252 (2018).
41. Balaraju, J. N., Sankara Narayanan, T. S. N. & Seshadri, S. K. Electroless Ni–P composite coatings. *J. Appl. Electrochem.* **33**(9), 807–816 (2003).
42. Radwan, A. B. & Shakoore, R. A. Aluminum nitride (AlN) reinforced electrodeposited Ni–B nanocomposite coatings. *Ceram. Int.* **46**(7), 9863–9871 (2020).
43. Yusuf, M. et al. Synthesis and characterisation of Ni–B/Ni–P–CeO₂ duplex composite coatings. *J. Appl. Electrochem.* **48**, 391–404 (2018).
44. Yang, Y. et al. Fabrication and characterization of electroless Ni–P–ZrO₂ nano-composite coatings. *Appl. Nanosci.* **1**(1), 19–26 (2011).
45. Knyazev, A. V. et al. Magnetic properties of electrodeposited amorphous nickel–phosphorus alloys. *Russ. J. Electrochem.* **53**(3), 270–274 (2017).
46. Afroukhteh, S., Dehghanian, C. & Emamy, M. Preparation of electroless Ni–P composite coatings containing nano-scattered alumina in presence of polymeric surfactant. *Prog. Nat. Sci. Mater. Int.* **22**, 318–325 (2012).
47. Li, B. & Zhang, W. Microstructural, surface and electrochemical properties of pulse electrodeposited Ni–W/Si₃N₄ nanocomposite coating. *Ceram. Int.* **44**(16), 19907–19918 (2018).
48. Safavi, M. S. & Rasooli, A. Ni–P–TiO₂ nanocomposite coatings with uniformly dispersed Ni₃Ti intermetallics: effects of current density and post heat treatment. *Surf. Coat. Technol.* **372**, 252–259 (2019).
49. Sliem, M. H. et al. Enhanced mechanical and corrosion protection properties of pulse electrodeposited Ni–P–ZrO₂ nanocomposite coatings. *Surf. Coat. Technol.* **403**, 126340 (2020).

50. Restrepo Parra, E., Arango, P. J. & Benavides, V. XPS structure analysis of TiN/TiC bilayers produced by pulsed vacuum arc discharge. *Dyna* 77, 64–74 (2010).
51. Spanou, S. et al. Self cleaning behaviour of Ni/nano-TiO₂ metal matrix composites. *Electrochim. Acta* 105, 324–332 (2013).
52. Pillai, A. M., Rajendra, A. & Sharma, A. K. Electrodeposited nickel-phosphorous (Ni-P) alloy coating: an in-depth study of its preparation, properties, and structural transitions. *J. Coat. Technol. Res.* 9(6), 785–797 (2012).
53. Ping, Z. et al. Mechanically assisted electroplating of Ni-P coatings on carbon steel. *Surf. Coat. Technol.* 202(24), 6023–6028 (2008).
54. Guglielmi, N. Kinetics of the deposition of inert particles from electrolytic baths. *J. Electrochem. Soc.* 119(8), 1009 (1972).
55. Berçot, P., Peña-Muñoz, E. & Pagetti, J. Electrolytic composite Ni-P/PTFE coatings: an adaptation of Guglielmi's model for the phenomena of incorporation. *Surf. Coat. Technol.* 157(2), 282–289 (2002).
56. Bahadormanesh, B. & Dolati, A. The kinetics of Ni-Co/SiC composite coatings electrodeposition. *J. Alloy. Compd.* 504(2), 514–518 (2010).
57. Franssøer, J., Celis, J. P. & Roos, J. R. Analysis of the electrolytic codeposition of non-Brownian particles with metals. *J. Electrochem. Soc.* 139(2), 413–425 (1992).
58. Celis, J. P., Roos, J. R. & Buelens, C. A mathematical model for the electrolytic codeposition of particles with a metallic matrix. *J. Electrochem. Soc.* 134(6), 1402–1408 (1987).
59. Pouladi, S., Shariat, M. H. & Bahrololoom, M. E. Electrodeposition and characterization of Ni-Zn-P and Ni-Zn-P/nano-SiC coatings. *Surf. Coat. Technol.* 213, 33–40 (2012).
60. Huang, H.-C. et al. Microstructure evolution and hardening mechanisms of Ni-P electrodeposits. *Surf. Coat. Technol.* 205(7), 2097–2103 (2010).
61. Balaraju, J. N., Narayanan, T. S. N. S. & Seshadri, S. K. Structure and phase transformation behaviour of electroless Ni-P composite coatings. *Mater. Res. Bull.* 41(4), 847–860 (2006).
62. Grove, D. E., Gupta, U. & Castleman, A. W. Effect of carbon concentration on changing the morphology of titanium carbide nanoparticles from cubic to cuboctahedron. *ACS Nano* 4(1), 49–54 (2010).
63. Zhou, Y.-R. et al. Electrodeposition and corrosion resistance of Ni-P-TiN composite coating on AZ91D magnesium alloy. *Trans. Nonferrous Met. Soc. China* 26(11), 2976–2987 (2016).
64. Wang, Y. et al. Duplex Ni-P-ZrO₂/Ni-P electroless coating on stainless steel. *J. Alloy. Compd.* 630, 189–194 (2015).
65. Yusuf, M. M. et al. Synthesis and characterisation of Ni-B/Ni-P-CeO₂ duplex composite coatings. *J. Appl. Electrochem.* 48(4), 391–404 (2018).
66. Meshram, A. P., Punth Kumar, M. K. & Srivastava, C. Enhancement in the corrosion resistance behaviour of amorphous NiP coatings by incorporation of graphene. *Diamond Relat. Mater.* 105, 107795 (2020).
67. Ghavidel, N. et al. Corrosion and wear behavior of an electroless Ni-P/nano-SiC coating on AZ31 Mg alloy obtained through environmentally-friendly conversion coating. *Surf. Coat. Technol.* 382, 125156 (2020).
68. Czajany, M. & Baumli, P. Effect of surfactants on the behavior of the Ni-P bath and on the formation of electroless Ni-P-TiC composite coatings. *Surf. Coat. Technol.* 361, 42–49 (2019).
69. Fayyad, E. M. et al. Novel electroless deposited corrosion-resistant and anti-bacterial NiP-TiNi nanocomposite coatings. *Surf. Coat. Technol.* 369, 323–333 (2019).
70. Luo, H. et al. Development of electroless Ni-P/nano-WC composite coatings and investigation on its properties. *Surf. Coat. Technol.* 277, 99–106 (2015).
71. Luo, H. et al. Characterization of microstructure and properties of electroless duplex Ni-W-P/Ni-P nano-ZrO₂ composite coating. *Mater. Today Phys.* 4, 36–42 (2018).
72. Song, Y., Shan, D. & Han, E. Comparative study on corrosion protection properties of electroless NiP-ZrO₂ and NiP coatings on AZ91D magnesium alloy. *Mater. Corros. Werkstoffe Und Korrosion - MATER CORROS* 58, 506–510 (2007).

Acknowledgments

This publication was made possible by Qatar University Grant-IRCC-2020-006. Statements made herein are solely the responsibility of the authors. Microstructural analyses (FE-SEM/EDS and HR-TEM) were accomplished at the Central Laboratory Unit (CLU), Qatar University, Doha, Qatar. XPS analysis was accomplished at the Gas Processing Center (GPC), Qatar University, Doha, Qatar. Prof. M. F. Montemor thanks Fundação para a Ciência e a Tecnologia (FCT, Portugal) for financial support under the projects UIDB/00100/2020.

Author contributions

O.F. developed coatings and wrote the initial draft of the manuscript, Adnan Khan helped in experimental work and corrosion studies, R.A.S. designed the experiments and revised the manuscript, A.H. helped in the analysis of mechanical properties of the coatings, M.M.Y. conducted the mechanical testing, M.F.M. revised and corrected the corrosion part and entire manuscript, S.R. modified and revised the whole manuscript, K.K. helped in the analyzing the microstructures of the coatings and revised that part of the manuscript, M.R.I.F. helped in XPS analysis and P.C.O. revised and modified the whole manuscript.

Competing interests

The authors declare no competing interests.

Additional information

Correspondence and requests for materials should be addressed to R.A.S.

Reprints and permissions information is available at www.nature.com/reprints.

Publisher's note Springer Nature remains neutral with regard to jurisdictional claims in published maps and institutional affiliations.

Surface & Coatings Technology
Evaluation of Mechanical and Corrosion Resistance Characteristics of Ni-P-ZrC
nanocomposite coatings
 --Manuscript Draft--

Manuscript Number:	
Article Type:	Full Length Article
Keywords:	Nanocomposite coatings; electrodeposition; reinforcement; hardness; corrosion
Corresponding Author:	Abdul Shakoor, PhD Qatar university Doha, QATAR
First Author:	Osama Fayyaz
Order of Authors:	Osama Fayyaz A. Bahgat Radwan Mostafa H. Sliem R. A. Shakoor Aboubakr M. Abdullah MD Anwarul Hasan
Abstract:	<p>The current study reports the structural, mechanical, wear, erosion, and corrosion-resistant properties of the as-electrodeposited Ni-P-ZrC nanocomposite coatings. For a clear comparison, Ni-P and Ni-P-ZrC nanocomposite coatings containing 0.75 g/L zirconium carbide nanoparticle (ZCNPs) were developed through the electrodeposition technique. The synthesized coatings were thoroughly investigated employing various techniques namely field emission scanning electron microscopy (SEM), energy dispersive x-ray spectroscopy (EDS), X-ray diffraction (XRD), atomic force microscopy (AFM), microhardness, nanoindentation, and electrochemical impedance spectroscopy (EIS), etc. Successful co-electrodeposition of ZCNPs in the as-prepared Ni-P alloy is attained without any observable defects. It is observed that the addition of ZCNPs has a considerable impact on structural, mechanical, and corrosion resistance. Enhancement in the mechanical properties is observed due to reinforcement of Ni-P matrix by the ZCNPs, which can be accredited to mainly dispersion hardening influence. The wear resistance and erosion of the as-prepared metallic coatings were evaluated, indicating an improvement upon the addition of ZCNPs. Furthermore, the corrosion protection efficiency (PE %) of the Ni-P matrix was enhanced by the incorporation of ZCNPs from 71 to 85.4%. The Ni-P-ZrC nanocomposite coatings provide an exciting option for their utilization in the automotive, electronics, aerospace, oil, and gas industry.</p>
Suggested Reviewers:	Zohair Farhat Zoheir.Farhat@dal.ca Wei Gao w.gao@auckland.ac.nz Raymundo Case raymundo.case@tamu.edu